Master Thesis

CFD SIMULATION OF THE CRESTWING WAVE ENERGY CONVERTER

carried out for the purpose of obtaining the degree of Master of Science (MSc or Dipl.-Ing. or DI), submitted at TU Wien, Faculty of Mechanical and Industrial Engineering, by

DANIELA DORIS LEIBETSEDER, BSc

Mat.Nr.: 01612753

under the supervision of

Univ.Prof. Dipl.-Ing. Dr.-Ing. Alfredo Soldati
Prof. Dr. Jens Honoré Walther

Institute of Fluid Mechanics and Heat Transfer, E322

Vienna, October 2022

Author's address:

Institute of Fluid Mechanics and Heat Transfer
Vienna University of Technology
Tower BA/E322, Getreidemarkt 9
1060 Vienna – Austria

Cover:

Caption of cover picture (if any)

Affidavit

I declare in lieu of oath, that I wrote this thesis and performed the associated research myself, using only literature cited in this volume. If text passages from sources are used literally, they are marked as such.

I confirm that this work is original and has not been submitted elsewhere for any examination, nor is it currently under consideration for a thesis elsewhere.

I acknowledge that the submitted work will be checked electronically-technically using suitable and state-of-the-art means (plagiarism detection software). On the one hand, this ensures that the submitted work was prepared according to the high-quality standards within the applicable rules to ensure good scientific practice "Code of Conduct" at the TU Wien. On the other hand, a comparison with other student theses avoids violations of my personal copyright.

City and Date

Signature

Acknowledgments

I would like to thank Prof. Alfredo Soldati for supervising this thesis. I am grateful for the opportunity to write this thesis within the ERASMUS programme at the Technical University of Denmark in cooperation with Crestwing. During my exchange, Prof. Jens Honoré Walther supervised my work and I would like to thank him particularly. I really appreciate the support, the numerous interesting discussions on the topic and the feedback on my work. Further, I would like to thank Prof. Yanlin Shao, MSc Stig Staghøj Knudsen and MSc Rune Pilgaard Bloom for their input in several discussions and their feedback.

Last but not least, I would like to thank my friends and family for supporting and encouraging me during my studies.

Abstract

Wave energy has great potential to contribute to sustainable energy production as waves have the highest energy intensity of all renewable energy sources. Wave energy still faces some challenges, but current advancements led to the development of the Crestwing wave energy converter. It uses the concept of wave activated body technology and employs a mechanical power-take-off system.

In this thesis, a CFD simulation of the Crestwing wave energy converter is set up aiming to gain a better understanding of the behaviour and the performance of the Crestwing wave energy converter in ocean waves and its influence on the waves while providing validated results. The CFD simulations use the dynamic fluid body interaction model and the overset mesh technique. Since the simulations are based on experiments conducted at the Danish Hydraulic Institute, the design of the wave energy converter and the dimensions of the wave tank correspond to experiments. The simulated wave energy converter is operating in fifth order Stokes waves, is moored with a catenary, and is equipped with a power-take-off system modelled by a spring damper coupling.

A reasonable and sufficiently accurate simulation has been set up, by validating the wave generation in an empty wave tank and a successful verification study of the mesh and time step. In the following, numerous simulations of the wave energy converter operating in different wave conditions are performed and the results are compared to those of experiments. Also, five applications of the power-take-off system are tested which differ in the intensity of the force in the power-take-off system depending on its motion. For all conducted simulations, the energy exerted on the device and the energy in the power-take-off system are determined, which allows to define the efficiency of the first wave energy conversion stage and the overall efficiency based on the theoretical energy of the incident wave. Additionally, the resulting wave field is investigated in greater detail by determining the wave elevation at different locations in the empty wave tank.

Zusammenfassung

Wellenenergie hat großes Potential zu einer nachhaltigen Energieproduktion beizutragen, da Wellen von allen erneuerbaren Energiequellen die größte Energiedichte haben. Die Wellenenergie steht allerdings vor einigen Herausforderungen, jedoch führten aktuelle Fortschritte zur Entwicklung des Crestwing Wellenenergiekonverters. Dieser ist ein wellenaktivierter Körper und nutzt ein mechanisches Energietransformationssystem.

In dieser Arbeit wird eine CFD-Simulation des Crestwing Wellenenergiekonverters erstellt, um ein besseres Verständnis des Verhaltens und der Effizienz des Wellenenergiekonverters in Meereswellen und dessen Einflusses auf die Wellen zu gewinnen. Gleichzeitig sollen validierte Ergebnisse bereitgestellt werden. Die CFD-Simulationen verwenden das dynamische Fluid-Körper-Interaktionsmodell und die Overset-Mesh-Technik. Da die Simulationen auf Experimenten beruhen, die am Dänischen Hydraulischen Institut durchgeführt wurden, entsprechen das Design des Wellenenergiekonverters und die Abmessungen des Wellenbeckens den Experimenten. Der simulierte Wellenenergiekonverter arbeitet in Stokes-Wellen fünfter Ordnung, ist mit einer Kette verankert und mit einem durch eine Feder-Dämpfer-Kombination modellierten Energietransformationssystem ausgestattet.

Durch die Validierung der Wellenerzeugung in einem numerischen Wellenbecken und eine erfolgreiche Verifizierung des Meshs und des Zeitschritts wird eine ausreichend genaue Simulation erstellt. Im Folgenden wird der Wellenenergiekonverter in verschiedenen Wellenbedingungen simuliert und die Ergebnisse anschließend mit experimentellen Daten verglichen. Außerdem werden fünf Varianten des Energietransformationssystem getestet, die sich durch die Intensität der Kraft im Energietransformationssystem abhängig von dessen Bewegung unterscheiden. Für alle durchgeführten Simulationen werden die auf das Gerät ausgeübte Energie und die Energie im Energietransformationssystem bestimmt. Mit Hilfe der theoretischen Wellenenergie der einfallenden Welle kann dann der Wirkungsgrad der ersten Wellenenergieumwandlungsstufe und der Gesamtwirkungsgrad bestimmt werden. Zusätzlich wird das resultierende Wellenfeld durch die Bestimmung der Wellenhöhe an verschiedenen Stellen im numerischen Wellenbecken genauer untersucht.

Contents

List of Figures

List of Tables

List of Symbols

Abbreviation	Definition
CFD	Computational Fluid Dynamics
CFL	Courant-Friedrichs-Lewy
CO_2	carbon dioxide
CPU	central processing unit
DFBI	Dynamic Fluid Body Interaction
DHI	Danish Hydraulic Institute
DoF	6-Degrees of Freedom
EU	European Union
HRIC	High-Resolution Interface Capturing
PTO	power-take-off system
URANS	unsteady Reynolds-Averaged Navier-Stokes
VOF	Volume Of Fluid
3D	three dimensional

Symbol	Unit	Definition
A	m	wave amplitude
A_n	m	wave amplitude of the nth wave of a wave group consisting of N waves of different wave numbers
A_{ij}	–	coefficients for solution of fifth order Stokes theory used by StarCCM+
B_{22}, B_{31}, B_{42}, B_{44}, B_{53}, B_{55}	–	coefficients for solution of fifth order Stokes theory used by StarCCM+
c	m/s	wave speed
$(c-\overline{u})_{fifth}$	m/s	wave celerity excluding the current according to fifth order Stokes theory

c_E	m/s	mean uniform current
c_g	m/s	group velocity
c_m	m/s	perturbation coefficient of the wave celerity
C, D	m^2/s	constants of the solution for the amplitude of the velocity potential $Z(z)$
C_0, C_2, C_4	–	coefficients for solution of fifth order Stokes theory used by StarCCM+
$C_{\epsilon 1}$	–	constant for the k-ϵ model
$C_{\epsilon 2}$	–	constant for the k-ϵ model
C_μ	–	constant for the k-ϵ model
d	m	height
D_f	N	drag force parallel to the free stream
$E_f = z - \eta$	m	definition of the free surface
E_k	J	kinetic energy contained in a propagating wave
$\overline{E_k}$	J/m^2	mean kinetic energy density contained in a propagating wave
$E_{OnDevice}$	J	energy exerted on the device
E_p	J	potential energy contained in a propagating wave
$\overline{E_p}$	J/m^2	mean potential energy density contained in a propagating wave
E_{PTO}	J	energy in the power-take-off system
E_{tot}	J	total energy contained in a propagating wave
$\overline{E_{tot}}$	J/m^2	total mean energy density contained in a propagating wave
E_{Waves}	J	theoretical wave energy
$E_{WavesAfter}$	J	theoretical wave energy 0.1 m after the device
$f_{rad,k}$	N	component k of the radiation force oscillating in mode j
F_{left}	N	force due to the power-take-off system on the smaller (left) pontoon
F_{right}	N	force due to the power-take-off system on the greater (right) pontoon

h	m	water depth
H	m	wave height
H_{After}	m	wave height 0.1 m after the device
k	1/m	wave number
k_d	kg/s	damping coefficient
k_e	kg/s^2	elastic coefficient
k_n	1/m	wave number of the nth wave component of a wave group consisting of N waves of different wave numbers
k_t	m^2/s^2	turbulent kinetic energy
l	m	length
L_{device}	m	length of the wave energy converter
L_f	N	lift force normal to the free stream
m	kg	mass
m_{total}	kg	mass of the wave energy converter
n_b	m	normal coordinate to the body surface
n_h	m	normal coordinate to the seabed
n_k	–	component k of the normal vector
$N(t)$	m^2/s^2	time dependant constant in Bernoulli's equation
p	Pa	pressure
$\overline{p}$	Pa	mean pressure
p'	Pa	fluctuating pressure
p_a	Pa	atmospheric pressure
p_{abs}	Pa	absolute pressure
P	W	wave energy flux
$\overline{P}$	W/m	mean wave energy flux per width of the wave incident on the device
$P_{OnDevice}$	W	wave power exerted on device
P_{PTO}	W	power in the power-take-off system
P_{Waves}	W	theoretical wave power
q		any parameter of a flow
$\bar{q}$		mean part of any parameter of a flow

q'		fluctuating part of any parameter of a flow
r	m	radial distance from the body
s	$-$	wave steepness
S	m^2	surface
S_ϕ	$kg/(s^2m)$	source term at the cell center
t	s	time
t_{elapse}	s	elapse time
t_{CPU}	s	CPU time
T	s	wave period
$\overline{u}$	m/s	universal current
u_j	m/s	unit velocity of the body which oscillates in mode j
u_n	m/s	velocity normal to the body surface
U	m/s	velocity of the control volume
U_n	m/s	velocity normal to the control volume
U_R	$-$	Ursell number
v_h	m/s	velocity normal to the seabed
v_{Spring}	m/s	velocity of the spring damper coupling
V	m^3	volume
V_i	m^3	volume of the component i
w	m	width
x_{mean}	m	mean spring elongation between two time steps
x_n	m	spring elongation at time step n
x_{n+1}	m	spring elongation at time step n+1
x_{Spring}	m	elongation of the spring damper coupling
x_0	m	relaxation length of the spring damper coupling
$y+$	$-$	non-dimensional wall distance
z_0	m	total head measured from the still water level
$Z(z)$	m^2/s	amplitude of the velocity potential
α	$\circ$	incident angle of the fluid flow on the aerofoil of a Wells turbine

α_i	$-$	phase volume fraction
β	$\circ$	angle between the direction of propagation of the incident wave and the positive x-axis
Γ	kg/(ms)	face diffusivity
ΔE	s	difference between the theoretical wave energy before and after the device
Δt	s	time step
Δt_{max}	s	maximum time step
Δt_{mean}	s	mean time step
Δx_{back}	m	base size of the background mesh
$\Delta x_{overset}$	m	base size of the overset mesh
ϵ	m^2/s^3	turbulent dissipation rate
ε	$-$	perturbation parameter
η	m	free surface elevation
η_{first}	m	free surface elevation according to first order Stokes theory
η_{fifth}	m	free surface elevation according to fifth order Stokes theory
η_{sup}	m	free surface elevation of the superposition of plane waves characterized by different wave numbers
η_{WEC}	$-$	overall efficiency of the wave energy converter
$\eta_{WEC,1}$	$-$	efficiency of the first wave energy conversion stage
η_0	m	set up term
η_n	m	Fourier coefficients of the free surface elevation
η_{nm}	m	perturbation coefficient of the free surface elevation
λ	m	wave length
μ	Pas	dynamic viscosity
μ_t	Pas	turbulent viscosity
μ_A	Pas	dynamic viscosity of air

μ_W	Pas	dynamic viscosity of water
ν	m^2/s	kinematic viscosity
ρ	kg/m^3	density
ρ_A	kg/m^3	density of air
ρ_W	kg/m^3	density of water
σ_k	–	constant for the k-ϵ model
σ_ϵ	–	constant for the k-ϵ model
ϕ	m^2/s	velocity potential
ϕ_{first}	m^2/s	velocity potential according to first order Stokes theory
ϕ_{fifth}	m^2/s	velocity potential according to fifth order Stokes theory
ϕ_n	–	dimensionless potential coefficients
$\hat{\phi}$	m^2/s	complex velocity potential
$\hat{\phi}_D$	m^2/s	complex diffracted velocity potential
$\hat{\phi}_I$	m^2/s	complex incident velocity potential
$\hat{\phi}_R$	m^2/s	complex radiated velocity potential
$\hat{\phi}_{R\ j}$	m^2/s	complex radiated velocity potential in mode j
φ_n	–	algebraic transformation factor for ϕ_n
φ_{nm}	–	perturbation coefficient for the velocity potential ϕ
$\varphi_{R\ j}$	m	complex amplitude of the radiated velocity potential
ω	1/s	wave frequency
ω_n	1/s	wave frequency of the nth wave of a wave group consisting of N waves of different wave numbers
$\mathbf{a}$	m^2	surface vector
$\mathbf{f}$	N	force vector
$\mathbf{f_D}$	N	diffraction excitation force
$\mathbf{f_{ex}}$	N	excitation force
$\mathbf{f_f}$	N	force due to frictional losses

$\mathbf{f_{FK}}$	N	Froude-Krylov force
$\mathbf{f_{hd}}$	N	hydrodynamic force
$\mathbf{f_{hs}}$	N	buoyancy force
$\mathbf{f_m}$	N	force due to the mooring system
$\mathbf{f_{PTO}}$	N	force of the power-take-off system
$\mathbf{f_{rad}}$	N	radiation force
$\mathbf{f_v}$	N	force due to viscous effects
$\mathbf{g} = (0, 0, g)$	m/s^2	gravity force
$\overline{\mathbf{g}}$	m/s^2	mean gravity force
$\mathbf{m}$	Nm	moment vector
$\mathbf{m_{hd}}$	Nm	hydrodynamic moment vector
$\mathbf{n}$	–	normal vector
$\mathbf{r}$	m	radial distance vector from the body
$\mathbf{s}$	m	displacement of the body's equilibrium position
$\dot{\mathbf{s}}$	m/s	velocity of the displacement
$\ddot{\mathbf{s}}$	m/s^2	acceleration of the displacement
$\mathbf{v}$	m/s	velocity vector
$\overline{\mathbf{v}}$	m/s	mean velocity vector
$\mathbf{v}'$	m/s	fluctuation of the velocity vector
$\mathbf{x} = (x, y, z)$	m	location vector with its components
ω	1/s	angular velocity vector
$\dot{\omega}$	$1/s^2$	angular acceleration vector
$\mathbf{A} = A_{j,k}$	kg	added mass coefficient matrix
$\mathbf{B_{PTO}}$	kg/s	proportionality matrix describing a damper
$\mathbf{C}$	kg/s	buoyancy stiffness matrix
$\mathbf{C_{PTO}}$	kg/s^2	proportionality matrix describing a spring
$\mathbf{I}$	–	identity matrix
$\mathbf{J} = \begin{pmatrix} J_x & 0 & 0 \\ 0 & J_y & 0 \\ 0 & 0 & J_z \end{pmatrix}$	kgm^2	moment of inertia
$\mathbf{M}$	kg	mass matrix

$\mathbf{R} = R_{j,k}$,	kg/s	damping coefficient matrix
$\mathbf{T}$	Pa	shear stress tensor
$\overline{\mathbf{T}}$	Pa	averaged viscous stress tensor
$\mathbf{T_t}$	Pa	Reynolds stress tensor
$\mathbf{X} = X_{j,k}$	kg/s	radiation reactance matrix
$\mathbf{Z} = Z_{j,k}$	kg/s	radiation impedance

1

Introduction

The world's energy demand is increasing day by day, where fossil fuels are still the main source of energy. [45] Besides the fact that fossil fuels are finite resources and will be depleted soon, they also cause tremendous environmental damage. Pollution and the emission of CO_2 can be attributed to the power generation of fossil fuels which contributed to global warming. [28] In order to meet the increased power consumption, preserve resources and protect the environment, sustainable development is impelled following the Paris agreement. Since two-thirds of the EU's total energy supply was based on fossil fuels in 2020, the EU's aim to be climate neutral by 2050 is reinforced by the zero fossil fuel import mission. Thereby, the EU also aims to limit its dependence on imports of fossil fuels from foreign countries. [61] Hence, a mix of renewable energy sources such as wind, solar, biomass, geothermal, and marine energy should secure the energy supply and replace fossil fuels. [28]

Wave energy holds enormous potential to contribute to the renewable energy mix as the annual global wave power resource is estimated 3 TW exceeding the annual global electricity consumption. However, wave energy is still one of the less mature renewable energy sources as wave energy faces several challenges and research was interrupted repeatedly in the past. [45] The main challenge is the irregularity of ocean waves which requires the development of a device, which is capable of converting the irregular motion of ocean waves into a smooth motion that drives a generator, and withstands high forces and a corrosive environment. [16] Thereby, the cost of installation, mooring, operation and maintenance must be minimized to make wave energy economically comparable. [42] Nevertheless, various concepts of wave energy converters have already been developed. They differ in working principles and operating sites allowing wave energy converter to be categorized in different ways. The most common categorization

is based on the way energy is absorbed, where three main groups are distinguished that are referred to as the overtopping energy device, the oscillating water column, and wave-activated bodies. [45]

Even though all concepts face the major challenges, they pursue the goal of extracting energy from ocean waves and converting it into electricity, which is accomplished within three stages. The wave energy converter absorbs the energy from the waves within the first energy conversion stage. In the second energy conversion stage the absorbed energy is converted into useful mechanical energy and finally into electricity using a power-take-off system. [56] Since the power-take-off system performs the decisive stage of energy conversion, it is the key component of the wave energy converter and significantly determines the efficiency and costs of power conversion. [23] Thus, several types of power-take-off systems such as the turbine transfer, the hydraulic motor, as well as direct drive methods have been introduced. [3]

Crestwing has developed a wave energy converter consisting of two closed box structures which are connected by a hinge. The device floats on the water surface, whereby waves induce a relative motion of the two boxes. This oscillatory motion between the two wave-activated bodies is used to harness wave energy, as it is converted into a rotatory motion using a mechanical power-take-off system. This rotatory motion in turn drives the generator system producing electricity. Crestwing's technology has already been tested in several experiments in the deepwater basin of the Danish Hydraulic Institute as well as during two offshore tests. [13] The technology is proven to be promising, but further research and development is required to optimize the Crestwing wave energy converter. Additional experiments are costly and time demanding, which is why CFD simulations are to be used. CFD simulations can provide trustworthy results when verified and validated, contributing to a better understanding of the behaviour of the wave energy converter. However, there is no CFD simulation of the Crestwing wave energy converter yet.

Thus, this thesis aims to provide a CFD simulation of the Crestwing wave energy converter using the CFD software Simcenter STAR-CCM+ 2021.3 from Siemens. The CFD simulations reproduce the experiments conducted in the Danish Hydraulic Institute. Therefore, the dimensions of the wave tank and the geometry of the wave energy converter are chosen accordingly. Firstly, the wave generation in the empty wave tank is verified by

comparing simulated waves to waves according to linear wave theory. After a successful verification study of the empty wave tank, the wave energy converter is simulated in fifth order Stokes waves within this wave tank. Additionally, a mesh and time step verification study is conducted to ensure the best compromise between accuracy and computational effort. The objective of the simulations is to gain a better understanding of the behaviour and the performance of the wave energy converter in ocean waves, and its influence on the waves, while validating the results with experiments. Therefore, the wave energy absorbed by the device as well as the energy in the power-take-off system is determined. This, combined with the theoretical wave energy according to linear wave theory, allows to identify the efficiency of the first wave energy conversion stage and the overall efficiency of the wave energy converter. Further, the wave field resulting from the operating wave energy converter is studied. Due to the irregularity of ocean waves, the behaviour and the efficiency of the wave energy converter in different wave conditions are of high interest. Thus, several simulations of the Crestwing wave energy converter in different wave conditions have been performed and the results are compared to those of experiments. As the power-take-off system is the essential component of wave energy conversion, its influence on the waves, on the behaviour and on the performance of the wave energy converter is crucial. Thus, five different models of the power-take-off system are further investigated.

2

Wave energy converter

The impact of climate change on the planet is intensifying as global temperatures continue to rise leading to higher sea levels and more intense extreme events. This affects natural and human systems with associated loss and degradation of ecosystems, as well as reduced water and food security. [27] Therefore, the main focus is on reducing global CO_2 emissions to net zero by 2050 and limiting the global temperature rise to 1.5 °C while ensuring stable and affordable energy supplies, providing universal energy access, and enabling robust economic growth. [26]

A major potential for reducing CO_2 emissions resides in energy production, as this with 36.5 % accounts for the largest contributor to energy-related CO_2 emissions in 2020. [60] This is due to the fact that fossil fuels still supply 80 % of the world's energy in 2020. [18] Besides the adverse effects on the environment, fossil fuels will soon be depleted, while the world's energy demand is further increasing. [32] Another point to consider is that the dependence on one single energy source must be minimized. To protect the environment, meet the increasing power demand, and preserve resources, a mix of renewable energy sources such as wind, solar, biomass, geothermal and marine energy must be considered. [28]

2.1 Potential of wave energy converter

Especially ocean wave energy is expected to contribute more to the renewable energy mix in the future as it can be very beneficial in comparison to other renewable energy sources. [56] Firstly, the total wave energy resource exceeds the global consumption of electricity. The global wave power resource, excluding areas with less than 5 kW/m and areas with potential ice cover, is estimated 3 TW. [31] However the global consumption

of electricity is 2.3 TW. [45] Additionally, it is claimed that the seasonal variability of the available wave energy meets the seasonal electricity demand. [56] Secondly, the energy intensity of waves is the highest among renewable energy sources and is about 2 - 3 kW/m^2. For comparison the energy density of wind is 0.4 - 0.6 kW/m^2 and the solar energy density is 0.1 - 0.2 kW/m^2. [42] The reason for this is the origin of waves, whereby solar energy is converted into wave energy. [16] Solar energy leads to odd pressure distributions in the atmosphere which in turn generates wind. Hence, waves are generated when the wind is blowing across the surface of the water and a progressive energy transfer from the wind to water in created boundary layers occurs. [31] The energy is carried by the waves over long distances without any significant energy loss. This allows predicting wave conditions ahead of time. [56] Furthermore, wave energy can be extracted 90 % of the time, whereas wind and solar energy are just available 20-30 % of the time. [42] Lastly, the negative environmental impact is minimized by using offshore devices. [16] The CO_2 emissions of power generation associated with wave energy are low compared to solar energy and comparable with wind energy. [56] All points considered, wave energy has great potential in contributing to the renewable energy mix and thereby replacing fossil fuel-based energy. [24]

2.2 History of wave energy converter

The potential of wave energy was already recognized in the late 18th century as the first patent for a wave energy converter was submitted in 1799. With the emerging oil crisis in 1973, research in the field of wave energy was pushed forward. A decrease in research activities could be recognized in the 1980s and 1990s due to the recovering economy leading to reduced funding. [31] Recently, wave energy research was resumed as using renewable energy sources gains more and more importance due to the threat of global warming and increasing fossil fuel prices. [24] This is accompanied by the development of many different concepts, techniques, designs and operating principles for harnessing wave energy. [3]

2.3 Challenges of wave energy converter

Although the basic theoretical knowledge is already established, wave energy is still one of the less mature renewable energy sources and therefore not yet economically competitive with other renewable energy sources. [42] This is due to several challenges that wave energy is facing. The complexity and the large amount of changing environmental parameters such as wind, pressure, temperature, humidity, salinity, water depth and many more, complicate the description and prediction of the environmental conditions at a certain location. [45]

To advance the technology of wave energy and design and optimize wave energy converters, the environmental condition at the operating site must be well known. Thus, accurate metocean data must be provided and refined as the available metocean data is not sufficient yet. Further, the ocean waves are stochastic with irregularity in amplitude with respect to time which leads to continuously changing water surface elevation and frequency. Therefore, the energy magnitude varies enormously. [31] One of the most significant challenges is the conversion of this random, high-force oscillatory motion into a motion that drives a generator. [16] To compensate for the high fluctuation of the wave motion and generate a smooth electrical output, an array of wave energy devices or special electrical systems are required. [31] Not only the water elevation but also the wave direction in offshore locations is highly variable. Thus, the wave energy converter must be either symmetrical or equipped with an adaptive mooring system such that the device can align with the waves and capture the wave energy. Another major challenge is to design the wave energy converter in a way that it operates with maximum efficiency in the most common wave conditions but also withstands extreme wave loads. Further, the components of the wave energy converter must resist the highly corrosive environment. This results in difficulties for the design of electrical components, structural parts and mooring lines, which in turn accounts for the high cost of wave energy conversion technology. [16] Another point that decelerates further development of wave energy technology is that there is no technology convergence. This makes the collaboration of developers more difficult as they can not share their experiences. Further, there are no well-accepted standards yet. Recently, technical specifications are developed to enable developers to evaluate different wave energy technologies. However,

these technical specifications need some time to be accepted as standards. [56] All points considered, the cost of electricity generated from ocean waves must be reduced to make wave energy economically comparable to other energy sources. To do that costs of installation, mooring, operation and maintenance must be minimized. [42] Further, the efficiency of wave energy conversion must be improved. [56]

2.4 Assembly of wave energy converter

The development of wave energy converters is therefore still evolving. There are already many different concepts, which all generally pursue the goal of extracting energy from waves and converting it into electricity. However, they differ in working principles and operating sites. [56] Nevertheless, all wave energy converters are similar in design and consist of four main sub-systems. [45]

The hydrodynamic system is the main part of the wave energy converter. This system absorbs wave energy and transfers forces and motions to the power-take-off system and the reaction system. There are different types such as wave-activated bodies, oscillating water columns, and overtopping energy devices, which are further described in chapter 2.6. The power-take-off system converts the captured wave energy into electricity. Different principles are developed and further discussed in chapter 4. The reaction system moors the wave energy converter and provides a reaction point for the power-take-off system and support for the hydrodynamic system. The control and instrumentation system consists of the processors for the automation and electromechanical processes and the sensors. This system includes data acquisition, communication, data transmission and the human interface. [45]

2.5 Stages of wave energy conversion

Despite all different concepts, the process of wave energy conversion is generally divided into three stages. Firstly, the wave energy is converted into mechanical, pneumatic or potential energy depending on the hydrodynamic system. Overtopping devices capture potential energy, whereas wave-activated bodies save kinetic energy and the oscillating water column captures pneumatic power in the air chamber. Secondly, the absorbed energy is converted into useful mechanical energy using a power-take-off system. There

are many different types of power-take-off systems due to varying types of absorbed energy. The main power-take-off systems are hydraulic power-take-off systems, the direct drive for wave-activated bodies, air turbines for oscillating water columns and low head water turbines for overtopping devices. Thirdly, the energy obtained in the secondary energy conversion stage is transformed into electricity by connecting the power-take-off system to the generators. [56]

Since the type of the wave energy converter determines the assembly of the power-take-off system which in turn affects the generator, the three stages are strongly interrelated and progressive. Therefore, all energy conversion stages must be optimized to improve the overall efficiency of the wave energy converter. [66]

2.6 Categorization of wave energy converter

Due to various concepts with different working principles and operating sites, wave energy converters can be categorized in different ways. The categorization by the location where the device is installed introduces onshore, near shore and offshore devices. Another classification is based on device deployment. Thereby, devices with horizontal extension parallel to the direction of wave propagation are called Terminators, while those with horizontal extension orthogonal to the direction of wave propagation are Attenuators. Point Absorbers have small extensions compared to the wavelength. Wave energy converters are also categorized by their working principles in eight main types. [45] However, the most common way to classify wave energy converters is based on the way energy is absorbed. Three main groups are distinguished that are referred to as the overtopping energy device, the oscillating water column and wave-activated bodies. [56]

An overtopping energy device harnesses wave energy using the principle shown in figure 2.1. Waves are guided over a ramp into a reservoir, wherein water is temporarily stored. [45] Thereby, wave motion is blocked from the reservoir and there is an increase of the water head in the reservoir. This leads to a conversion of the unstable wave energy into stable potential energy. Due to the difference between the water level in the reservoir and the mean ocean water level, the water leaves the reservoir through the outlet pipe driving the power-take-off system and generating electricity. The power-

take-off system of the overtopping energy device employs an axial flow turbine which is also used for hydroelectric power generation. [66]

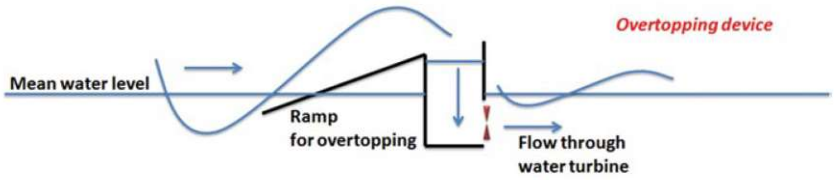

Figure 2.1 – Principle of overtopping wave energy devices [31]

An oscillating water column consists of a partially submerged chamber with an opening below the water surface and an opening connected to the atmosphere as well as air turbines serving as the power-take-off system. The working principle of an oscillating water column is shown in figure 2.2. The wave enters the chamber through the opening below the water surface and changes the water level in the chamber. As the water level is rising, the air in the chamber is compressed, whereas air is sucked into the chamber from outside when the water level declines. [31] This creates pressure fluctuations in the chamber and results in an oscillating airflow. Thus, wave energy is converted into air pressure energy and kinetic energy. The air turbines on top of the chamber are driven by this oscillating airflow and produce electricity. The reciprocating airflow requires the air turbines to be self-rectifying. Therefore, either the Wells turbine, the self-rectifying impulse turbine or the Denniss-Auld turbine is employed. [66]

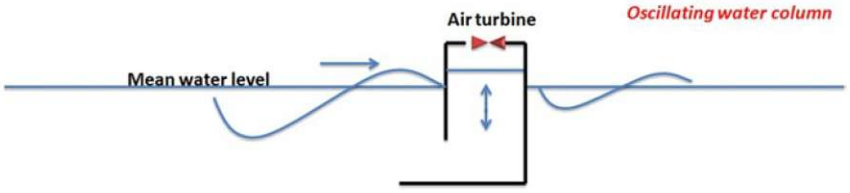

Figure 2.2 – Principle of oscillating water columns [31]

Wave-activated bodies are the main and early concepts among wave energy converters. Wave-activated bodies are fully or partially submerged solid bodies which are floating or sea-bottom mounted. [31] The operating principle can be seen in figure 2.3. The body is induced to move with six degrees of freedom by the irregular characteristics of the waves. [66] Thus, the wave-induced motions of the wave-activated body drive the

power-take-off system and produce electricity. Thereby, the translational motions are used particularly for power generation. [31] To convert the wave-induced motion into electricity, various power-take-off systems such as the hydraulic/pneumatic system, the mechanical gear type, or the direct drive transmission method, are used. [66]

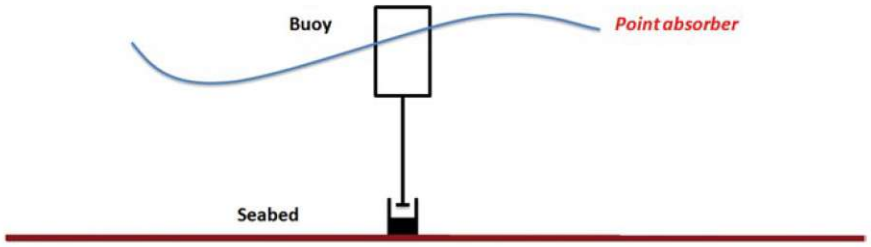

Figure 2.3 – Principle of point absorbers [31]

The Crestwing wave energy converter is one of many concepts of the wave-activated bodies and will be investigated in this thesis. It consists of two closed box structures that are connected by a hinge. The device floats on the water surface and is moored with a specific anchoring system. Crestwing uses the relative motion of the two wave-activated bodies to harness wave energy. Thereby, only one degree of freedom is used for power production. A mechanical power-take-off system converts the oscillatory motion between the two bodies into a rotating motion on an axle using a ratchet mechanism and a flywheel. The rotating axle then drives a gear and a generator system to produce electricity. [45]

3

Wave theory

Understanding the wave effects on the ocean surface and floating structures is of high interest since waves contain large amounts of energy. This energy is converted to electrical power by wave energy converters. [41] This chapter includes the sources and the characteristics of ocean waves. Further, linear wave theory as well as non-linear Stokes theory are introduced. Based on linear wave theory, the wave energy contained by a wave is derived. Finally, the motion response of a body that is immersed in water is analyzed by introducing the forces acting on the floating body.

3.1 Sources of ocean waves

Ocean surface waves are created by different disturbing and restoring forces such as pressure or stress from the atmosphere, for example, wind, earthquakes, the gravity of the earth and celestial bodies, the Coriolis force, and surface tension. The type and scale of these forces influence the wave period, which characterizes the ocean surface waves. [1] Figure 3.1 represents the classification of waves by the wave period.

Capillary waves are mostly generated by the wind and appear as small ripples on the water's surface. They are dominated by the surface tension of the water. Those waves are characterized by a small wave period and a small wavelength. [40]

As the wave is growing due to the impact of the wind, the wave period increases. These waves are considered gravity waves having wave periods between 1 and 30 s. The determining factors of gravity waves are the Earth's gravity and the buoyancy in the water. [40]

Tidal waves are caused by the fluctuation of gravity due to the influence of the moon and the sun. Storms and tsunamis are the results of earthquakes and land movements.

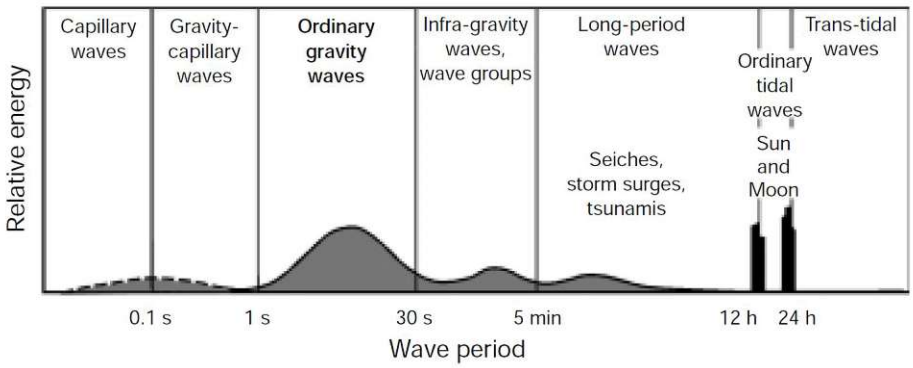

Figure 3.1 – Classification of ocean waves by the wave period [1]

Both are considered long-period waves. [1]

However, waves interacting with wave energy converters are most likely generated by the wind blowing across the surface of the ocean. Hereby, the wind transfers energy into waves through the propagation of pressure fluctuations travelling in the same direction as the waves. At first, waves appear as small ripples on the surface of the water. These small ripples influence the air-flow leading to positive pressure on the windward side and negative pressure on the leeward side of the wave crest. Hence, the net force on the wave and the wave velocity are in phase and a transfer of energy from the wind to the wave occurs. Subsequently, the waves grow and the net force increases with the size of the wave. [45] At some point, the energy transmission does not lead to an increasing size of the waves as the force of the wind is balanced by turbulent losses and white-capping. At this point, the waves are considered to be fully developed. Further, fully developed waves depend on the wind speed and the fetch, describing the distance over which the wind can blow. [5] When the wind stops blowing, the long waves travel faster and leave the short wave behind. Those long waves travel for long distances with little loss of energy and are often referred to as swell waves in the literature. Figure 3.2 represents the generation of wind waves. [45]

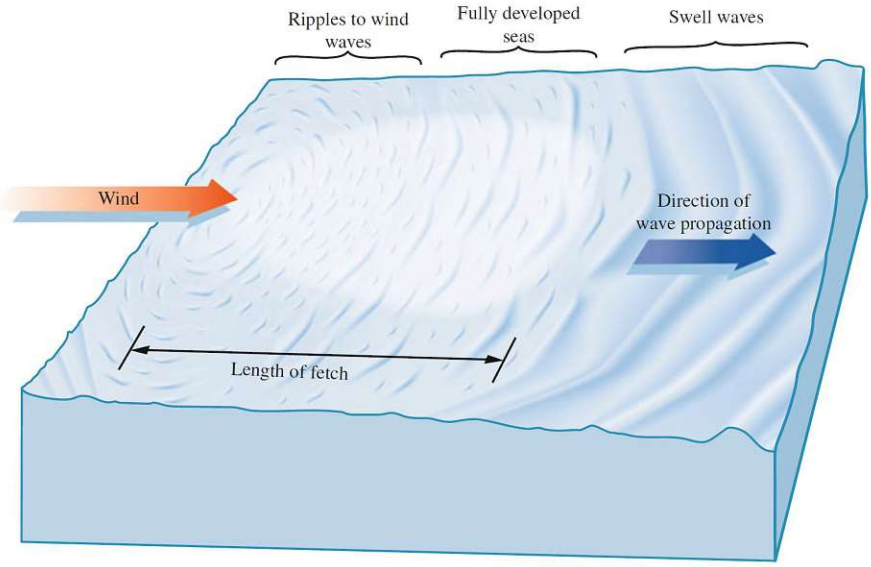

Figure 3.2 – Generation of waves [45]

3.2 Wave characteristics

The characteristics of a single monochromatic wave are considered since wind-generated waves represent a linear superposition of sinusoidal waves of different frequencies, amplitudes, directions, and phases. [58] Thus, sinusoidal waves provide a simplified description of wind-generated waves. [1] A monochromatic wave, as shown in figure 3.3, can be characterized by its height $H = 2A$, wavelength λ and the wave period T. [45] The free surface elevation of a general two-dimensional, sinusoidal wave is [41]

$$\eta(x,t) = A\cos(kx - \omega t) \tag{3.1}$$

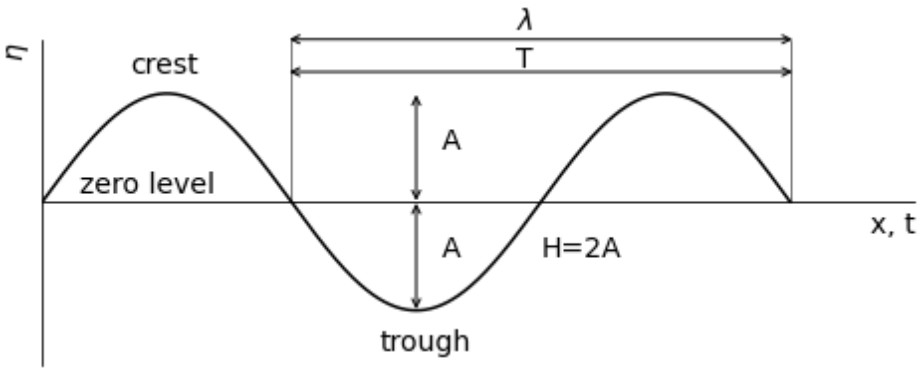

Figure 3.3 – Characteristics of waves [45]

Further, other parameters, such as the wave steepness $s = H/\lambda$, the wave number $k = 2\pi/\lambda$, the wave speed $c = \lambda/T$ and the wave frequency $\omega = 2\pi/T$ are derived from the main characteristics. [45]

Another point to consider is the water depth h and its influence on water particle motion. A water particle on the ocean surface is moving up and down but also backward in the trough and forwards on the crest of the wave. The backward motion is marginally less than the forward motion which results in a small net forward shift of the water particle. The proportions of this displacement depend on the wave steepness.

A water particle in deeper water experiences the same motion as a water particle on the surface, as the water is disturbed due to the propagation of the wave. However, the motion and therefore the displacement of the water particle depend on the water depth and decreases exponentially with increasing water depth. [1]

The water particle motion depending on the water depth is described by the ratio between the water depth h and the wavelength λ, which determines three regions in the ocean. If this ratio is greater than 1/2, the considered region can be classified as deep water. In this region, the net forward shift of the water particle on the surface can be neglected resulting in a circular water particle motion with a velocity of $\pi H/T$.[9] Therefore, ocean waves can be described as simple sinusoidal waves as a good approximation for many engineering applications. Furthermore, the displacement of the water particle at the bottom of the ocean is negligible due to the water depth. Thus, the sea bed can safely be assumed to not influence the water particle motion. Shallow water requires the ratio to be less than 1/20. In this region, the displacement of the water particle at the bottom of the ocean is not negligible due to the proximity to the seabed. Thus, the water particle motion becomes more elliptical with decreasing water depth. Transitional depth describes the region between the deep water and the shallow water. [45]

3.3 Wave modelling

There are various approaches to describing waves mathematically. One of the main parameters distinguishing between linear and non-linear waves is the wave steepness $s = H/\lambda$. It also depends on the regions introduced in chapter 3.2. [34] For deep

water waves with small wave steepness, linear wave theory is often applied as a good approximation. [45] It predicts a circular water particle motion, small amplitudes, and an equal height of the crest and the trough. As the wave steepness increases, non-linear wave models should be applied to assure the accuracy of the solution. In shallow water, the Cnoidal wave theory or other shallow water wave models are applied, whereas the Stokes wave theory is used in transitional or deep water. [65] As the Crestwing Wave Energy Converter is installed in deep water, this work will focus on linear wave theory and Stokes wave theory.

Figure 3.4 shows the range of validity of different wave theories based on the wave steepness $s = H/(gT^2)$ and the relative water depth $h/(gT^2)$. [45] According to [34], it was established for two-dimensional periodic waves, but it is generally used for any kind of water waves.

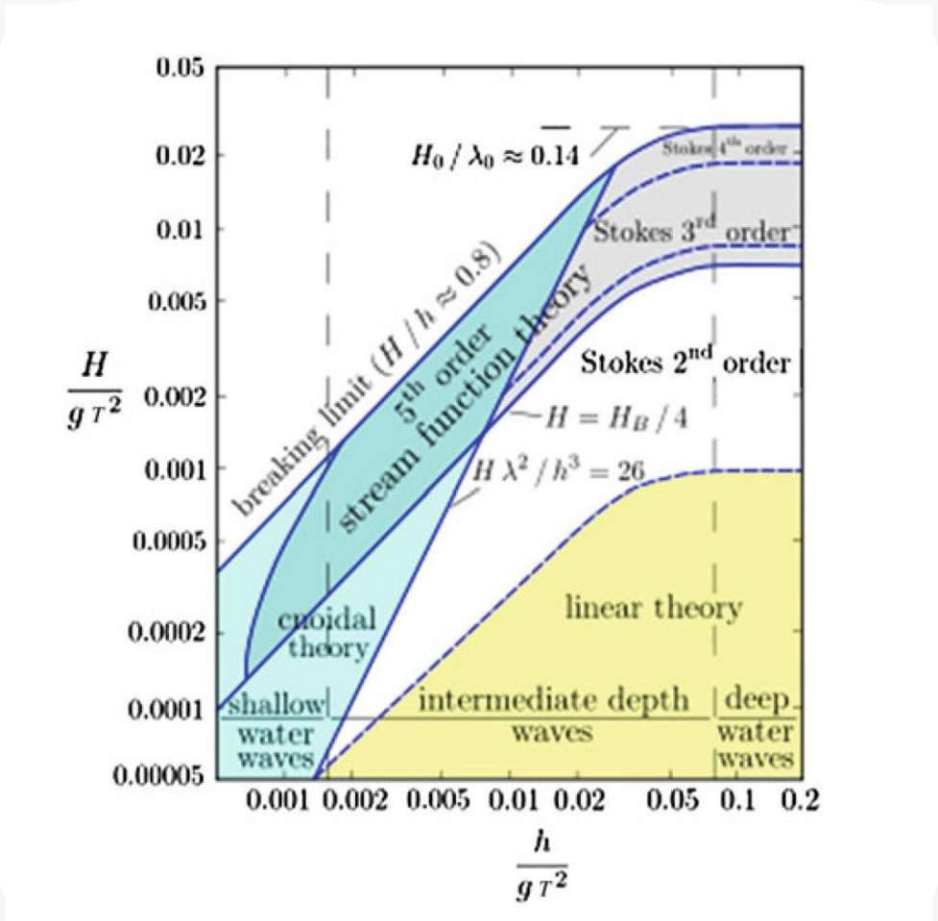

Figure 3.4 – Suitability of different wave theories based on the wave steepness [45]

3.4 Fundamental equations

The basic equations of a flow are derived from fundamental conservation laws of mass, momentum, and energy for a continuum. These are derived from an infinitesimal control volume in differential form. [44]

The continuity equation 3.2 describes the conservation of mass in an infinitesimal control volume and requires that the temporal change in mass is equal to the difference in the incoming and outgoing mass flows. [44]

$$\frac{\partial \rho}{\partial t} + \nabla \cdot (\rho \mathbf{v}) = 0 \tag{3.2}$$

Hereby, ρ is the density and $\mathbf{v}$ is the velocity vector.

Under the assumption of an incompressible, instationary, three-dimensional flow, the continuity equation simplifies to equation 3.3. [43]

$$\nabla \cdot \mathbf{v} = 0 \tag{3.3}$$

According to the conservation law of momentum, the temporal variation of the momentum in an infinitesimal control volume corresponds to the entering and exiting momentum fluxes. Further, normal and shear stresses acting on the control volume as well as volume forces contribute to the temporal change of the momentum. [43] This is described by the momentum equations. [53]

$$\frac{\partial}{\partial t}(\rho \mathbf{v}) + (\mathbf{v} \cdot \nabla)(\rho \mathbf{v}) = \nabla \cdot \mathbf{T} - \nabla p + \rho \mathbf{g} \tag{3.4}$$

Hereby, p is the pressure, $\mathbf{g}$ is the gravity force, and $\mathbf{T}$ is the shear stress tensor. The shear stress tensor is modelled by a constitutive law relating the viscous stresses to the velocity gradients. [44] Assuming further a Newtonian fluid, this constitutive relation is modelled by Stokes's law 3.5. [51]

$$\mathbf{T} = \mu(\nabla \mathbf{v} + (\nabla \mathbf{v})^T) - \frac{2}{3}\mu(\nabla \cdot \mathbf{v})\mathbf{I} \tag{3.5}$$

μ is the dynamic viscosity. Thereby, the conservation law of momentum simplifies to equation 3.6. [43]

$$\left(\frac{\partial \mathbf{v}}{\partial t} + (\mathbf{v} \cdot \nabla)\mathbf{v}\right) = \mathbf{g} - \frac{1}{\rho}\nabla p + \nu \nabla \cdot (\nabla \mathbf{v}) \tag{3.6}$$

3.5 Linear wave theory

Linear wave theory, first developed by Airy in 1845, yields useful, realistic results for many applications. This theory is easier to apply and the received results are easier to comprehend in comparison with higher-order theories. This is why linear wave theory is commonly used in practice. [58] Further, linear wave theory is the fundamental basis of higher order Stokes theory. [29] Nevertheless, the usability of linear wave theory is limited due to simplifying assumptions that are made and lead to less accuracy. [58]
First, a Cartesian coordinate system is introduced. The origin of the Cartesian coordinate system is located on the undisturbed position of the water, called the zero level in figure 3.3. [37] The x-axis points in the direction of the wave propagation and the z-axis points upwards out of the water surface. The elevation on the free surface is defined by the function $z = \eta(x, y, t)$.
To yield the linear wave theory, the following simplifying assumptions have to be made and applied to the governing equations in 3.4. The fluid is considered incompressible, $\rho = const.$ and inviscid, $\nu = 0$. [12] The flow is irrotational, $\nabla \times \mathbf{v} = 0$, which means that fluid particles do not rotate about their center. [37] Further, the wave amplitude is small compared to the wavelength and the water depth, $H/\lambda << 1$ and $H/h << 1$. [29]
Due to the irrotationality of the flow, the velocity can be written as

$$\mathbf{v} = \nabla \phi \tag{3.7}$$

with the velocity potential ϕ being harmonic.
Thus, the waves can be described by a potential flow and the Laplace equation is derived from the continuity equation for an incompressible fluid 3.3. [43]

$$\nabla^2 \phi = 0 \tag{3.8}$$

The Navier-Stokes equation for an incompressible fluid 3.6 simplifies to the Euler

equation if an inviscid flow is assumed and gravity ρg is the only external force . [41]

$$\frac{\partial \mathbf{v}}{\partial t} + (\mathbf{v} \cdot \nabla)\mathbf{v} = \mathbf{g} - \frac{1}{\rho}\nabla p \tag{3.9}$$

The Bernoulli equation is obtained by substituting the condition of an irrotational flow 3.7 in the Euler equation 3.9 followed by some vector operations. [41]

$$\frac{\partial \phi}{\partial t} + \frac{1}{2}(\nabla\phi \cdot \nabla\phi) = -\frac{p}{\rho} - gy + N(t) \tag{3.10}$$

The time dependant constant $N(t)$ does not affect the velocity vector, which is why it can either be neglected or chosen arbitrarily. [41]

Further, boundary conditions at the seabed and on the water's surface have to be applied. First, the sea bed is considered a solid, immovable surface. [63] Thus, there is no flow normal to the seabed. Therefore, the bottom boundary condition is:

$$v_h = \frac{\partial \phi}{\partial n_h} = 0 \qquad at \;\; z = -h \tag{3.11}$$

n_h is the normal coordinate at the seabed. [37] If the seabed can be assumed horizontal, the bottom boundary condition can be written as: [58]

$$\frac{\partial \phi}{\partial z} = 0 \qquad at \;\; z = -h \tag{3.12}$$

Second, the kinematic boundary condition on the water's surface must be satisfied. It implies that water particles on the ocean surface must remain there. Thus, the particle velocity at the free surface $z = \eta$ must be equal to the normal velocity of the free surface. [37] The kinematic boundary condition requires the substantial derivative to be zero at the free surface $E_f = z - \eta$. [12]

$$\frac{DE_f}{Dt} = \frac{D(z-\eta)}{Dt} = \frac{\partial \phi}{\partial z} - \frac{\partial \eta}{\partial t} - \frac{\partial \phi}{\partial x}\frac{\partial \eta}{\partial x} - \frac{\partial \phi}{\partial y}\frac{\partial \eta}{\partial y} = 0 \qquad at \;\; z = \eta \tag{3.13}$$

Assuming that the wave elevation η is sufficiently small compared to the wavelength λ and the water depth h and applying the kinematic boundary condition to the still water level leads to the linearized kinematic boundary condition. [58]

$$\frac{\partial \phi}{\partial z} = \frac{\partial \eta}{\partial t} \qquad at \;\; z = \eta \tag{3.14}$$

Third, the fluid pressure on the water surface is considered to be constant and equal to the atmospheric pressure. The dynamic boundary condition is obtained by applying this assumption to the Bernoulli equation 3.10. [63]

$$-\frac{1}{\rho}(p - p_a) = \frac{\partial \phi}{\partial t} + \frac{1}{2}\nabla\phi \cdot \nabla\phi + g\eta = 0 \qquad at \;\; z = \eta \tag{3.15}$$

Neglecting the higher order terms in equation 3.15 leads to the linearized dynamic boundary condition on the free surface. [41]

$$\eta = -\frac{1}{g}\frac{\partial \phi}{\partial t} \qquad at \;\; z = \eta \tag{3.16}$$

Thus, a set of equations consisting of the Laplace equation 3.8 and the linearized boundary conditions 3.12, 3.14 and 3.16 is obtained. [65] To satisfy this set of equations, the velocity potential must be in the form of equation 3.17. [22]

$$\phi(x, z, t) = \Re[Z(z)e^{-ikx+i\omega t}] \tag{3.17}$$

A general solution for $Z(z)$ is yield solving the Laplace equation 3.8 with the given velocity potential 3.17. [41]

$$Z(z) = Ce^{kz} + De^{-kz} \tag{3.18}$$

Assuming water of infinite depth, $h \to \infty$, the constant D in equation 3.18 vanishes by using the bottom boundary condition 3.11. [63] The velocity potential function simplifies to [41].

$$\phi(x, z, t) = \Re[Ce^{kz-ikx+i\omega t}] \tag{3.19}$$

The constant C in equation 3.19 is obtained using the linearized dynamic boundary condition on the free surface 3.16 and is defined as $C = \frac{igA}{\omega}$. Therefore, the velocity potential in deep water is [41]

$$\phi(x, z, t) = \frac{gA}{\omega}e^{kz}\sin(kx - \omega t) \tag{3.20}$$

Further, the kinematic boundary condition on the free surface 3.14 must be considered. By combining the kinematic 3.14 and the dynamic 3.16 boundary condition on the free

surface an additional condition is obtained. [65]

$$\frac{\partial^2 \phi}{\partial t^2} + g\frac{\partial \phi}{\partial z} = 0 \qquad at \;\; z = 0 \tag{3.21}$$

The dispersion relation for deep water is yielded by substituting the obtained velocity potential 3.20 in this additional condition 3.21. Hereby the wave number k and the wave frequency ω are related. [41]

$$k = \frac{\omega^2}{g} \tag{3.22}$$

The wave speed c in deep water is determined applying the dispersion relation 3.22 to the definition of wave speed $c = \frac{\lambda}{T} = \frac{\omega}{k}$. [41]

$$c = \frac{\lambda}{T} = \frac{\omega}{k} = \sqrt{\frac{g}{k}} = \sqrt{\frac{g\lambda}{2\pi}} \tag{3.23}$$

The general solution $Z(z)$ 3.18 must be adapted if water of finite depth is considered. This leads to the following velocity potential for transitional water

$$\phi(x, z, t) = \frac{gA}{\omega}\frac{\cosh(kz + kh)}{\cosh(kh)}\sin(kx - \omega t) \tag{3.24}$$

and the dispersion relation for transitional water. [41]

$$k\tanh(kh) = \frac{\omega^2}{g} \tag{3.25}$$

The wave speed in transitional water results in 3.26. [41]

$$c = \frac{\omega}{k} = \sqrt{\frac{g}{k}\tanh(kh)} \tag{3.26}$$

Additionally, the velocity potential and the dispersion relation for shallow water, $h \to 0$, can be derived from the general solution for transitional water 3.24 and 3.25, using the asymptotic limits of the hyperbolic functions. [65] The velocity potential for shallow water is

$$\phi(x, z, t) = \frac{gA}{\omega}\cosh(kz)\sin(kx - \omega t) \tag{3.27}$$

and the dispersion relation for shallow water is

$$k^2 = \frac{\omega^2}{gh} \tag{3.28}$$

The wave speed c in shallow water can be approximated from equation 3.26 using the Taylor series for the hyperbolic function which yields 3.29. [41]

$$c = \frac{\omega}{k} = \sqrt{gh} \tag{3.29}$$

The correlations above describe a plane progressive wave. The linear wave theory allows describing ocean surface waves as a superposition of plane waves characterized by different wave numbers. [41]

$$\eta_{sup} = \sum_{n=1}^{N} \Re[A_n e^{ik_n x + i\omega_n t}] \tag{3.30}$$

Due to the different characteristics of each wave in the sum 3.30, the distribution of the waves is hard to predict. Assuming the waves to have almost equal wavelengths and travel in the same direction, the waves travel in groups. This phenomenon is characterized by the group velocity which is defined by equation 3.31. [41]

$$c_g = \frac{d\omega}{dk} \tag{3.31}$$

Applying the dispersion relation 3.22 to equation 3.31 yields the group velocity in deep water, which is equal to half of the wave speed c.

$$c_g = \frac{1}{2}\sqrt{\frac{g}{k}} = \frac{1}{2}c \tag{3.32}$$

In case of transitional water, the dispersion relation 3.25 must be applied to equation 3.31 in order to obtain the group velocity in transitional water 3.33. [41]

$$c_g = \left(\frac{1}{2} + \frac{kh}{\sinh 2kh}\right) c \tag{3.33}$$

In shallow water, the group velocity and the wave speed are equal $c_g = c$, as the expression in brackets in equation 3.33 adds up to one. [41]

3.6 Stokes wave theory

Linear wave theory is only applicable for small wave steepness ($s < 0.01$) and infinitesimally small amplitudes ($A \to 0$). Thereby, the governing equations and the boundary conditions are linearised. [45] If the wave steepness increases, the linearisation is not accurate enough and the non-linearities of the governing equations and the boundary conditions must be taken into account. [54] Nevertheless, simplifying assumptions have to be made, since solving equations with non-linear terms is challenging. [30] Stokes wave theory yields reasonable results if a finite-amplitude wave with small wave steepness in deep water is assumed. [35]

In general, the solution of the Stokes wave theory can be derived by applying Fourier expansion to the boundary conditions of the free surface 3.13 and 3.15. This yields a set of nonlinear algebraic equations for the Fourier coefficients of the free surface, which are derived by perturbation theory. [67] The order of the Stokes wave theory is determined depending on the number of perturbation terms. [30]

The first order Stokes wave theory assumes a sinusoidal wave described by equation 3.1, having an infinitesimal wave height ($A \to 0$). This assumption allows the boundary conditions on the free surface 3.13 and 3.15 to be developed into a Taylor series around the still water level. [9] The wave elevation 3.34 and the boundary conditions on the free surface 3.35 and 3.36 for the first order Stokes theory are derived by neglecting terms of higher order than H. [30]

$$\eta_{first} = -\frac{1}{g}\frac{\partial \phi_{first}}{\partial t} \tag{3.34}$$

$$\frac{\partial \phi_{first}}{\partial z} = \frac{\partial \eta_{first}}{\partial t} \tag{3.35}$$

$$\frac{\partial^2 \phi_{first}}{\partial t^2} + g\frac{\partial \phi_{first}}{\partial z} = 0 \tag{3.36}$$

The first-order wave components of Stokes wave theory are derived from the above approximations and are given by 3.37 and 3.38. [35]

$$\eta_{first} = A\cos(kx - \omega t) \tag{3.37}$$

$$\phi_{first} = \frac{gA}{\omega} \frac{\cosh\left(k(z+h)\right)}{\cosh\left(kh\right)} \sin\left(kx - \omega t\right) \tag{3.38}$$

The fifth-order Stokes waves are often used to determine the maximum surface displacement and the maximum velocity and acceleration. [36] Further, real waves are modelled more accurately using fifth-order Stokes waves than using first-order waves. [57]
Hereafter, the universal solution for fifth-order Stokes waves will be derived.
The potential function ϕ is approximated with a Fourier series 3.39. This expression satisfies the Laplace equation 3.8 and the boundary condition on the sea bed 3.11. [21] Thereby, $\overline{u}$ describes the universal current. [67]

$$\phi = \overline{u}x + \frac{c}{k} \sum_{n=1}^{\infty} \phi_n \cosh\left[nk(h+z)\right] \sin\left[n(kx - \omega t)\right] \tag{3.39}$$

Additionally, the free surface η is approximated by a power series 3.40. [67]

$$\eta = \eta_0 + \sum_{n=1}^{\infty} \eta_n \cos\left[n(kx - \omega t)\right] \tag{3.40}$$

Inserting the potential function 3.39 in the boundary conditions of the free surface 3.13 and 3.15 yield the approximation for the kinematic boundary condition 3.41 and the dynamic boundary condition 3.42. The algebraic transformation for ϕ_n is introduced as $(1 - \frac{\overline{u}}{c})\varphi_n$ and simplifies arithmetic operations. [67]

$$k\eta = \sum_{n=1}^{\infty} \varphi_n \sinh\left[nk(h+\eta)\right] \cos\left[n(kx - \omega t)\right] \tag{3.41}$$

$$\begin{aligned}
&- (c - \overline{u})^2 \sum_{n=1}^{\infty} n\varphi_n \cosh[nk(h+\eta)] \cos\left[n(kx - \omega t)\right] \\
&+ \frac{1}{2}(c - \overline{u})^2 \{\sum_{n=1}^{\infty} n\varphi_n \cosh\left[nk(h+\eta)\right] \cos\left[n(kx - \omega t)\right]\}^2 \\
&+ \frac{1}{2}(c - \overline{u})^2 \{\sum_{n=1}^{\infty} n\varphi_n \sinh\left[nk(h+\eta)\right] \sin\left[n(kx - \omega t)\right]\}^2 \\
&+ g\eta = gz_0 - \frac{1}{2}\overline{u}^2
\end{aligned} \tag{3.42}$$

The obtained equations 3.41 and 3.42 are further modified by limiting the Fourier series

to five terms ($n = 5$) and expanding the hyperbolic functions at the sill water level as the Taylor series. Thus, six equations for the free surface are obtained by the kinematic boundary condition 3.41. Inserting these equations in the expression derived from the dynamic boundary condition 3.42 yields six more equations for the free surface η. Finally, the free surface η in those twelve equations is approximated by the power series 3.40 which is truncated at $n = 5$. [67]

Therefore, the Fourier coefficients of the free surface and potential function can be derived from this set of nonlinear algebraic equations using perturbation theory. Thereby, a perturbation expansion of the velocity potential ϕ 3.43, the water elevation η 3.44 and the current 3.45 are developed as a Fourier series with respect to a non dimensional small perturbation parameter ε, which is also truncated at $m = 5$. [30]

$$\varphi_n = \sum_{m=1}^{5} \varphi_{nm} \varepsilon^m \tag{3.43}$$

$$\eta_n = \sum_{m=1}^{5} \eta_{nm} \varepsilon^m \tag{3.44}$$

$$(c - \overline{u})^2 = \sum_{m=0}^{5-1} c_m^2 \varepsilon^m \tag{3.45}$$

These approximations 3.43, 3.44, and 3.45 are inserted in the obtained set of nonlinear algebraic equations. Solving this system of equations yield the coefficients, which can be withdrawn from the literature [67]. The universal solution of the fifth order Stokes wave theory is given by 3.46, 3.47 and 3.48. [67]

$$\begin{aligned}
\eta_{fifth} =& \eta_0 + \varepsilon \left(\eta_{11} + \varepsilon\eta_{12} + \varepsilon^2\eta_{13} + \varepsilon^3\eta_{14} + \varepsilon^4\eta_{15}\right) \cos\left(kx - \omega t\right) \\
&+ \varepsilon^2 \left(\eta_{22} + \varepsilon\eta_{23} + \varepsilon^2\eta_{24} + \varepsilon^3\eta_{25}\right) \cos 2(kx - \omega t) \\
&+ \varepsilon^3 \left(\eta_{33} + \varepsilon\eta_{34} + \varepsilon^2\eta_{35}\right) \cos 3(kx - \omega t) \\
&+ \varepsilon^4 \left(\eta_{44} + \varepsilon\eta_{45}\right) \cos 4(kx - \omega t) \\
&+ \varepsilon^5 \eta_{55} \cos 5(kx - \omega t))
\end{aligned} \tag{3.46}$$

$$\begin{aligned}\phi_{fifth} =& \bar{u}x + \frac{c-\bar{u}}{k}\left\{\varepsilon\left(\varphi_{11}+\varepsilon\varphi_{12}+\varepsilon^2\varphi_{13}+\varepsilon^3\varphi_{14}+\varepsilon^4\varphi_{15}\right)\cosh\left[k(h+z)\right]\sin\left(kx-\omega t\right)\right.\\ &+\varepsilon^2\left(\varphi_{22}+\varepsilon\varphi_{23}+\varepsilon^2\varphi_{24}+\varepsilon^3\varphi_{25}\right)\cosh\left[2k(h+z)\right]\sin 2(kx-\omega t)\\ &+\varepsilon^3\left(\varphi_{33}+\varepsilon\varphi_{34}+\varepsilon^2\varphi_{35}\right)\cosh\left[3k(h+z)\right]\sin 3(kx-\omega t)\\ &+\varepsilon^4\left(\varphi_{44}+\varepsilon\varphi_{45}\right)\cosh\left[4k(h+z)\right]\sin 4(kx-\omega t)\\ &\left.+\varepsilon^5\varphi_{55}\cosh\left[5k(h+z)\right]\sin 5(kx-\omega t)\right\}\end{aligned} \tag{3.47}$$

$$(c-\overline{u})^2_{fifth} = c_0^2+\varepsilon c_1^2+\varepsilon^2 c_2^2+\varepsilon^3 c_3^2+\varepsilon^4 c_4^2 \tag{3.48}$$

Hereby, the perturbation parameter is considered global. Different definitions of the perturbation parameter have been suggested. Thus, different Stokes solutions are yielded. [67] Defining the perturbation parameter as a product of the wave number and the wave amplitude $\varepsilon = kA$ yields a Stokes theory for small wave steepness and deep water. [30] In general it is also applicable for intermediate water, but the solution converges more slowly for decreasing water depth. [52]

3.7 Wave energy

Since a wave energy converter extracts energy from water waves, a mathematical description of the energy provided by the waves will be derived in this chapter. In order to achieve this, a control volume perpendicular to the direction of the wave propagation is introduced. It delimits the fluid with vertical sides and bounds it above by the free surface and below by the seabed. The control volume moves with constant velocity U in the direction of the wave propagation. [49]

The total energy contained in a propagating wave is composed of kinetic and potential energy. [41]

$$E_{tot} = E_k + E_p = \rho \iiint_V \left(\frac{1}{2}\mathbf{v}^2 + gz\right) dV \tag{3.49}$$

These two quantities are averaged in space over a unit area and in time over one wave period resulting in the mean kinetic energy density 3.50 as well as the mean potential

energy density 3.51 of the water under the free surface. Equations 3.50 and 3.51 are simplified by substituting the wave elevation and the water particle velocity, yielded by the linear wave theory. Further, constant deep water is assumed. [62] The mean potential energy density of the fluid below the still water level is neglected ($-h < z < 0$), as it does not contribute to the wave motion. [33] This results in the equipartition of energy since the kinetic and the potential energy density are identical when averaged over a wave period. [62]

$$\overline{E_k} = \frac{1}{T}\int_0^T \frac{\rho}{2}\int_{-h}^{\eta} \mathbf{v}^2 dzdt = \frac{\rho g H^2}{16} \tag{3.50}$$

$$\overline{E_p} = \frac{1}{T}\int_0^T \rho g \int_0^{\eta} z dzdt = \frac{\rho g H^2}{16} \tag{3.51}$$

The total mean energy density of a propagating wave 3.52 is given by the sum of mean kinetic and mean potential energy density in the fluid. [41]

$$\overline{E_{tot}} = \overline{E_k} + \overline{E_p} = \frac{1}{T}\int_0^T \rho \int_{-h}^{\eta} (\frac{1}{2}\mathbf{v}^2 + gz) dzdt = \frac{\rho g H^2}{8} \tag{3.52}$$

The time derivative of the total wave energy represents the wave energy flux P. It can be interpreted as the power of the dynamic pressure of the wavefront exerted on the vertical section per unit width over one wave period. [62] Applying the transport theorem to the time derivative of the total energy yields equation 3.53. [41]

$$\begin{aligned} P = \frac{dE_{tot}}{dt} =& \rho \frac{d}{dt} \iiint_V (\frac{1}{2}\mathbf{v}^2 + gz) dV \\ =& \rho \iiint_V \frac{\partial}{\partial t}(\frac{1}{2}\mathbf{v}^2 + gz) dV + \rho \iint_S (\frac{1}{2}\mathbf{v}^2 + gz) U_n dS \end{aligned} \tag{3.53}$$

Taking into account that the vertical coordinate z does not contribute to the integrand of the last volume integral as it is independent of time, the kinetic energy term in equation 3.53 can be rewritten using Laplace's equation and the divergence theorem. Further, the wave energy is transmitted only across the vertical control surface since the bottom and the free surface do not contribute to the wave energy flux. Additionally, the control volume moves with constant velocity $U_n = U$. Thus, the mean rate of the

wave energy flux can be rewritten as 3.54. [41]

$$\overline{P} = \rho \frac{1}{T} \int_0^T \int_{-h}^{\eta} \frac{\partial \phi}{\partial t} \frac{\partial \phi}{\partial x} + (\frac{1}{2}\mathbf{v}^2 + gz) U dz dt \tag{3.54}$$

Setting the position of the control volume to $x = 0$ and the velocity at which the control volume moves to $U = 0$, equation 3.54 is simplified to equation 3.55. [41]

$$\overline{P} = \rho \frac{1}{T} \int_0^T \int_{-h}^{\eta} \frac{\partial \phi}{\partial t} \frac{\partial \phi}{\partial x} dz dt \tag{3.55}$$

Assuming linear wave theory, the mean wave energy flux is specified as the product of the mean total energy and the group velocity. [49]

$$\overline{P} = \frac{1}{8} \rho g H^2 c (\frac{1}{2} + \frac{kh}{\sinh 2kh}) = c_g \overline{E_{tot}} \tag{3.56}$$

3.8 Wave-structure interaction

The effect of ocean waves on the wave energy converter is of great interest as it determines the motion of the device. A cartesian coordinate system originating in the center of gravity of the immersed device is introduced, whose z-axis points upwards and the x-y plane is horizontal. The device moves with six degrees of freedom as shown in figure 3.5. [20] Forces cause the translational motion to surge, sway, and heave in x-, y-, and z-direction and moments cause the rotational motion to roll, pitch, and sway around the x-, y-, and z-axis. [7]

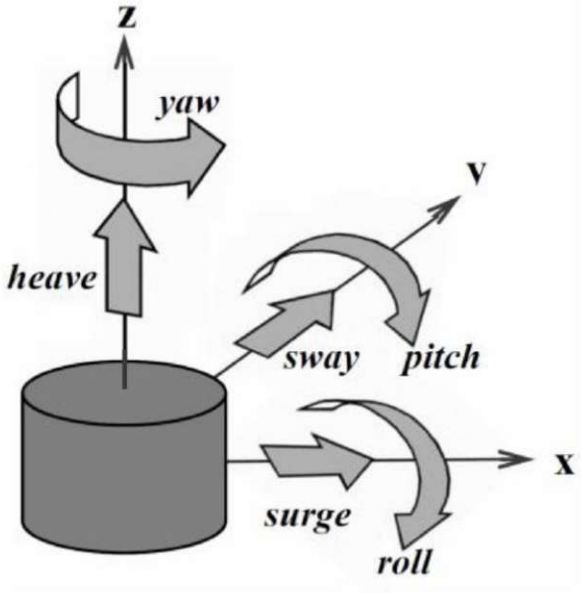

Figure 3.5 – Motions of a floating body [56]

The dynamic equation for the translational and rotational motion of a rigid body is derived from second Newton's law of motion. [56] A wave energy converter experiences, among others, hydrodynamic force $\mathbf{f}_{hd}$ which is composed of an radiation and an excitation force. Further, the buoyancy force $\mathbf{f}_{hs}$ as well as the force of the power-take-off system $\mathbf{f}_{PTO}$ influence the motion of the device. Additionally, forces due to the mooring system $\mathbf{f}_m$, viscous effects $\mathbf{f}_v$ and frictional losses $\mathbf{f}_f$ act on the wave energy converter and are neglected as their influence is marginal. [5] These forces cause a displacement $\mathbf{s}$ from the equilibrium position of the wave energy converter with the mass m. [20]

$$m\ddot{\mathbf{s}} = \sum \mathbf{f} = \mathbf{f}_{hd} + \mathbf{f}_{hs} + \mathbf{f}_{PTO} + \mathbf{f}_m + \mathbf{f}_v + \mathbf{f}_f \tag{3.57}$$

$$\mathbf{J}\dot{\omega} = \sum \mathbf{m} \tag{3.58}$$

The forces and moments acting on a floating and submerged device are resolved with a linear approach. The balance between buoyancy and gravity yields the hydrostatic buoyancy force. It is derived by the linearization of the integral of the hydrostatic pressure distribution over the body's surface which results in 3.59. [22] The coefficients of the buoyancy stiffness matrix $\mathbf{C}$ serve as proportionality constants between the buoyancy force and the displacement of the body $\mathbf{s}$ from its equilibrium position. [20]

$$\mathbf{f}_{hs} = -\mathbf{C}\mathbf{s} \tag{3.59}$$

The force applied by the power-take-off system has two contributions to the device when a linear approach is assumed. The contribution proportional to the displacement $\mathbf{C_{PTO}}$ of the body in 3.60 represents a spring, whereas the contribution proportional to the velocity of the displacement $\mathbf{B_{PTO}}$ describes a damper. [22]

$$\mathbf{f}_{PTO} = -\mathbf{B_{PTO}}\dot{\mathbf{s}} - \mathbf{C_{PTO}}\mathbf{s} \tag{3.60}$$

The hydrodynamic force $\mathbf{f}_{hd}$ and the moment result from the pressure of the fluid and the shear stress acting on the submerged surface of the device. The contribution of shear forces is negligible, whereby the hydrodynamic forces and moments are given by 3.61. [50] The pressure on the wetted surface of the device can be rewritten using Bernoulli's equation and neglecting higher-order terms to ensure linearity. [22]

$$\begin{aligned} \mathbf{f_{hd}} &= \int_S p\mathbf{n}dS = -\rho \int_S \frac{\partial \phi}{\partial t}\mathbf{n}dS \\ \mathbf{m_{hd}} &= \int_S p(\mathbf{r} \times \mathbf{n})dS \end{aligned} \tag{3.61}$$

Within the linear wave theory for deep water, a plane progressive wave of small amplitude with sinusoidal time dependence is assumed as an incident wave. [41] Its velocity potential ϕ is given by 3.17 which is further simplified to 3.62. This represents a decomposition into a spatial complex amplitude and a sinusoidal time dependence. [22]

$$\phi(x, y, z, t) = \Re[\hat{\phi}(x, y, z)e^{i\omega t}] \tag{3.62}$$

In the course of linear theory, the velocity potential must satisfy the boundary conditions on the sea bed 3.12 and the free water surface 3.14 and 3.16. If a body is immersed in the fluid, two additional conditions must be taken into account. [50] First, the component of the fluid velocity normal to the body surface u_n must be equal to the body velocity in the direction normal to its surface. This is described by the linearized impermeable boundary condition 3.63. [22]

$$\frac{\partial \phi}{\partial n_b} = u_n \tag{3.63}$$

Second, the wave field far from the body should appear similar to the incident wave field. This condition is referred to as radiation condition 3.64. Applying the energy conservation principle yields the velocity potential which satisfies the radiation condition. This velocity potential must decay proportional to the radial distance r from the body. [22]

$$\phi \propto (kr)^{-\frac{1}{2}} e^{-ikr} \quad r \to \infty \tag{3.64}$$

Further, the linear theory generally allows for superposition of solutions. On the one hand, a superposition of regular waves leads to a more realistic irregular wave pattern. [41] On the other hand, the complex velocity potential $\hat{\phi}$ can be decomposed into an incident, a diffracted, and a radiated velocity potential. [6]

$$\hat{\phi} = \hat{\phi}_I + \hat{\phi}_D + \hat{\phi}_R \tag{3.65}$$

The time dependence of the hydrodynamic force can be removed by substituting equation 3.62 in 3.61. [5] Then, the decomposition of the velocity potential 3.65 is applied to the hydrodynamic force resulting in equation 3.66. Thereby, the hydrodynamic force is decomposed into the excitation force $\mathbf{f_{ex}}$ and the radiation force $\mathbf{f_{rad}}$. [22]

$$\mathbf{f_{hd}} = \mathbf{f_{ex}} + \mathbf{f_{rad}} = -i\omega\rho \int_S \hat{\phi}\mathbf{n}dS = -i\omega\rho \int_S (\hat{\phi}_I + \hat{\phi}_D)\mathbf{n}dS - i\omega\rho \int_S \hat{\phi}_R \mathbf{n}dS \tag{3.66}$$

The excitation force 3.67 occurs through a rigid fixed body subjected to incident waves. It is further divided into the Froude-Krylov force $\mathbf{f_{FK}}$ and the diffraction excitation force $\mathbf{f_D}$. [20]

$$\mathbf{f_{ex}} = \mathbf{f_{FK}} + \mathbf{f_D} = i\omega\rho \int_S \hat{\phi}_I \mathbf{n}dS + i\omega\rho \int_S \hat{\phi}_D \mathbf{n}dS \tag{3.67}$$

The force due to the incident velocity potential $\hat{\phi}_I$ is the Froude-Krylov force. $\hat{\phi}_I$ represents a plane propagating wave that is not disturbed by any bodies. It is given by 3.68 and depends on the angle β between the direction of propagation of the incident

wave and the positive x-axis. [6]

$$\hat{\phi}_I = \frac{igA}{\omega}\frac{\cosh k(z+h)}{\cosh kh}e^{-ik(x\cos\beta+y\sin\beta)} \tag{3.68}$$

The diffraction excitation force results from the diffracted velocity potential $\hat{\phi}_D$ which originates from the interaction of the incident wave and a motionless body. The boundary condition on the body 3.63 must be adapted to a fixed body which results in the solid body boundary condition 3.69. [50]

$$\frac{\partial\phi}{\partial n_b} = \frac{\partial\hat{\phi}_D}{\partial n_b} + \frac{\partial\hat{\phi}_I}{\partial n_b} = 0 \tag{3.69}$$

In the case of an incident wave upon a vertical wall at $x = 0$, the diffracted wave is given by a diffracted wave and the diffracted velocity potential is given by equation 3.70. Since a body whose dimensions are small compared to the wavelength is assumed to not disturb the incident wave field severely, the diffraction excitation force can be neglected. Thus, the Froude-Krylov force seems to be a reasonable approximation to the excitation force. [20]

$$\hat{\phi}_D = \frac{igA}{\omega}\frac{\cosh k(z+h)}{\cosh kh}e^{ik(x\cos\beta+y\sin\beta)} \tag{3.70}$$

The radiated velocity potential results from the motion of a body in calm waters. Allowing the body to move in all six degrees of freedom, the radiated velocity potential can be rewritten as a superposition of radiated waves generated due to each of the six oscillation modes. [20] This results in 3.71. Thereby, the unit velocity u_j of the body which oscillates in mode j is proportional to the radiated velocity potential and is associated with the proportionality constant $\varphi_{R\,j}$ which corresponds to the complex amplitude of the radiated velocity potential. [5]

$$\hat{\phi}_R = \sum_{j=1}^{6} \varphi_{R\,j} u_j \tag{3.71}$$

The component k of the radiation force acts on the body which oscillates in mode j. Associating the radiation force with the radiated velocity potential gives equation 3.72. [22]

$$f_{rad,k} = i\omega\rho \int_S \hat{\phi}_{R\ j} n_k dS = i\omega\rho \int_S \varphi_{R\ j} u_j n_k dS = -Z_{j,k} u_j \tag{3.72}$$

It can be rewritten by introducing the radiation impedance 3.73, which is further modified using the body boundary condition 3.63. The radiation impedance can be divided into a real and an imaginary part. [20] The real part $\mathbf{R}$ is referred to as the damping coefficient matrix and corresponds to the dissipative effect due to the transmission of energy from the oscillating body to the water causing the energy to propagate away from the body. The imaginary part $\mathbf{X}$ is called the radiation reactance matrix. Water experiences an increase in kinetic energy and gravitational potential energy due to wave motions. The difference between the average added kinetic and potential energy is described by the radiation reactance matrix. As the energy stored in the water flows into the mechanical system and back out into the surrounding water, the reactive effect is established by the harmonic response of the system. The radiation impedance can be rewritten further as the radiation reactance matrix depends on ω. Thereby, the added mass coefficient $\mathbf{A}$ is introduced which describes an inertial increase that is attributed to water displacement close to the body due to body motion. [22]

$$Z_{j,k} = -i\omega\rho \int_S \varphi_{R\ j} n_k dS = R_{j,k} + iX_{j,k} = R_{j,k} + i\omega A_{j,k} \tag{3.73}$$

Considering all important forces and rearranging equation 3.58 leads to the equation of a forced damped oscillator 3.74. The amplitude of the body motion $\mathbf{s}$ can be determined with the aid of this equation. [5]

$$(\mathbf{M} + \mathbf{A})\ddot{\mathbf{s}} + (\mathbf{R} + \mathbf{B_{PTO}})\dot{\mathbf{s}} + (\mathbf{C} + \mathbf{C_{PTO}})\mathbf{s} = \mathbf{f_{ex}} \tag{3.74}$$

4

Power-take-off systems

The power-take-off system is the key component of the wave energy converter. [23] It performs the secondary energy conversion stage which converts the absorbed wave energy into useful mechanical energy and then into electricity. [56] Thereby, the main objective of wave energy converters can be achieved. [19]

The power-take-off system contributes to the mass and the size of the wave energy converter, which influences the structural dynamics of the wave energy converter and therefore the overall performance. [2] Further, the power-take-off system determines the efficiency and the reliability of the power conversion and therefore the annual energy production. This in turn affects the operation and maintenance cost and determines the availability of wave energy. Therefore, 20 - 30 % of the total capital cost of a wave energy converter is related to the power-take-off system. All points considered, the power-take-off system contributes considerably to the levelised cost of energy, which decreases with an increase in efficiency and reduction in the cost of the power-take-off system. Hence, designing an efficient and economically competitive power-take-off system is crucial to improving wave energy conversion technology. [45]

4.1 Challenges of power-take-off systems

Just like wave energy converters power-take-off systems face some significant challenges. Robustness, reliability, and minimal maintenance are required for both the wave energy converter and the power-take-off system. This is due to the harsh environment, adverse weather conditions, and difficult accessibility of the operating site of wave energy converters. [45]

Not only the structure of the wave energy converter but especially the power-take-off

systems must cope with the irregular nature of ocean waves and withstand high forces. [2] So, the main challenge is to convert the random, high-force oscillatory motion into a smooth motion that drives a generator. [16] The ocean waves induce a slow oscillating motion combined with high forces to the wave energy converter and subsequently to the power-take-off system. Nevertheless, the electric motor requires a smooth and fast rotatory motion in one direction. [45] To convert the oscillating into a rotatory movement, the captured intermittent wave energy is temporarily stored and smoothened with the aid of the power-take-off system. [2]

One of the main challenges in developing power-take-off systems is to reproduce the effect of the power-take-off system at a laboratory scale. The power-take-off system is either substituted with a miniaturized power-take-off system, which produces little amounts of electricity, or modelled with an active damper element, which simulates the power-take-off reaction forces. Both approaches lead to uncertainties caused by unpredictable friction losses between moving parts, signal noise, instrument resolution, accuracy, repeatability, and multiple sensors. To limit and quantify these uncertainties, the laboratory-scale power-take-off system must be constructed using common practices and known theories. Thereby, correct calibration and characterization of the power-take-off damping are conducted in early tests. [23]

4.2 Types of power-take-off systems

Several concepts of power-take-off systems have already been developed to maximize power output while minimizing costs. [3] Thus, the type of the wave energy converter is decisive as the wave energy absorbed in the primary energy conversion stage is different depending on the type of the wave energy converter. Since different kinds of absorbed energy must be transformed into useful mechanical energy, different concepts of power-take-off systems are required. Consequently, the development of various types of wave energy converters is accompanied by several concepts of power-take-off systems. [56] Figure 4.1 illustrates the various concepts of power-take-off systems, with the turbine transfer, the hydraulic motor, as well as direct drive methods being the most used techniques. [3]

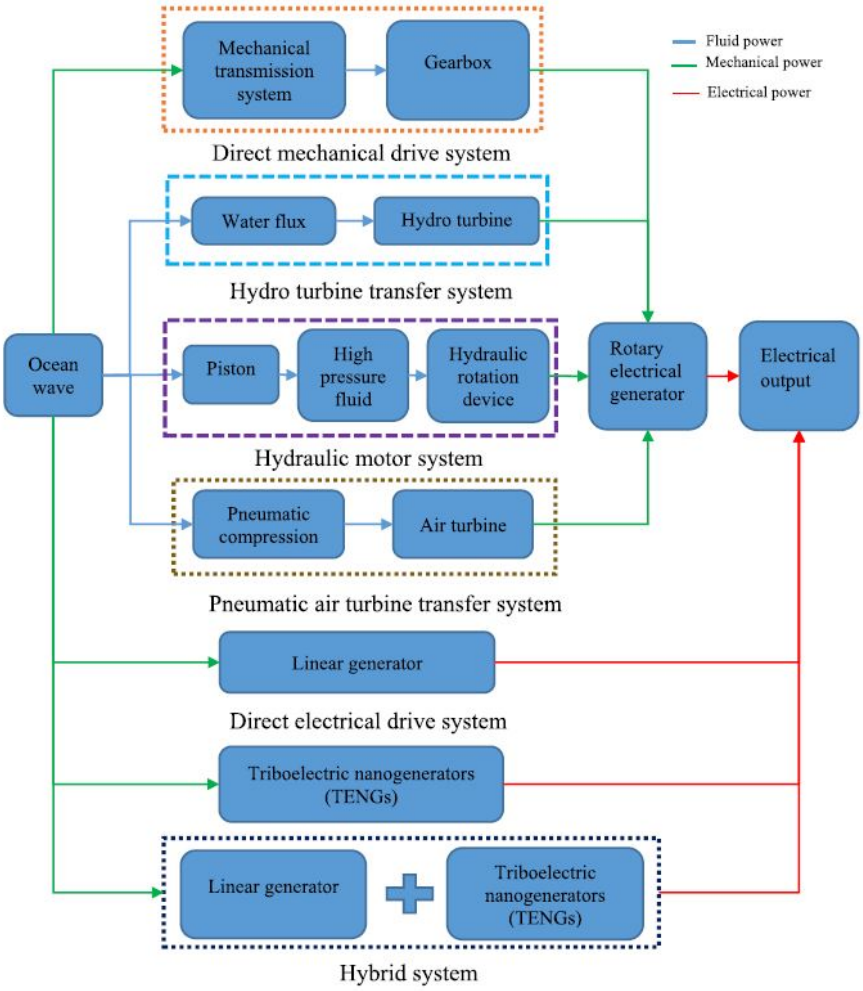

Figure 4.1 – Overview of different concepts of power-take-off systems [3]

The hydro turbine transfer system is similar to a hydroelectric power generation system and is employed in overtopping energy devices. [66] Since this concept has been in use in hydropower plants for many years, this technology is quite mature. [24] Additionally, hydro turbines have the advantage of requiring little maintenance while operating with an excess of 90 % efficiency. Further, environmental problems caused by leaking fluids can be disregarded. [3] Overtopping devices capture wave energy in the form of potential energy by accumulating water in a reservoir. [45] The difference in potential energy makes the water flow out of the reservoir whereby it drives the hydro turbine which in term directly drives the generator to produce electricity. [66] However, the hydro turbine requires a certain head and flow to be economical. This represents a significant challenge as energy extraction from ocean waves can only provide the head and flow to a certain degree. [3] Different types of hydro turbines such as the Pelton turbine, the

Kaplan turbine, and the Francis turbine are employed in overtopping energy devices. [66]

The Pelton turbine is an impulse turbine whose working principle is shown in figure 4.2. A nozzle injects water, whereby a jet is generated. Hence, the pressure acting on the water in the nozzle is converted into velocity. This water jet is directed towards the bucket-shaped blades of the runner which turns in the atmosphere. [15] Thus, the kinetic energy of the water is transferred to the turbine which converts the kinetic energy into mechanical energy by rotating. [19].

The Kaplan turbine is an axial hydro turbine, which is represented in figure 4.2. [15] The water flow to the runner is regulated by fixed and adjustable vanes. The runner is enclosed within a pressure casing and is fully immersed in water. It rotates axially and the blades are adjustable such that the turbine is suitable for low flow conditions and high flow conditions. [45] The Kaplan turbine is suitable for low flow conditions and is therefore used for wave energy converters. On the other hand, the Francis turbine is not employed in wave energy converters as it is more applicable to high water heads. However, both the Kaplan and the Francis turbine use the working principle of reaction turbines where the pressure differential created on the rotor blades turns the rotor. [19]

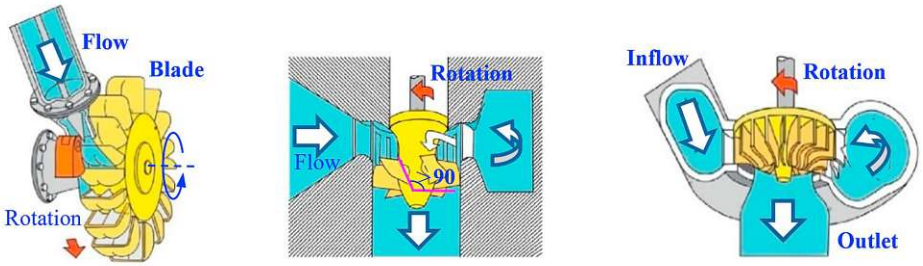

Figure 4.2 – Overview of different hydro turbines: Pelton turbine (left), Kaplan turbine (middle), Francis turbine (right) [66]

The air turbine is installed as a power-take-off system in oscillating water columns and provides several advantages. Besides having no environmental impact due to leakage, the air turbine can be located such that it is easily accessible for maintenance and is not affected by the corrosive salt water and destructive high waves. [3] The air turbine is driven by the oscillating air flow originating from the fluctuating air pressure and kinetic energy in the enclosed chamber which in turn results from the irregular nature of ocean waves. [45] Thereby, the slow velocity of ocean waves is transformed into

high air flow rates. [3] However, the bidirectional air flow entails a major disadvantage as conventional turbines have steering restrictions. They can only be employed in combination with non-returning valves since the air flow must be rectified. This implies a complicated configuration, high maintenance, and costs. Self-rectifying air turbines offer a viable alternative as the alternating air flow is converted into a unidirectional rotation. Several types of self-rectifying air turbines have already been proposed. [45] Thereby, the Wells turbine, the self-rectifying impulse turbine, and the Denniss-Auld turbine are the most often used concepts and are shown in figure 4.3. [66]

The Wells turbine is considered one of the simplest and most economical axial flow turbines for wave energy conversion. Compared to other turbines, the Wells turbine can generate energy even at low airflow rates and still achieve good efficiency. [55] It consists of several symmetrical aerofoil blades positioned around a hub with its chord planes normal to the axis of rotation. There are no rectifying air valves required as the Wells turbine is self-rectifying due to the symmetry of the aerofoil blades. When an aerofoil is exposed to the fluid flow at a certain incident angle α, a lift force L_f normal to the free stream and a drag force D_f parallel to the free stream is induced. These forces can be decomposed into tangential and axial components. The sign of the incident angle α generally depends on the direction of the airflow. In the case of a symmetrical aerofoil, the direction of the tangential force is the same for positive and negative values of the incident angle α. Thereby, the symmetrical aerofoils positioned around an axis of rotation cause the self-rectifying effect as they always rotate in a single direction regardless of the direction of the airflow. [47] However, the rotor of the Wells turbine must be initially accelerated by an external source of energy. [45]

The impulse turbine is developed to overcome this disadvantage. [45] Its rotor consists of two rows of guide vanes which are positioned symmetrically on both sides of the rotor representing a reflection of each other with respect to a plane through the rotor disk. [55] The self-rectifying effect is achieved due to this specific arrangement of the guide vanes. Thereby, the airflow is redirected by the guide vanes such that the kinetic energy of the airflow is directly transferred into the tangential force component on the rotor blades. The guide vanes can be fixed or pitched and the pitching mechanism can be self-controlled by the airflow or controlled by another active mechanism. Thus, the design of the impulse turbine is more complex, whereby the reliability decreases while

the operation and maintenance costs increase. [45]

The Dennis-Auld turbine is a further development of the Wells turbine. The aerofoil blades of the Dennis-Auld turbine rotate around their neutral position to realize the self-rectifying effect. [45]

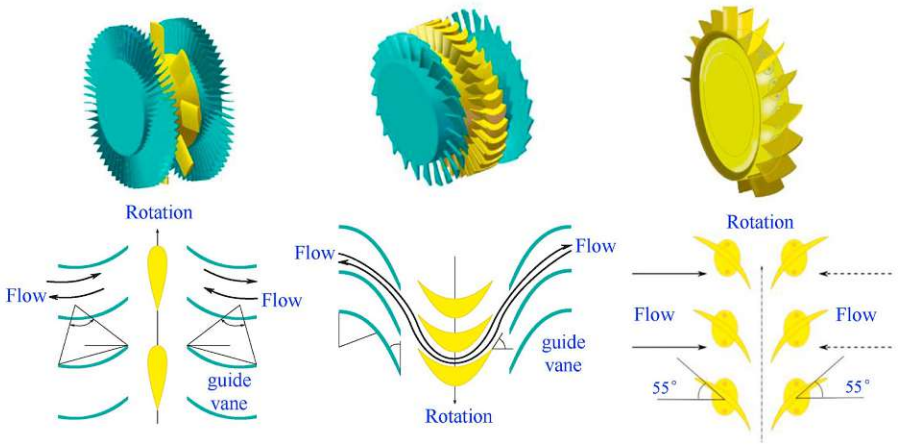

Figure 4.3 – Overview of different self-rectifying air turbines: Wells turbine (left), Impulse turbine (middle), Dennis-Auld turbine (right) [66]

The hydraulic motor-based power-take-off system is employed in wave-activated bodies to convert the wave-induced translational and rotational motion of the body into electricity. [56] Hydraulic converters are well suited for wave energy conversion as they harness large amounts of power while being able to handle the low-speed oscillating motion of ocean waves combined with high forces. The already high efficiencies can be further increased by using an incompressible fluid resulting in efficiencies of up to 80 %. However, hydraulic converters pose a risk to the marine environment, as hydraulic oil can leak from the system. Also, the hydraulic system consists of a lot of mechanical moving parts, which require regular system maintenance. Another point to consider is that unexpected extreme conditions can cause damage to the system if the maximum displacement limit of the hydraulic actuator is reached. [3]

The working principle of a hydraulic converter is shown in figure 4.4. The wave-induced motion of a wave-activated body activates a hydraulic ram or a piston. Thereby, hydraulic oil enters the circuit under high pressure and passes multiple check valves. These check valves are designed like rectifiers so that the hydraulic oil always flows in one direction regardless of the motion of the piston. The hydraulic fluid is guided to a high-pressure accumulator, where it is temporarily stored. Thereby, fluctuations in pressure are absorbed and the flow of the hydraulic fluid is smoothened to ensure a

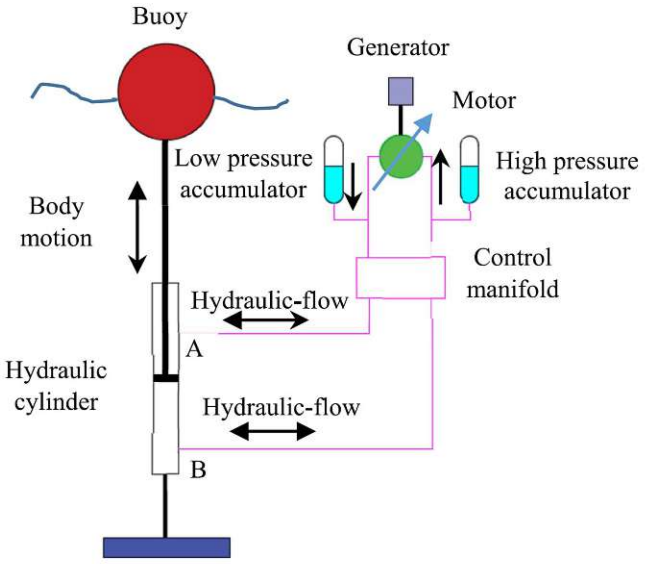

Figure 4.4 – Working principle of a hydraulic motor-based power-take-off system [3]

smooth flow rate and thus deliver a steady electrical output. The flow is subsequently directed to the hydraulic motor where the hydraulic energy is converted into mechanical energy. Thereby, the control of the flow determines the power output and the efficiency of the device. In addition to the high-pressure accumulator, several control strategies have been developed and employed to improve efficiency. The mechanical energy is further converted into electrical energy by the generator which is directly connected to the hydraulic motor. A low-pressure accumulator supplies low pressure in the return line to prevent cavitation. [19]

Another possibility to convert the wave-induced motion of the body into electricity is the direct drive systems. Two main types are distinguished. [56] The direct mechanical drive system shown in figure 4.5 is characterized by converting the mechanical energy generated by the wave-induced motion of the body directly into electricity. Thereby, the mechanical system converts a linear into a rotatory motion to drive the generator. [45] The mechanical system consists of a gearbox, pulleys, cables, and, if applicable, a flywheel and is directly coupled with the generator without any pneumatic or hydraulic systems. As no hydraulic system is employed, friction is reduced whereby more wave energy is transferred to the direct mechanical drive system. [3] Further, only up to three energy conversions are necessary which results in high efficiency. However, the direct mechanical drive system is subjected to uncountable load cycles leading to doubtful reliability, short lifetime, and high maintenance costs. [45]

The Crestwing wave energy converter employs a direct mechanical drive system. Thereby, the linear motion of the two floating wave-activated bodies relative to each other is transformed into a rotatory motion by moving a push rod over a cogwheel which is connected to the generator. A more detailed description of the power-take-off system of the Crestwing wave energy converter is provided in chapter 5.3. [13]

The direct electrical drive system connects the wave-activated body directly to the moving part of a linear electric generator. Therefore, no intermediate mechanical interface is required whereby losses are avoided and maintenance costs are reduced. The concept of the direct electrical drive system is shown in figure 4.6 and is based on the use of a translator and a stator. The translator comprises alternating polarity magnets and is coupled to the wave-activated body, whereas the stator is equipped with coil windings and fixed on the seabed. [3] A heaving motion is induced by the ocean waves, whereby the translator moves relatively to the stationary stator. [45] Hence, a magnetic field inside the coil windings is created which in turn produces electricity. Since the generated electricity originates from the wave-induced motion of the body, rectification by power electronics is required to be suitable for the electric grid. Thus, the power transmission system is very complicated. Further, the low frequencies of the ocean waves lead to linear velocities of the translator which are much lower than the velocity of conventional rotary generators. Additionally, very large machines and a heavy mounting structure are needed to endure the forces between the stator and the translator. However, the direct electrical drive system achieves relatively high efficiency and enables continuous force control. [3]

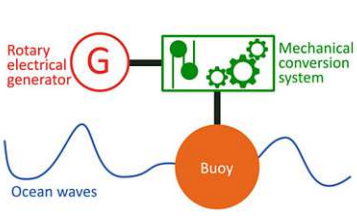

Figure 4.5 – Direct mechanical drive system [45]

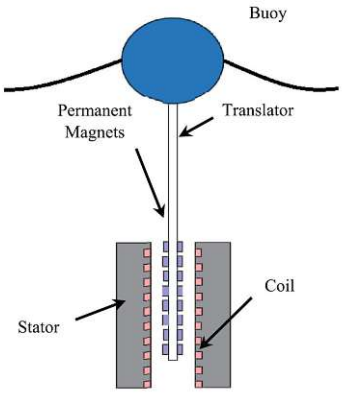

Figure 4.6 – Direct electrical drive system [3]

5

Methodology

This study aims to provide a CFD simulation of the Crestwing wave energy converter. This chapter gives an overview of how the simulation is set up. The CFD simulations are carried out with the commercial CFD software Simcenter STAR-CCM+ 2021.3 from Siemens, which discretizes the unsteady Reynolds-Averaged Navier-Stokes (URANS) equations using the finite-volume method. The CFD simulations will be compared to linear wave theory and experimental data which is obtained by experiments conducted at the Danish Hydraulic Institute (DHI) deepwater basin, which is 30 m long, 20 m wide and 3 m deep. [8] The data processing is performed using Python 3.9.7.

5.1 The Crestwing wave energy converter

The Crestwing wave energy converter consists of two pontoons, which are connected by a hinge. The geometry and dimensions of the device as well as the used coordinate systems are based on [8] and can be seen in figure 5.1.

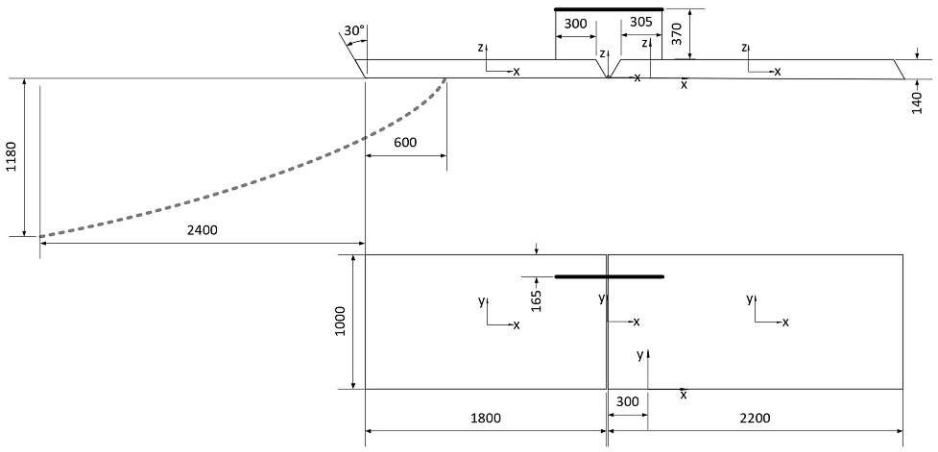

Figure 5.1 – Dimension of the Crestwing wave energy converter

The weight of the device was approximated using Archimedes Principle as the exact data could not be provided. Archimedes Principle states, that a body immersed in fluid experiences a buoyant force equal to the weight of the displaced fluid. [7]

$$\mathbf{f_{hs}} = \iint_S p\mathbf{n}\, dS = \rho \mathbf{g} V \tag{5.1}$$

Equation 5.1 can be derived from Gauss' Theorem. ρV is the weight of the displaced fluid and is equal to the weight of the wave energy converter. [59] The volume of the displaced fluid has been determined using video data of the Crestwing wave energy converter floating on still water. Marks on the device enabled measuring how deep the device was immersed. This resulted in a total mass of $m_{total} = 160\,\text{kg}$. The power-take-off (PTO) system is located on top of the smaller pontoon close to the hinge. Therefore, the weight of the device is inhomogeneously distributed. To simplify the approximation of the characteristics of the two pontoons, the mass distribution of each part is assumed to be homogeneous. In addition to this, the geometry of the device allows calculating the moment of inertia of each pontoon using the moment of inertia of a rectangular box, shown in figure 5.2. [10]

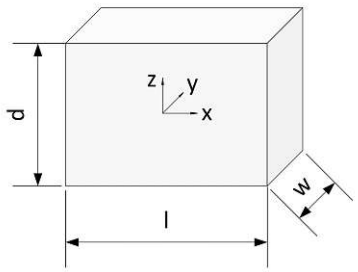

$$J_x = \frac{1}{12} m(w^2 + d^2) \tag{5.2}$$

$$J_y = \frac{1}{12} m(l^2 + d^2) \tag{5.3}$$

$$J_z = \frac{1}{12} m(l^2 + w^2) \tag{5.4}$$

Figure 5.2 – Moment of inertia [10]

The characteristics of each pontoon are summarized in table 5.1.

Table 5.1 – Characteristics of the wave energy converter

	small (left) pontoon	big (right) pontoon
mass m	100.00 kg	60.00 kg
moment of inertia J_x	8.50 kgm^2	5.10 kgm^2
moment of inertia J_y	27.16 kgm^2	24.30 kgm^2
moment of inertia J_z	35.33 kgm^2	29.20 kgm^2

Each pontoon of the wave energy converter experiences translational and rotational motions in all directions due to wave-structure interaction. Therefore, it has six degrees of freedom. The surge, sway, heave, roll, pitch, and yaw motions of the wave energy converter are modelled using the Dynamic Fluid Body Interaction (DFBI) 6 - Degrees of Freedom (DoF) Multi-Body Motion Solver provided by STAR-CCM+.
The two 6-DoF Bodies are connected by a hinge, which is located in the middle of the two pontoons. The hinge is modelled with the built-in revolute joint coupling provided by STAR-CCM+. It only allows a single relative rotation of the two pontoons around the axis of revolution. [57]

5.2 Mooring system

The Crestwing wave energy converter is fixed at the seabed with a flexible three-point anchoring system. It allows the device to rotate 360°. Further, the entire energy potential of the Crestwing wave energy converter can be exploited and the impact of unexpected waves is minimized with this anchoring system. [13] In the experiments conducted by the Danish Hydraulic Institute the anchoring system was modelled by a single-point mooring consisting of a mooring line, damping elements, and a spherical buoyancy element. [8] In this thesis the anchoring system is simulated by the quasi-stationary, elastic catenary coupling provided by STAR-CCM+. [57] It is attached to the small pontoon at 0.6 m from the front edge and continues to a position 1.18 m below the water surface and 2.4 m away from the front edge of the small pontoon, as shown in figure 5.1. The setup of the simulation and the experiments deviate. This is why the characteristics in table 5.2 are approximated so that the mooring system in the simulation and the experiments are comparable.

Table 5.2 – Mooring characteristics

Characteristic	Value
Stiffness	300 N/m
Mass per Unit Length	1 kg/m
Relaxation Length	3.1 m

5.3 Power-take-off system

Crestwing developed an efficient mechanical power-take-off (PTO) system. It is mounted on top of the small pontoon and connects the two barges with a push rod. [8] It moves a toothed rack over a cogwheel. Thereby, the linear movement is transformed into a circular one through a drive-train. This assembly drives the power generator. The rotation increases through a speed-up gear and is stabilized with the aid of a flywheel which smooths the electricity production. [13] A one-way clutch is installed between the toothed rack and the drive-train. It transmits the rotation in only one direction. The power-take-off system of Crestwing is characterized by this one-way motion of the drive-train. [14] The operation mode is shown in figure 5.3.

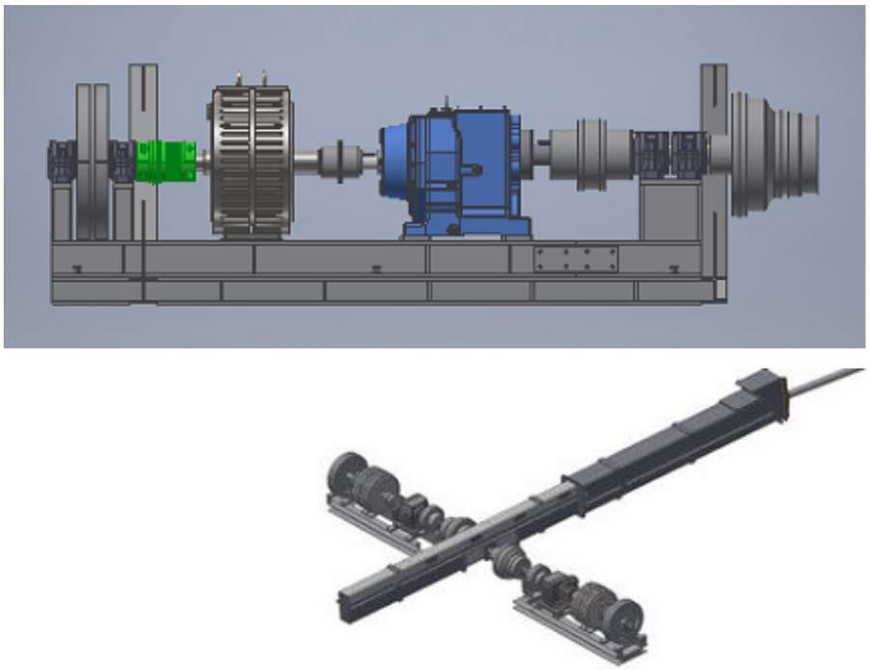

Figure 5.3 – Power-take-off system of the Crestwing wave energy converter [13]

In the experiments at the Danish Hydraulic Institute, the power generator is modelled using a hysteresis brake. [8] Like the generator, the hysteresis brake is driven by the conversion of the linear motion of the push rod into a circular one. The rotation experiences resistance which extracts energy from the movement. Thus, a force equal to the resistance is applied to the push rod in terms of actio reactio. Further, the one-way clutch is replaced by two clutches that control the activation of the brake. [8]

Thereby, the intensity of the brake effect can be adjusted according to the direction of the rotation.

In this simulation, the linear movement of the push rod which is connected to the toothed rack and thereby converted to a circular one is simulated with the built-in spring-damper coupling from STAR-CCM+. The exact position of the power-take-off system is shown in figure 5.1. The spring damper coupling connects the two pontoons with an elastic force, which is given by Hooke's law, and a damping force. The total force on the end point located on the smaller pontoon is given by equation 5.5 and the other one by equation 5.6. [57]

$$F_{left} = k_e(x_{Spring} - x_0) + k_d v_{Spring} \tag{5.5}$$

$$F_{right} = -F_{left} \tag{5.6}$$

The force and the velocity of this push-rod were measured during the experiments at the Danish Hydraulic Institute. The data of one particular experiment was chosen and provided by Crestwing. The characteristics of the spring-damper coupling are derived from this data and are listed in table 5.3.

Table 5.3 – PTO Characteristics

Characteristic	Value
Relaxation Length x_0	0.686 m
Elastic Coefficient k_e	3035.28 kg/s^2
Damping Coefficient k_d	2082.2 kg/s

In this thesis, different types of power-take-off systems are investigated. All systems are based on the characteristics of the spring-damper coupling in table 5.3. They differ in the intensity of the brake effect depending on the direction of the rotation which in turn is determined by the linear motion of the push rod. When the two pontoons are approaching each other as in figure 5.4, the movement is referred to as the push. Hereby, the spring damper velocity is negative or zero. The pull movement is characterized by a positive spring damper velocity. In this case, the two barges are moving away from each other as in figure 5.5.

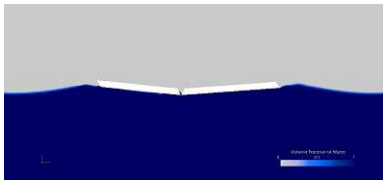

Figure 5.4 – Wave energy converter during the push motion ($v_{Spring} \leq 0\,\mathrm{m/s}$)

Figure 5.5 – Wave energy converter during the pull motion ($v_{Spring} > 0\,\mathrm{m/s}$)

Since the intensity of the brake effect can be attributed to the force in the push rod, the different power-take-off systems are simulated by adjusting the force on the endpoint of the spring damper coupling 5.5. To do so, the elastic coefficient k_e and the damping coefficient k_d in table 5.3 are modified by a user field function. The user field function differentiates between the push and pull motion with the aid of an if condition, which allows to apply the force on the spring damper independently for push and pull. Subsequently, the intensity of the force is varied according to table 5.4.

Table 5.4 – Percentage of the force on the spring damper during push and pull

	PTO 1	PTO 2	PTO 3	PTO 4	PTO 5
Push	100 %	80 %	50 %	100 %	80 %
Pull	100 %	80 %	50 %	0 %	20 %

The first power-take-off system is referred to as two-way braking. The brake is fully activated during the push and pull motion. This leads to a constant maximal resistance of the power-take-off system resulting in a constant force on the spring damper.
The second and third setups work as a two-way braking system since energy is extracted during the pull and push motion. The resistance and therefore the force in the spring damper is constant, but it is varied in its intensity.
The fourth setup is characterized by a maximal resistance of the power-take-off system during the push motion and a minimal resistance of the power-take-off system during the pull motion. This causes a force acting on the spring damper only during the push motion, but not during the pull motion. Subsequently, energy is only extracted during the push motion. This system is called one-way braking and is used by Crestwing, as experiments have shown a significantly improved power conversion. This can be attributed to the improved freedom of movement of the device, which allows the device to travel the maximal distance from the wave crest to the wave trough. [14]

The remaining power-take-off system extracts energy in both ways, but the resistance of the power-take-off system and therefore the force in the damping system differs between the push and the pull motion.

5.4 Computational domain

The computational domain is a rectangular box equal to the Danish Hydraulic Institute deepwater basin. The modelled water depth is 3 m. The length of the computational domain is 30 m and the width is 20 m. It is shown in figure 5.6.

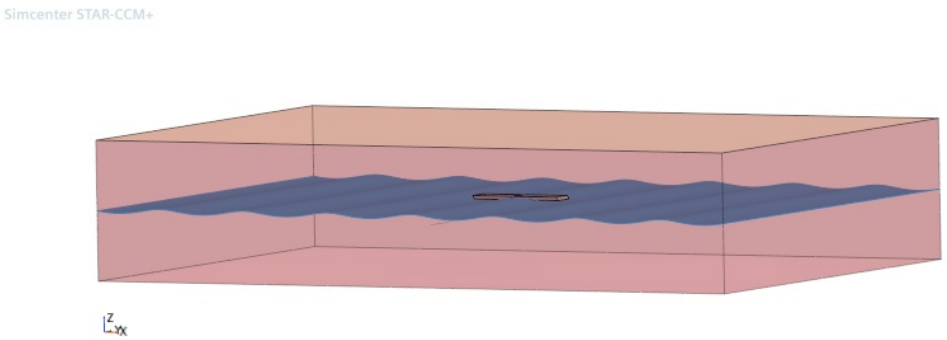

Figure 5.6 – Computational domain with the Crestwing wave energy converter

The boundaries of the domain are defined as follows: The top of the domain is set to a pressure outlet, which allows the airflow to evolve freely. Velocity inlets are applied on all vertical sides which allows simulating motions of the wave energy converter. The bottom of the domain is a velocity inlet, which implies that the bottom of the domain does not influence the water surface. This is one of the characteristics of deep water waves and it is fulfilled since the ratio of the water depth h and the wavelength λ is greater than 1/2 in all conducted simulations.

The wave energy converter is treated as a rigid body. Thus, a no-slip condition is applied on the surface of the device. Since the overset mesh approach is used, an overset boundary at the surface of the overset region is defined.

5.5 Governing equations

The mathematical model used by StarCCM+ is derived from the fundamental equations 3.2 and 3.4. [57] These equations are modified to calculate turbulent flows. [44] A turbulent flow is characterized by the fact that it is unsteady, irregular, random, and chaotic. Thus, the properties vary significantly and irregularly in space and time. [46] Therefore, all properties of a turbulent flow can be described as the sum of a mean and a fluctuating part, $q = \bar{q} + q'$. Assuming an incompressible, instationary, Newtonian, three-dimensional fluid flow and forming the time average of the continuity equation 3.3 and the Navier-Stokes equations 3.6 lead to the Unsteady Reynolds Navier-Stokes (URANS) equations. [64] These form the governing equations in this simulation.

$$\nabla \cdot \overline{\mathbf{v}} = 0 \tag{5.7}$$

$$\rho \frac{\partial \overline{\mathbf{v}}}{\partial t} + \rho(\overline{\mathbf{v}} \cdot \nabla)\overline{\mathbf{v}} = -\nabla \overline{p} + \nabla \cdot \overline{\mathbf{T}} + \nabla \cdot \mathbf{T_t} + \rho \overline{\mathbf{g}} \tag{5.8}$$

The force due to gravity $\rho\overline{\mathbf{g}}$ is added to the Navier Stokes equation using the gravity model of StarCCM+.

$\overline{\mathbf{T}}$ is the averaged viscous stress tensor for an incompressible Newtonian fluid which results from Stokes' law 3.5.

$$\bar{\mathbf{T}} = \mu(\nabla \overline{\mathbf{v}} + (\nabla \overline{\mathbf{v}})^T) \tag{5.9}$$

The additional term $\mathbf{T_t} = -\rho\overline{\mathbf{v}' \otimes \mathbf{v}'}$ in the URANS equations is referred to as the Reynolds stress tensor and describes the effect of the velocity fluctuations. [48] The Reynolds stress tensor adds six additional unknown quantities to the system of equations which consists of only four equations. [64] To close the system of equations, the Reynolds stress tensor is modelled using a turbulence model, more specifically the linear eddy viscosity model. [57] This turbulent model is based on the Boussinesq approximation, which equates the transport mechanism of the turbulent velocity fluctuation with the mechanism applied to the transport of molecules. [17] Thus, the Reynolds stress tensor $\mathbf{T_t}$ follows the same constitutive law as the viscous stress tensor 5.9. [64]

$$\mathbf{T_t} = \mu_t(\nabla\overline{\mathbf{v}} + (\nabla\overline{\mathbf{v}})^T) - \frac{2}{3}\rho k_t \mathbf{I} \tag{5.10}$$

Hereby, μ_t is the turbulent viscosity, k_t is the turbulent kinetic energy, and $\mathbf{I}$ is the identity tensor.

In this simulation, the $k-\epsilon$ model is used to obtain the unknown parameters in equation 5.10. The $k-\epsilon$ model is a two-equation model, providing transport equations for the turbulent kinetic energy k_t and the turbulent dissipation rate ϵ. Combined with the URANS equations, a closed system of equations is obtained. The turbulent viscosity can be derived with the aid of these properties and is modelled by equation 5.11. [46] C_μ is the model constant.

$$\mu_t = \rho C_\mu \frac{k_t^2}{\epsilon} \tag{5.11}$$

The transport equation for the turbulent kinetic energy $k_t = \frac{1}{2}\mathrm{tr}(\overline{\mathbf{v'}\mathbf{v'}^T})$ is derived from the Navier Stokes equation for an incompressible fluid 3.6. This equation is first multiplied by the velocity fluctuation $\mathbf{v'}$ and then time-averaged. Thus a differential equation for the Reynolds-stress tensor is obtained which is referred to as the Reynolds stress equation 5.12. [64]

$$\begin{aligned}\frac{\partial \mathbf{T_t}}{\partial t} + (\overline{\mathbf{v}}\cdot\nabla)\mathbf{T_t} = &-\mathbf{T_t}\cdot(\nabla\overline{\mathbf{v}} + \nabla(\overline{\mathbf{v}})^T) + 2\mu\overline{\nabla\mathbf{v}'\cdot(\nabla\mathbf{v}')^T} \\ &- \overline{p'\left(\nabla\mathbf{v}' + (\nabla\mathbf{v}')^T\right)} + \nabla\cdot\left[\mu\nabla\mathbf{T_t} + \rho\overline{\mathbf{v}'\otimes\mathbf{v}'\otimes\mathbf{v}'} + \overline{p'\mathbf{v}'\otimes(\mathrm{diag}(\mathbf{v}'))}\right]\end{aligned} \tag{5.12}$$

Taking the trace of the Reynolds stress equation yields the transport equation for the turbulent kinetic energy k_t 5.13 for an incompressible fluid. [44]

$$\rho\frac{\partial k_t}{\partial t} + \rho\overline{\mathbf{v}}\cdot\nabla k_t = \mathbf{T_t}\colon\nabla\overline{\mathbf{v}} - \rho\epsilon + \nabla\cdot\left[\left(\mu + \frac{\mu_T}{\sigma_k}\right)\nabla k_t\right] \tag{5.13}$$

The transport equation for the turbulent dissipation $\epsilon = \nu\,\mathrm{tr}\overline{(\nabla\mathbf{v}')\cdot(\nabla\mathbf{v}')^T}$ is obtained by applying $2\nu(\nabla\mathbf{v}')^T\cdot\nabla$ to the Navier-Stokes equation for an incompressible fluid 3.6. Subsequently, this product is time-averaged. This procedure leads to the exact transport equation for ϵ, which contains double and triple correlations of fluctuating velocity, pressure, and velocity gradients. These correlations are unknown and thus

must be simplified with suitable models. This results in the modelled ϵ equation 5.14. [64]

$$\rho\frac{\partial\epsilon}{\partial t}+\rho\overline{\mathbf{v}}\cdot\nabla\epsilon=C_{\epsilon1}\frac{\epsilon}{k_t}\mathbf{T_t}:\nabla\overline{\mathbf{v}}-\rho C_{\epsilon2}\frac{\epsilon^2}{k_t}+\nabla\cdot\left[\left(\mu+\frac{\mu_T}{\sigma_\epsilon}\right)\nabla\epsilon\right] \tag{5.14}$$
$$C_{\epsilon1}=1.44, C_{\epsilon2}=1.92, C_\mu=0.09, \sigma_k=1.0, \sigma_\epsilon=1.3$$

Subsequently, StarCCM+ discretizes this system of equations using finite-volume methods. Thereby, the governing equations are integrated over a control volume and Gauss's divergence theorem is applied. This yields the governing equations in integral form. [44] The generic form of these transport equations is given by 5.15, whereby Γ is the face diffusivity and S_ϕ is the source term at the cell center. [57]

$$\frac{d}{dt}\int_V\rho\phi dV+\int_S\rho\mathbf{v}\phi\cdot d\mathbf{a}=\int_S\Gamma\nabla\phi d\mathbf{a}+\int_V S_\phi dV \tag{5.15}$$

In this simulation, the governing equations in the integral form are solved iteratively by the segregated flow solver provided by StarCCM+. Thus, the diffusive term is discretized using a second order scheme and the convective term is discretized by the second order upwind scheme, which is chosen due to its robustness and accuracy. Further, the pressure-velocity coupling algorithm, called SIMPLE, is applied to obtain the discretization of the pressure gradient. Thereby, a pressure-correction equation is derived from the continuity and Navier-Stokes equations, which corrects the pressure to find a velocity field that fulfils the continuity equation. The pressure is finally yielded from this pressure-correction equation. [57]

Additionally, the Volume Of Fluid (VOF) multiphase model provided by StarCCM+ is applied to resolve the surface of the water. Thus, the phase volume fraction $\alpha_i=\frac{V_i}{V}$ is introduced, which describes the distribution of phases and the position of the interface. [57] α_i follows the phase mass conservation equation 5.16. [38]

$$\frac{\partial\alpha_i}{\partial t}+\nabla\cdot(\alpha_i\mathbf{v})=0 \tag{5.16}$$

Since the two Eulerian fluids, air ($\rho_A=1.184\,15\,\mathrm{kg/m^3}, \mu_A=1.855\,08\times10^{-5}\,\mathrm{Pas}$) and water ($\rho_W=997.561\,\mathrm{kg/m^3}, \mu_W=8.8871\times10^{-4}\,\mathrm{Pas}$), are immiscible, they are separated by a sharp interface. This results in large spatial variations of phase volume

fractions, which can not be accurately resolved by the second-order upwind scheme. Thus, High-Resolution Interface Capturing (HRIC) is applied additionally by the VOF multiphase model, to model the convective transport of the fluid components. [57]
The time derivation is discretized using the second-order implicit backward differentiation scheme, which is selected due to its high accuracy and reduced computing time. A physical time step of 0.001 s, an under-relaxation factor of 0.8, and eight inner iterations are chosen. This selection of parameters can be assumed to be sufficient for the given problem. Additionally, adaptive time stepping is implemented using the free surface Courant-Friedrichs-Lewy (CFL) Condition. Hereby, the chosen physical time step is adjusted based on the CFL number, which is weighted by the rate of change of volume fraction. The CFL number indicates how many cells the fluid moves per time step. According to Siemens, the CFL number must not be greater than 0.5 to ensure convergence, stability, and accuracy. [57] In this simulation, the maximum limit of the CFL number is set to 0.2 since the suggested maximum limit of 0.5 leads to instabilities during the simulation which were observed during the first test runs.

5.6 Waves

The Volume Of Fluid (VOF) multiphase model provided by StarCCM+ additionally contains the VOF Waves model, which is used in this simulation to model surface gravity waves.
StarCCM+ models, among others, first order waves with the first order approximation and fifth order waves with the fifth order approximation to the Stokes theory following the approach of [21]. Thereby, the perturbation parameter is defined as a product of the wave number and the wave amplitude $\varepsilon = \frac{kH}{2}$. [21] A steadily propagating periodic wave is assumed, whereby the wave train can be specified by the water depth h, the wavelength λ, and the wave height H. [57]
This results in a regular periodic sinusoidal wave profile given by equation 3.37 and equation 3.38 for the first-order Stokes wave theory. [57]
The solution of equation 5.17 and equation 5.19 for the fifth order Stokes wave theory can be derived as the water depth h, the wavelength λ, and the wave height H are known. Thereby, the wave number k and the perturbation parameter ε can be calculated. The

values of the coefficients can be withdrawn from the reference [21].

$$\phi(x,z) \approx -\overline{u}x + C_0 \left(\frac{g}{k^3}\right)^{1/2} \sum_{i=1}^{5} \varepsilon^i \sum_{j=1}^{i} A_{ij} \cosh(jkz) \sin(jkx) + O(\varepsilon^6) \tag{5.17}$$

$$\overline{u} \left(\frac{k}{g}\right)^{1/2} = C_0 + \varepsilon^2 C_2 + \varepsilon^4 C_4 + O(\varepsilon^6) \tag{5.18}$$

$$\begin{aligned} k\eta(x) = {} & kh + \varepsilon \cos(kx) + \varepsilon^2 B_{22} \cos(2kx) + \varepsilon^3 B_{31}(\cos(kx) - \cos(3kx)) \\ & + \varepsilon^4 (B_{42} \cos(2kx) + B_{44} \cos(4kx)) \\ & + \varepsilon^5 (-(B_{53} + B_{55}) \cos(kx) + B_{53} \cos(3kx) + B_{55} \cos(5kx)) + O(\varepsilon^6) \end{aligned} \tag{5.19}$$

In the case of unsteady fluid velocities, it is essential to know the wave speed c. It can be obtained by measurements or by Stokes's first definition of wave speed, which is described by $\overline{u}$ in equation 5.18. [21] Thereby, the wave speed is predicted relative to a frame in which the current is assumed to be zero. [67] Applying Stokes's first definition of wave speed to a physical frame, for example at the seabed, leads to a Doppler-shifted period due to the dependence of the wave speed on physical quantities such as the current or the mass flux. [21]

In most cases the wave period T rather than the wavelength λ and the mean uniform current $c_E = c - \overline{u}$ rather than the wave speed $c = \frac{\lambda}{T} = \frac{2\pi}{kT}$ are known. Thereby, the wave number k is unknown. The advantage of the approach made in [21] is that the wave number k can be calculated with the aid of one non-linear equation given by 5.20 using an iterative method. The most common used first approximation of k is the linear-deep water result for small Eulerian time mean fluid velocity $c_E = c - \overline{u}$, which is $k \approx \frac{4\pi^2}{T^2 g}(1 - \frac{4\pi c_E}{gT})$. [21]

$$\left(\frac{k}{g}\right)^{1/2} c_E - \frac{2\pi}{T(gk)^{1/2}} + C_0(kh) + \left(\frac{kH}{2}\right)^2 C_2(kh) + \left(\frac{kH}{2}\right)^4 C_4(kh) = 0 \tag{5.20}$$

Waves generated with the fifth order wave theory are claimed to be more realistic to ocean waves. However, this theory is only valid as long as the Ursell number $U_R = \frac{H\lambda^2}{h^3}$ is less than 30. [57] This condition applies to all conducted simulations. Therefore, the simulations are mainly performed with the fifth-order wave theory. Some simulations are also carried out with the first-order wave theory to compare the solutions of both

approaches.

In this thesis, the wavelength and the wave height are adjusted to provide simulations of the wave energy converter in different wave conditions. Thereby, wind and current are neglected and the wave heading is kept at 0° assuming head sea. The waves are propagating in x-direction with a cosine function cos(Wave Heading) and in y-direction with a sine function sin(Wave Heading). Thus, the boundary conditions in front and at the backside imply a wave tangential to the propagating x-direction that suits the propagating wave coming from the inlet boundary in front of the device. The boundary condition after the device applies the same cosine function in the positive propagating x-direction as the one in front of the device. Thus, it is assured that no eddies evolve due to the inlet boundaries and the waves are modelled properly.

Further, the wave settings together with the dimension of the computational domain assure that the waves are well developed when reaching the wave energy converter.

5.7 Mesh

The mesh used in this simulation consists of hexahedrons in an unstructured grid. It is created by the Trimmed Cell Mesher. This volume mesher is chosen because, among other advantageous features, it allows alignment with a user-specified coordinate system and refinement based on surface mesh size. First, the Trimmed Cell Mesher creates a template mesh consisting of hexahedral cells with a certain target size. The core mesh is trimmed from the template mesh using the geometry described in chapter 5.1 and 5.4. To improve and optimize the quality of the surface of the given geometry, the surface is retriangulated by the Surface Remesher yielding a high-quality triangle surface mesh of the given geometry. [57]

The mesh is refined in the important zones. Following the advice of Siemens [57], all refinements in this simulation are set as multiples of two from the target surface size. As the cell size increases only by a multiple of two from the target surface size, other refinement rates lead to an inappropriate mesh with unwanted inhomogenities.

The mesh of the computational domain in figure 5.7 is refined at the free surface to ensure an accurate resolution of the free surface. The thickness of the refinement is three times the wave height and the volumetric control is applied symmetrically

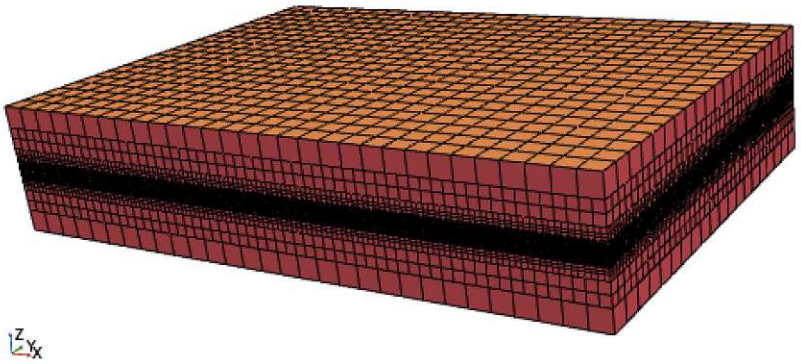

Figure 5.7 – Mesh of the computational domain

around the still water level. Further, the mesh is aligned with the wave direction to guarantee more accuracy. The mesh has 68 cells per wavelength and 9 cells per wave height in the refinement zone. This is slightly fewer cells than what is recommended by Siemens [57]. Nevertheless, these settings are used by [38] where a convergence study is conducted. Comparing these settings to the recommended settings by Siemens, no significant deviation in the results can be observed. Thus, it was concluded that these settings are a good compromise between the spatial discretization error and computational cost. However, shorter waves lead to an increasing number of cells and increased computational costs.

To capture the motion of the wave energy converter properly, the overset mesh approach is chosen. It discretizes a computational domain with different overlapping meshes by coupling the regions implicitly. The coupling results from a hole-cutting process, where cells in the background mesh become inactive when the solution is fully obtained by cells of the overset domain. This coupling leads to an exchange of data between acceptor and donor cells of each region. [57]

This simulation incorporates three regions, the background region and two overset regions. The background region captures the whole computational domain and is based on the mesh in figure 5.7. Further, an overset region for each part of the wave energy converter is applied. As recommended by Siemens [57], the size of the overset regions is determined such that there are at least five cells between the surface of the wave energy converter and the overset boundary. Thus, a proper data exchange between the background and the overset domain is ensured. To optimize the coupling of the two domains and ensure an accurate interpolation at the overset interface, the cell size

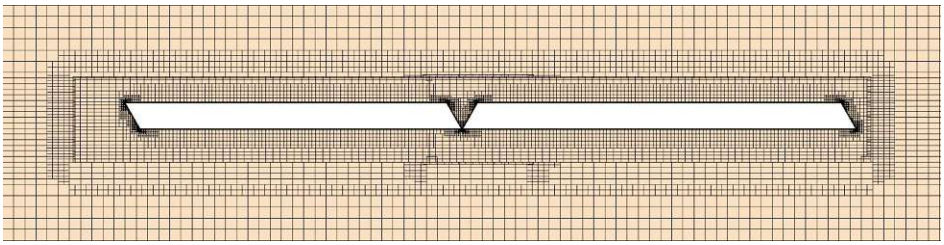

Figure 5.8 – Detail of the refined mesh around the wave energy converter

of the meshes should be similar. Thus, the background mesh shown in figure 5.7 is further refined in the overset overlapping zone such that the cell size of the refinement is approximated to the cell size of the overset meshes. Since the two overset meshes not only overlap with the background mesh but also with each other, the cell size of both overset meshes is set equally. Moreover, the cell size of the overset meshes must be slightly smaller than the one of the background mesh and it must correspond to a fifth of the implemented wavelength. This applies to all wavelengths shorter than the length of the device. For longer wavelengths, the cell size must not exceed a fifth of the length of the wave energy converter. Otherwise, instabilities at the edge of the overlapping region of the overset meshes and the background mesh occur. Additionally, the Adaptive Mesh Refinement (AMR) technique is used to match the cell size of the background and overset domain properly. [57] The mesh used in this simulation is shown in figure 5.8.

The surface of the wave energy converter is additionally resolved using three Prism Layers. The Prism Layer Mesher allows an accurate solution of the viscous sublayer by estimating the wall shear stress within the wall function approximation. To guarantee the high quality of the Prism Layer Mesh, the wall y+-value on the surface of the wave energy converter is mostly kept under 1. Further, the mesh of the wave energy converter in figure 5.9 is modified using surface control and curve control to refine the mesh at critical areas such as the edges of the wave energy converter.

Figure 5.9 – Mesh of the wave energy converter

5.8 Post processing

The aim of this thesis is to determine the efficiency of the wave energy converter. Thereby, the process of wave energy conversion has to be taken into account. The Crestwing wave energy converter transforms wave energy into mechanical energy in the first stage. Then, the absorbed energy is converted into useful mechanical energy using the power take-off system. Finally, a third conversion from this mechanical energy into electricity is carried out by connecting the power-take-off system to the generators. [56] In this thesis, the first two stages are of high interest. The mean wave energy flux is determined by equation 3.56 and refers to the width of the wave. Since the wave energy flux incident on the wave energy converter is relevant in this case, the width of the wave corresponds to the width of the device $w = 1\,\mathrm{m}$. Thus, the wave power is yielded by multiplying the mean wave energy flux according to equation 3.56 by the width of the device w. Further, equation 5.21 is obtained assuming deep water.

$$P_{Waves} = w c_g \overline{E_{tot}} = w \frac{c}{2} \frac{\rho g H^2}{8} = w \frac{1}{2} \sqrt{\frac{g\lambda}{2\pi}} \frac{\rho g H^2}{8} \tag{5.21}$$

Therefore, the waves exert a force according to equation 3.61 on the device. To determine the power exerted on the device, a user field function in StarCCM+ is implemented. It defines the dot product of the velocity and the absolute pressure normal to the wetted surface. This user field function is then integrated over the surface of the device resulting in equation 5.22.

$$P_{OnDevice} = \int_S (p\mathbf{n}) \cdot \mathbf{v} dS \tag{5.22}$$

The power exerted on the device is then transformed into mechanical energy using the power-take-off system. In this simulation, the power take-off system is modelled by the spring-damper coupling which experiences the force according to equation 5.5. The power of the power take-off system in equation 5.23 is determined by multiplying this force with the velocity of the spring-damper coupling.

$$P_{PTO} = F_{left} v_{Spring} \tag{5.23}$$

Star CCM+ provides field functions for the force in the spring damper F_{Left}, the velocity

v, the absolute pressure p_{abs} and the normal vector **n**. There is no specific field function for the spring velocity v_{Spring} but only for the spring elongation x_{Spring} and the time step Δt. Thus, a user-defined field function is implemented to calculate the velocity of the spring damper. Thereby, the derivative of the spring elongation is defined using finite difference. The difference quotient is given by equation 5.24.

$$v_{Spring} = \frac{dx_{Spring}}{dt} \approx \frac{x_{n+1} - x_n}{\Delta t} = 2\frac{x_{n+1} - \frac{x_{n+1}+x_n}{2}}{\Delta t} = 2\frac{x_{n+1} - x_{mean}}{\Delta t} \tag{5.24}$$

The spring elongation x_n can not be retrieved by StarCCM+ directly. Thus, the difference quotient is rewritten using the average of the two most recent data points during the simulation. The average of data samples can be obtained using the field function monitor Field Mean. The data samples are collected using the sliding sample window which allows the two most recent data samples to be accessed during the simulation.

Equations 5.21, 5.22 and 5.23 are integrated over the operating time to obtain the total amount of wave energy, the total amount of absorbed energy, and the total amount of converted energy by the power take-off system. The operating time is 8 s, whereby the first second of the simulations are not considered to avoid any inconsistencies at the beginning. The time period of 7 s is determined based on the values of the simulations which results in slightly different time intervals.

This data allows determining the loss of energy during the different stages of energy conversion. The amount of wave energy transferred to the device is determined by equation 5.22 and the amount of useful mechanical energy converted from the absorbed energy in the power-take-off system is given by equation 5.23. Thus, the overall efficiency is defined as the ratio of the energy in the power-take-off system and the total amount of wave energy.

$$\eta_{WEC} = \frac{E_{PTO}}{E_{Waves}} \tag{5.25}$$

6

Results

In this section, the results of the simulations will be discussed. Of great interest is the efficiency of the device as well as the behaviour of the waves. Therefore, the generated waves in the empty wave tank will be validated with the reference [38]. Further, a mesh and time step verification will be carried out for the overall simulation. Different applications of the power-take-off system are analysed and compared for the wave condition which achieved one of the highest efficiency in conducted experiments. The efficiency of the wave energy converter in different wave conditions is studied. These results are compared to experimental data provided by Crestwing and the reference [8]. Furthermore, flow analysis of the wave energy converter in the waves for different power-take-off systems as well as for different wave conditions will be carried out.

6.1 Experimental data

The experimental data provided in this chapter is used to compare and validate the results of the CFD simulations. Several wave tank tests with the Crestwing wave energy converter are carried out in the 3D offshore basin at the Danish Hydraulic Institute Offshore Test Facility. The model of the Crestwing wave energy converter is provided by Danish Yacht and fabricated at a scale of 1:20 using a composite material similar to the prototype material and is shown in figure 6.1. It is equipped with two different types of power-take-off systems representing the first model and the fourth model in table 5.4. [8] Further information about the setup and the experiments can be found in [8]. The experiments aim to understand the hydrodynamic behaviour of the Crestwing wave energy converter, the performance of the power-take-off system, and the effect of the mooring system. [8] This work focuses especially on the performance of different

applications of power-take-off systems as well as the behaviour of the wave energy converter in different wave conditions.

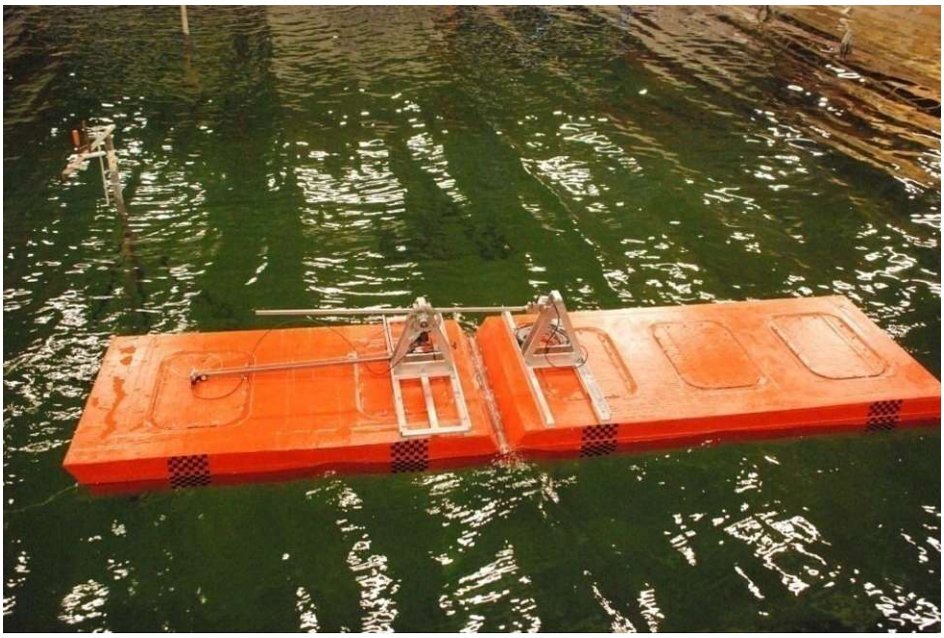

Figure 6.1 – Model of the Crestwing wave energy converter used in experiments at the Danish Hydraulic Institute [8]

The data shown in table 6.1 is provided by Crestwing and refers to experiments conducted with the fourth power-take-off system of table 5.4 in various wave conditions. The mean energy flux of the waves in table 6.1 is calculated according to equation 5.21. The power in the power-take-off system in table 6.1 is measured every 0.025 s. Both values are integrated over a time period of 7 s, whereby the time period is chosen so that there is hardly a phase difference between the wave in the experiment and the simulated wave. The efficiency is derived according to equation 5.25. This allows a feasible comparison between the experiments and the simulations.

The Crestwing wave energy converter attains quite high efficiencies for some wave conditions. Especially the wave conditions where the wavelength λ approximately equals the length of the device $L_{device} = 4\,\mathrm{m}$ tend to have high efficiencies. However, the efficiency decreases with smaller wavelengths as shown in table 6.1. The maximum efficiency of 66 % is obtained in the experiments for a wavelength of $\lambda = 3.7\,\mathrm{m}$ and a wave height of $H = 0.125\,\mathrm{m}$ whereas experiments with a wavelength of $\lambda = 2.2\,\mathrm{m}$ and a wave height of $H = 0.05\,\mathrm{m}$ result in the minimum efficiency of 6 %. Overall, the efficiency within these wave conditions is still comparable with other renewable energy

Table 6.1 – Experimental data provided by Crestwing

wave steepness $[s] = -$	wave height $[H] = \mathrm{m}$	wave period $[T] = \mathrm{s}$	wave length $[\lambda] = \mathrm{m}$	theoretical wave energy $[E_{Waves}] = \mathrm{J}$	energy PTO $[E_{PTO}] = \mathrm{J}$	efficiency $[\eta_{WEC}] = \%$
0.1316	0.250	1.10	1.9	462.01	39.21	9
0.1136	0.250	1.20	2.2	497.14	64.00	13
0.0962	0.250	1.30	2.6	540.45	169.91	31
0.0446	0.250	1.90	5.6	793.17	281.63	36
0.0645	0.200	1.40	3.1	377.69	200.76	53
0.0500	0.200	1.60	4.0	429.02	233.06	54
0.0392	0.200	1.80	5.1	484.44	255.21	53
0.0789	0.150	1.10	1.9	166.32	23.25	14
0.0682	0.150	1.20	2.2	178.97	32.42	18
0.0577	0.150	1.30	2.6	194.56	81.46	42
0.0338	0.125	1.53	3.7	161.18	107.11	66
0.0263	0.050	1.10	1.9	18.48	3.49	19
0.0227	0.050	1.20	2.2	19.89	1.29	6
0.0192	0.050	1.30	2.6	21.62	6.58	30
0.0161	0.050	1.40	3.1	23.61	7.08	30

sources as solar energy reaches efficiencies of up to 35 %. [39] In comparison, wind energy achieves up to 40 % efficiency. [4]

6.2 Empty wave tank

At first, a verification study of the wave generation in an empty CFD wave tank is conducted. The validation of the waves in the empty wave tank is carried out using the mesh of the computational domain shown in figure 5.7 and the time step settings described in chapter 5. This setup of the simulation follows [38], where a mesh and time step verification study is conducted for fifth-order Stokes waves.

The mesh verification study in [38] shows that using 68 cells per wavelength and 9 cells per wave height in the wave refinement zone is sufficient to resolve the water surface. Further refinement does not particularly improve the accuracy of the results while increasing computational cost severely, whereas a coarser mesh would diminish the accuracy of the results considerably but decrease the computational effort. Thus, these mesh refinement settings are chosen for the conducted simulation as it seems to be a sufficient compromise between the spatial discretization error and computational cost.

The time step verification study for the empty wave tank in [38] concludes that 750 time

steps per incident wave period are considered the best compromise between temporal discretization errors and computational cost. A bigger time step leads to a remarkable loss in accuracy, whereas using a smaller time step increases the computational cost while not improving the accuracy of the results. However, in the conducted simulation 1500 time steps per incident wave period are chosen which corresponds to the average physical time step of 0.001 s. Although this increases the computational effort for the simulation of the empty wave tank, the chosen time step provides the necessary accuracy and resolution for the further setup of the simulation.

The incident wave amplitude may decrease when the waves progress in an empty CFD wave tank. This can be attributed to numerical diffusion caused by pseudo-physical effects. [38] Dissipative effects are added by even-order derivatives and dispersive effects are added by odd-order derivatives to the numerical solution. Thus, the numerical solution deviates from reality as neither dispersion nor dissipation occurs physically in the wave equation. [62]

The loss of the incident wave amplitude in an empty wave tank is used to validate the setup of the empty wave tank. In this study, simulations of the waves in the empty wave tank with four different wave conditions are conducted. The wavelength is chosen depending on the length of the device L_{device} and the wave height is adapted such as the wave steepness is kept constant at $s = 0.0316$. The waves are generated using first and fifth order Stokes theory, which are then compared to linear waves whose amplitude is defined by equation 3.1. Figures 6.2a - 6.2d show the wave elevation resulting from the three different wave theories. The blue line represents the theoretical linear waves, the green line shows the wave elevation of the simulated first-order Stokes waves and the red line illustrates the wave elevation of the simulated fifth-order Stokes waves.

In figures 6.2a - 6.2d, the fifth-order Stokes waves appear to be a better approximation to the linear wave theory than the first-order Stokes wave. First of all, a marginal phase shift of the simulated waves to the right can be observed, whereby the phase shift of the first-order Stokes waves is greater than the one of the fifth-order Stokes waves. However, the phase shift in general is most likely due to the mesh alignment to the waves. Secondly, the amplitudes of the fifth-order Stokes waves deviate less from the linear waves than the first-order Stokes waves. The amplitudes of the first and fifth order Stokes waves in figures 6.2a and 6.2b tend to decrease steadily when

propagating in the empty wave tank, whereas these in figures 6.2c and 6.2d decrease at first and increase again at the end of the empty wave tank. Thereby, the maximum loss of the incident wave amplitude is greater for first order Stokes waves and is allocated to the end of the empty wave tank in figures 6.2a and 6.2b and to the middle of the empty wave tank in figures 6.2c and 6.2d. This phenomenon can be attributed to the inlet boundary condition at the end of the empty wave tank, which influences the wave amplitude, especially in the case of figures 6.2c and 6.2d.

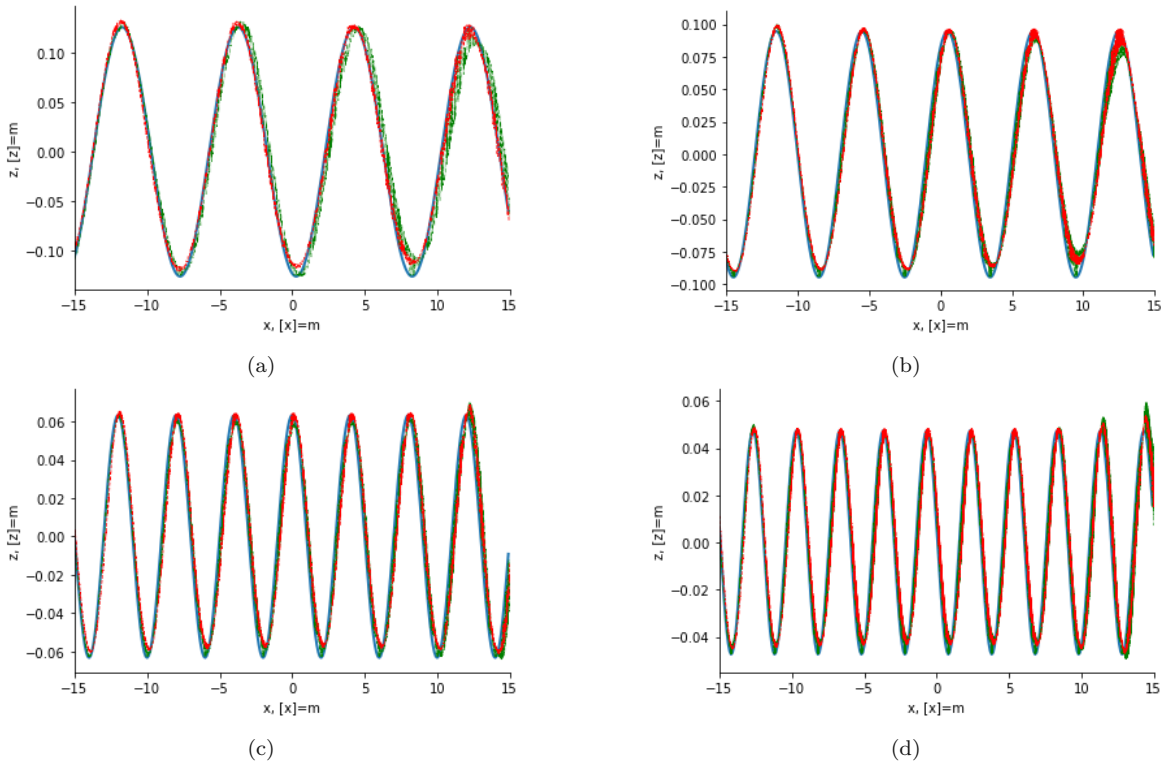

Figure 6.2 – Comparison of the wave elevation of theoretical linear waves (blue line), simulated first order Stokes waves (green line), and the simulated fifth order Stokes waves (red line) over the tank after $t = 8\,\mathrm{s}$. The wavelength, (a)$\lambda = 2L_{device}$, (b) $\lambda = 1.5L_{device}$, (c) $\lambda = 1L_{device}$ and (d) $\lambda = 0.75L_{device}$ depends on the length of the device and the wave heights are adapted, such that the wave steepness is kept constant

In the reference [38] the wave amplitude is measured at the position, where the center of gravity of the device is and is determined using the Fourier fitting procedure also used by the reference [25]. In this thesis, the deviation of the incident wave amplitude is determined in a simpler way. The wave elevation of the simulated first and fifth-order Stokes waves is determined at each x-coordinate, where a maximum of the linear wave is located. To identify the values of the wave elevation at these x-locations, the fourth order spline interpolation is performed using `scipy.interpolate.UnivariateSpline()`.

The smoothing factor specifying the number of knots is set to zero to interpolate through all data points. [11] This allows to determine the wave elevation at the exact x-location, where the maxima are identified. The average wave amplitude is calculated with the aid of these values and is compared to the incident wave amplitude. The deviation of the wave elevation from the incident wave amplitude is shown in table 6.2.

Table 6.2 – Loss of the incident wave amplitude

$\frac{\lambda}{L_{device}}$	1^{st} order Stokes waves	5^{th} order Stokes waves	reference
0.75	+0.3 %	-7.0 %	-7.2%
1.00	-7.0 %	-4.4 %	-3.2%
1.50	-7.3 %	-3.8 %	-1.9%
2.00	-4.6 %	-0.6 %	-1.3%

In general, a decrease of the incident wave amplitude can be noted in table 6.2. The first-order Stokes waves with the shortest wavelength are an exception because the incident wave amplitude increases. This is due to the substantial increase in wave height at the end of the empty wave tank in figure 6.2d. Since the loss of the incident wave amplitude is determined by the average of the maxima of the wave elevation, this increase contributes significantly to the calculation of the loss of the incident wave amplitude and leads to an overall increase of the incident wave amplitude. Nevertheless, a loss of the incident wave amplitude in the middle of the empty wave tank can be seen in figure 6.2d. Such an increase in wave height at the end of the empty wave tank is also observed for first-order waves with a wavelength of $\lambda = 1L_{device}$ in figure 6.2c. However, it is not as high as for waves with the shortest wavelength of $\lambda = 0.75L_{device}$ in figure 6.2d, which results in an overall loss of the incident wave amplitude. This also applies for fifth order Stokes waves for the two shortest wavelengths of $\lambda = 1L_{device}$ in figure 6.2c and $\lambda = 0.75L_{device}$ in figure 6.2d. The increase in wave height at the end of the empty wave tank for fifth-order Stokes waves is minimal so that the average of the wave amplitude is not influenced by these values.

Table 6.2 indicates that the loss of the incident wave amplitude for fifth-order Stokes waves increases for shorter wavelengths. This tendency also occurs in the reference [38]. However, the loss of the incident wave amplitude for first-order waves increases at first but decreases again with a shorter wavelength. This can be attributed to the aforementioned increase in wave height at the end of the empty wave tank.

In addition to this tendency, a quantitative similarity is observed in table 6.2 when

comparing the values of the loss of the incident wave amplitude of fifth order Stokes waves with the reference [38]. Even though a direct comparison to the reference [38] is not entirely correct since another methodology is used for determining the loss of the incident wave amplitude, the similarity of the results indicates the accuracy and validity of the empty wave tank with the fifth-order Stokes waves. The values of the loss of the incident wave amplitude of first-order Stokes waves deviate significantly from the ones for fifth-order Stokes waves. This confirms the observation made in figure 6.2a - 6.2d, that the fifth order Stokes waves approximate the linear waves better than the first order Stokes waves.

All points considered, the empty wave tank with the fifth order Stokes waves serves as the starting point for further simulations. Thereby, the mesh and the time step described in chapter 5 are used because the resolution and accuracy are satisfactory. Nevertheless, a verification study of the mesh and the time step are carried out.

6.3 Mesh and time step verification

The verification study of the overall simulation is conducted for fifth order Stokes waves with a wavelength of $\lambda = 1L_{device} = 4\,\mathrm{m}$ and a wave height $H = 0.2\,\mathrm{m}$ at 0° heading. These wave conditions yield one of the highest efficiencies in experiments performed at the DHI deepwater basin and are of interest later in this thesis. The wave energy converter is equipped with the fourth power-take-off system of table 5.4 within the verification study as the one-way braking is the most complicated system to implement and will be further investigated in different wave conditions. Since the efficiency of the wave energy converter is investigated in this thesis, the verification study of the mesh and the time step focus on the energy exerted on the device and the energy of the power-take-off system.

The time step verification study is carried out by testing three different maximum time step sizes with the mesh settings described in chapter 5. This mesh is based on the settings of the empty wave tank, which is already verified in chapter 6.2. The results in table 6.3 show that there is no significant deviation between the results of the energy exerted on the device and the energy of the power-take-off system for all tested time steps.

Table 6.3 – Time step verification

max time step $[\Delta t_{max}] = \mathrm{s}$	mean time step $[\Delta t_{mean}] = \mathrm{s}$	elapse time $[t_{elapse}] = \mathrm{h}$	energy on device $[E_{OnDevice}] = \mathrm{J}$	energy PTO $[E_{PTO}] = \mathrm{J}$
0.0005	0.000337	≈ 76	191.59	188.42
0.0010	0.000360	≈ 66	188.92	187.04
0.0020	0.000351	≈ 74	189.92	185.16

However, the elapsed times of the conducted simulations vary noticeably and do not act as expected. Generally, the elapsed time and also the CPU time decrease with an increasing time step as the CPU time depends on the time step and the cell volume. This tendency can be observed when looking at the simulations with the two smallest maximal time steps in table 6.3 and figure 6.4. On the contrary, the elapsed time and the CPU time increase again when increasing the maximum time step from 0.001 to 0.002. This can be attributed to the use of the adaptive time stepping, which refers to the free surface CFL Condition and adjusts the implemented time steps of 0.005, 0.001, and 0.002 based on the weighted Convective Courant (CFL) number automatically. [57] The variation of the time step during the simulations is displayed in figure 6.3. Additionally, the mean time step is calculated and enlisted in table 6.3. Figure 6.3 illustrates that the implemented time steps of 0.0005 and 0.001 are used frequently whereas the time step of 0.002 is not applied at all. Consequently, the CFL Condition for the adaptive time stepping is fulfilled using the smaller time steps, but can not be met by the greatest time step. This results in a maximum time step of approximately 0.0014 for the simulation with an implemented time step of 0.002 which is only applied twice as a local peak. Due to this the mean time step of the simulation increases at first but decreases at a certain point with an increasing implemented time step which can be seen in table 6.3. The decreased mean time step for the simulation with the highest implemented time step causes an increase of the CPU time of this simulation. All points considered, the implemented time step of 0.001 is used in further simulations as it seems to be the most efficient while providing sufficient accuracy.

Since the mean time step of the three simulations conducted is similar, varying the CFL number further validates the simulation. In this thesis, no verification study of the CFL number is provided. However, it was observed during the first test runs that simulations with a CFL number of 0.1 are accompanied with extreme long elapse times, while providing similar results to the simulations with a CFL number of 0.2. Using a CFL

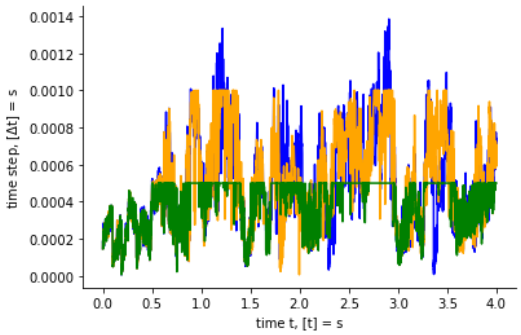

Figure 6.3 – Actual used time step for a maximum time step Δt_{max} of $\Delta t_{max} = 0.002\,\text{s}$ (blue), $\Delta t_{max} = 0.001\,\text{s}$ (orange) and $\Delta t_{max} = 0.0005\,\text{s}$ (green)

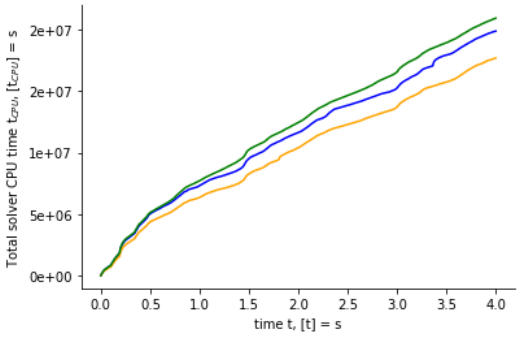

Figure 6.4 – Accumulated CPU time for all processes for the simulations with a maximal time step Δt_{max} of $\Delta t_{max} = 0.002\,\text{s}$ (blue), $\Delta t_{max} = 0.001\,\text{s}$ (orange) and $\Delta t_{max} = 0.0005\,\text{s}$ (green)

number of 0.2 decreases the elapse time significantly, which is why further simulations are conducted with a CFL number of 0.2.

The mesh verification study is conducted by changing the base size of the background mesh and the overset meshes. However, the wave refinement zone is implemented according to the settings used in chapter 6.2 as these are already verified by [38]. Otherwise, the simulations are based on the settings described in chapter 5 and use the maximal time step of $\Delta t_{max} = 0.001\,\text{s}$ that was found to be adequate within the time step verification study. Three different base sizes are tested, whereby the base size of the background and the overset meshes are changed in the same ratios.

The base size influences the size of all cells except the prism layer cells, whereby it also determines the number of cells. The smallest base size leads to the finest mesh consisting of the most cells, while the coarsest mesh with the least cells is achieved with the largest base size. Generally, finer meshes lead to more accurate results but also increase the simulation time. This can be observed in table 6.4, where the simulation time increases with an increasing number of cells. The energy exerted on the device differs considerably for the simulation with the coarsest mesh and the one with the medium mesh. On the contrary, the deviation of the energy exerted on the device is marginal between the medium mesh and the finest mesh. The energy in the power-take-off system deviates significantly for all three meshes and does not converge monotonously. As a result, the appropriate mesh is chosen depending on the energy exerted on the device and the simulation time. Considering the enormous simulation time with the finest mesh and the minor deviation of the energy exerted on the device compared to the simulation

with the medium base size, it was concluded that the medium base size provides the best compromise between accuracy and computational effort. Thus, the medium base size will be used in further simulations.

Table 6.4 – Mesh verification

base size background mesh $[\Delta x_{back}] = \text{m}$	base size overset mesh $[\Delta x_{overset}] = \text{m}$	cells	elapse time $[t_{elapse}] = \text{h}$	energy on device $[E_{OnDevice}] = \text{J}$	energy PTO $[E_{PTO}] = \text{J}$
3 m	0.6 m	9060971	≈ 124	189.52	179.76
4 m	0.8 m	6092254	≈ 66	188.92	187.04
8 m	1.6 m	4680185	≈ 53	184.19	182.05

Figure 6.5 shows the residuals for the simulation with a time step of $\Delta t_{max} = 0.001\,\text{s}$, a maximum CFL number of 0.2, and the mesh with $\Delta x_{back} = 4\,\text{m}$ and $\Delta x_{overset} = 0.8\,\text{m}$. The residuals converge perfectly. Hence, sufficiently accurate results are provided with these settings which are used in all following simulations.

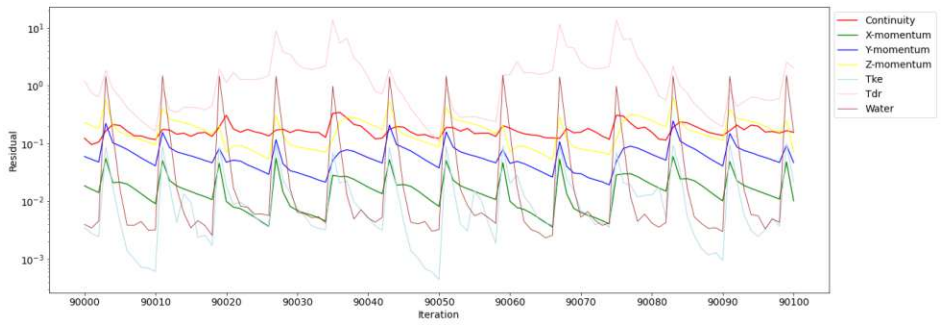

Figure 6.5 – Residuals of the simulation with the medium base size of the mesh and a time step of 0.001 s

6.4 CFD simulations of the Crestwing wave energy converter

In the following, the results of the CFD simulations are discussed. The simulations model the Crestwing wave energy converter in a wave tank with fifth order Stokes waves. The setup described in chapter 5 is used with the mesh and the time step that have been validated in chapter 6.3.

An excerpt of the simulation is shown in figure 6.6, where the motion sequence of the wave energy converter within one wave period is illustrated. Thereby, the wave energy converter is operating in fifth order Stokes waves having a wave height of $H = 0.2\,\mathrm{m}$ and a wavelength of $\lambda = 4\,\mathrm{m}$. First the wave energy converter travels over the wave crest, with the two barges moving away from each other performing the pull motion. When the barge travels from one wave crest to the next the push motion is executed. In the process, the two barges approach each other being the closest in the wave trough. Lastly, the barges approach the wave crest again with the push motion transitioning back to the pull motion.

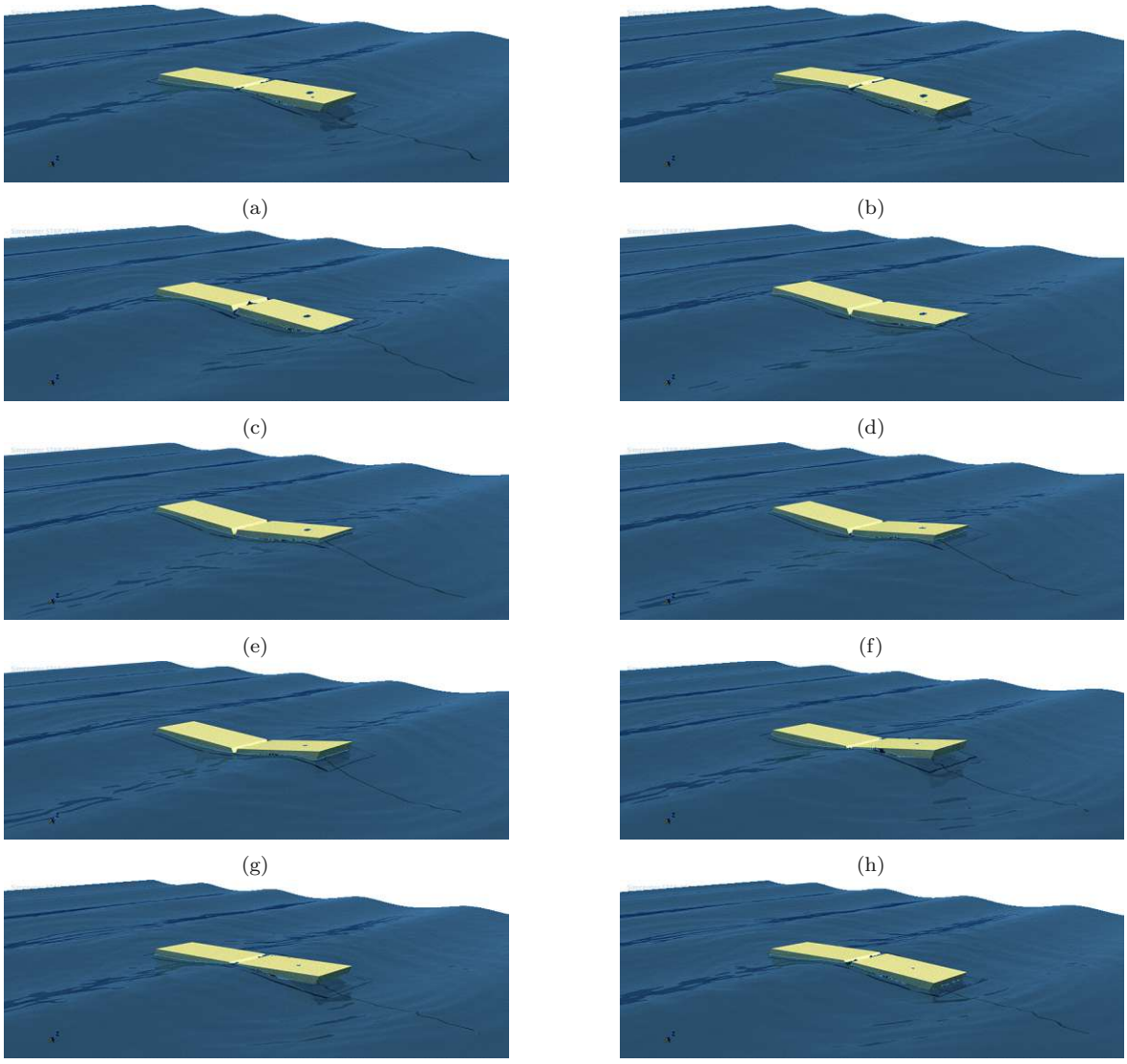

(a) (b) (c) (d) (e) (f) (g) (h) (i) (j)

Figure 6.6 – Crestwing wave energy converter operating in waves of a wave height of $H = 0.2\,\mathrm{m}$ and a wavelength of $\lambda = 4\,\mathrm{m}$ during one wave period

The induced velocity field of the waves in the whole domain is depicted in figure 6.7. The velocity field is in agreement with linear wave theory for deep water, as the vortices indicate the circular motion of the water particle. The water particle moves in the direction of the phase velocity beneath the wave crest and in the opposite direction beneath the wave trough. This is clearly visible in figure 6.8, where a more detailed profile of the fluid velocity around the wave energy converter is illustrated.
Figure 6.9 also shows a detailed profile of the velocity around the wave energy converter without the vector arrows. This enables to study the behaviour of the water surface around the device. When the wave energy converter dips into the water, the water surface is pushed down. The device is almost completely immersed, except from one area in the front half of the front pontoon. In this area, the pontoon is above the water surface, so that the water can not exert any pressure on the device. This can also be observed in figure 6.10, where the pressure distribution on the bottom of the device shows that the pressure in this area decreases. Moreover, a decrease of the pressure at the end of the aft pontoon is identified. This can be attributed to a decrease in wave elevation downstream the aft pontoon. A decrease in wave elevation indicates a loss in wave energy, whereby it can be concluded that energy from the waves is extracted by the device.

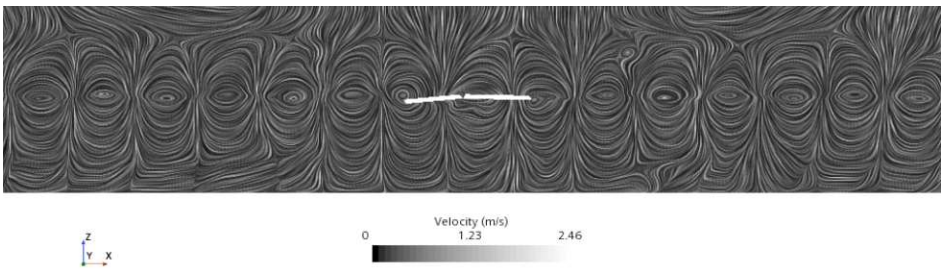

Figure 6.7 – Velocity in the wave tank for waves with a wave height of $H = 0.2\,\mathrm{m}$ and a wavelength of $\lambda = 4\,\mathrm{m}$ after $t = 8\,\mathrm{s}$

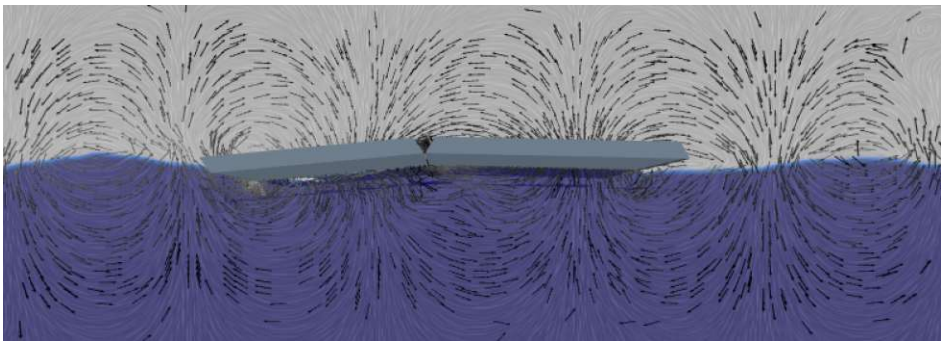

Figure 6.8 – Detail of the water particle motion in the wave tank around the wave energy converter operating in waves with a wave height of $H = 0.2\,\mathrm{m}$ and a wavelength of $\lambda = 4\,\mathrm{m}$ after $t = 8\,\mathrm{s}$

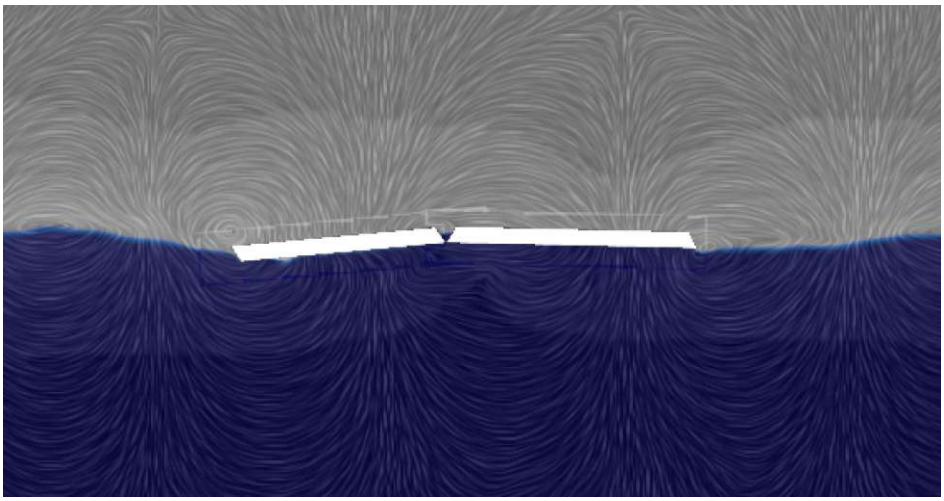

Figure 6.9 – Detail of the velocity in the wave tank around the wave energy converter operating in waves with a wave height of $H = 0.2\,\mathrm{m}$ and a wavelength of $\lambda = 4\,\mathrm{m}$ after $t = 8\,\mathrm{s}$

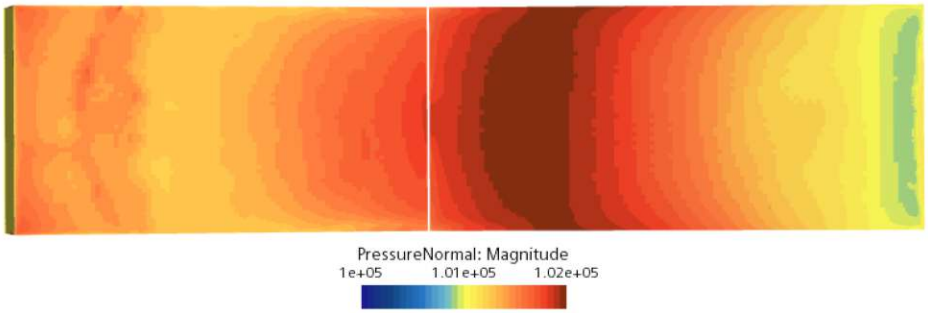

Figure 6.10 – Pressure on the bottom of the device operating in waves with a wave height of $H = 0.2\,\mathrm{m}$ and a wavelength of $\lambda = 4\,\mathrm{m}$ after $t = 8\,\mathrm{s}$

The induced velocity field of the waves in the whole domain as well as a more detailed illustration is shown in the appendix A.1.1 for different wave conditions and in appendix A.2.2 for different power-take-off systems.

6.5 Performance in different wave conditions

Hereafter, CFD simulations of the wave energy converter in different wave conditions are carried out to understand the behaviour of the wave energy converter. Due to the irregular nature of ocean waves, it is crucial to analyse the efficiency of the wave energy converter in different wave conditions. Therefore, the efficiency of the first wave energy conversion stage and the overall efficiency of the wave energy converter in different wave conditions is determined. Subsequently, the results of the simulations are compared to those of the experiments conducted at the Danish Hydraulic Institute. The set-up of the simulations described in chapter 5 is used. Different wave conditions of regular waves are simulated by adapting the wavelength λ and the wave height H. Hereby, the wave characteristics are chosen such as the simulations are comparable to conducted experiments. The wave energy converter is equipped with the fourth power-take-off system, as it is based on the same principle as the one used in experiments.

Table 6.5 summarizes the results of the simulations conducted with different wave conditions.

The theoretical mean wave energy flux is calculated according to equation 5.21 and is listed in table 6.5 as well as in table 6.1. The waves contain more energy the greater the wave height and the longer the wavelength, as the wave power P_{Waves} is proportional to the wave height H and the wavelength λ.

The wave energy converter captures the energy contained in the waves within the first wave energy conversion stage. The energy exerted on the wave energy converter follows equation 5.22 and is listed in table 6.5. It is noticeable that the efficiency of the first energy conversion stage increases with an increasing wavelength at constant wave height as long as the wavelength does not exceed the length of the wave energy converter $L_{device} = 4\,\mathrm{m}$. If the wavelength is greater than the length of the device, the efficiency of the first energy conversion stage decreases again. This is due to the fact that the wave energy converter can not align perfectly with waves having a small

Table 6.5 – Performance of the wave energy converter in different wave conditions

wave steepness $[s] = -$	wave height $[H] = \mathrm{m}$	wave period $[T] = \mathrm{s}$	wave length $[\lambda] = \mathrm{m}$	theoretical wave energy $[E_{Waves}] = \mathrm{J}$	energy on device $[E_{OnDevice}] = \mathrm{J}$	energy PTO $[E_{PTO}] = \mathrm{J}$	efficiency first stage $[\eta_{WEC,1}] = \%$	overall efficiency $[\eta_{WEC}] = \%$
0.1316	0.250	1.10	1.9	462.01	30.10	6.95	7	2
0.1136	0.250	1.20	2.2	497.14	154.42	132.34	31	27
0.0962	0.250	1.30	2.6	540.45	337.26	190.75	62	35
0.0446	0.250	1.90	5.6	793.17	383.65	360.47	48	45
0.0645	0.200	1.40	3.1	377.69	252.60	237.79	67	63
0.0500	0.200	1.60	4.0	429.02	369.23	327.47	86	76
0.0392	0.200	1.80	5.1	484.44	275.59	306.18	57	63
0.0789	0.150	1.10	1.9	166.32	9.65	19.71	6	12
0.0682	0.150	1.20	2.2	178.97	33.68	24.52	19	14
0.0577	0.150	1.30	2.6	194.56	78.81	62.15	41	32
0.0338	0.125	1.53	3.7	161.18	129.29	137.86	80	86
0.0263	0.0500	1.10	1.9	18.48	6.92	0.54	37	3
0.0227	0.0500	1.20	2.2	19.89	8.47	0.93	43	5
0.0192	0.0500	1.30	2.6	21.62	5.61	2.37	26	11
0.0161	0.0500	1.40	3.1	23.61	22.15	12.11	94	51

wavelengths. As a result, the wave energy converter floats on the wave crest and is not fully submerged, whereas only the pressure of the wave crest acts locally on the bottom of the device. The more the wavelength resembles the length of the device, the better the wave energy converter can follow the waves. Thus, the wave energy converter is fully submerged resulting in a high pressure transfer across the entire bottom of the device. For a wavelength longer than the length of the device, the pressure is distributed rather equally on the bottom of the device, but does not reach any maximal values. This is observed in figures 6.11 - 6.14, that show the pressure distribution on the bottom of the wave energy converter for different wavelengths and wave heights at $t = 8\,\mathrm{s}$. Since the energy exerted on the wave energy converter is determined by the pressure normal to the wetted surface, the first wave energy conversion stage is the most efficient, the more pressure is exerted on the device. This is the case for $\lambda \approx L_{device}$.

However, the efficiency behaviour of the first energy conversion stage for simulations conducted with a wave height of $H = 0.050\,\mathrm{m}$ acts differently. Generally, the efficiency of the first energy conversion stage also increases at first with an increasing wavelength. However, a decrease in the efficiency is observed at a wave length of $\lambda = 2.6\,\mathrm{m}$. In figures 6.11 - 6.15 it is generally observed that the pressure at a wavelength of $\lambda = 1.9\,\mathrm{m}$ is better distributed for higher wave heights, but still acts only locally on the bottom of the device at all wave heights, as the wave energy converter does not follow the waves properly and therefore floats on the wave crests and is not fully immersed. For the smallest wave height of $H = 0.05\,\mathrm{m}$, this is also observed for longer wavelengths, as is visualized in figure 6.15a - 6.15c. Thereby, the local impact of the pressure on the device decreases with an increasing wave length, but reaches higher values. Thus, the efficiency of the first energy conversion stage still increases at first. At a wavelength of $\lambda = 2.6\,\mathrm{m}$ the pressure acting on the device is already distributed more equally on the device, but does not reach as high values as the pressure exerted on the device by waves with a smaller wavelength. This results in a decreasing efficiency.

Increasing the wavelength to $\lambda = 3.1\,\mathrm{m}$ at a wave height of $H = 0.05\,\mathrm{m}$ leads to a significant increase in efficiency of the first energy conversion stage as an efficiency of 94 % is achieved. This is due to an increase of the pressure normal to the wetted surface resulting from a more equally distributed pressure and more frequently occurring maximum values of the pressure. This can be observed in figure 6.15d.

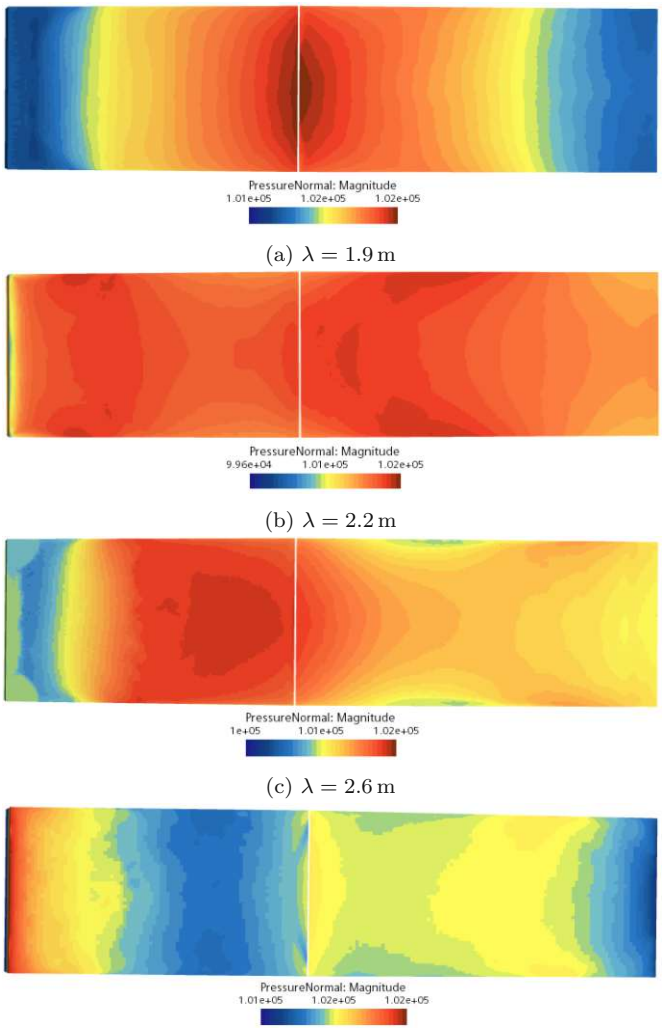

(a) $\lambda = 1.9\,\mathrm{m}$

(b) $\lambda = 2.2\,\mathrm{m}$

(c) $\lambda = 2.6\,\mathrm{m}$

(d) $\lambda = 5.6\,\mathrm{m}$

Figure 6.11 – Absolute pressure normal to the wetted surface exerted on the bottom of the wave energy converter for $H = 0.25\,\mathrm{m}$ and different wavelengths λ at $t = 8\,\mathrm{s}$

The second wave energy conversion stage describes the conversion of the absorbed energy into useful mechanical energy using the power-take-off system. Thus, the energy in the power-take-off system is of great interest and is further investigated for different wave conditions. The energy in the power-take-off system is listed in table 6.5 for all conducted simulations and in table 6.1 for experiments and is determined by equation 5.23. When comparing the data obtained by simulations with the one measured during experiments, deviations occur. These deviations can be explained when comparing the power in the power-take-off system measured during simulations to the one measured during experiments in figure 6.16 - 6.20.

It is noticeable, that simulations achieve higher values of the power in the power-take-off

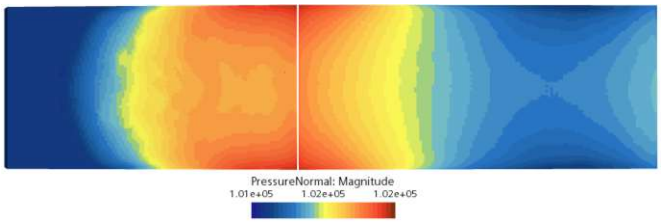

(a) $\lambda = 3.1\,\mathrm{m}$

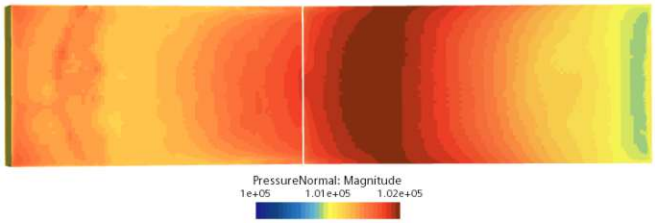

(b) $\lambda = 4\,\mathrm{m}$

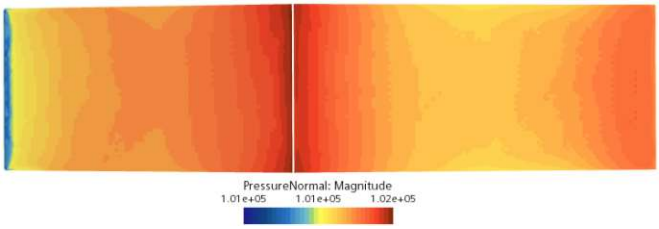

(c) $\lambda = 5.1\,\mathrm{m}$

Figure 6.12 – Absolute pressure normal to the wetted surface exerted on the bottom of the wave energy converter for $H = 0.20\,\mathrm{m}$ and different wavelengths λ at $t = 8\,\mathrm{s}$

system for some wave conditions and experiments for others. This is also reflected in the absolute values of the energy in the power-take-off system of the simulations in table 6.5 and of experiments in table 6.1. Thereby, the simulation or the experiment with a greater power characteristic achieves higher energy in the power-take-off system as the experiment or the simulation. However, this does not apply to two simulations, which model waves of $H = 0.25\,\mathrm{m}$, $\lambda = 5.6\,\mathrm{m}$ and $H = 0.15\,\mathrm{m}$, $\lambda = 2.6\,\mathrm{m}$. Hereby, the power characteristic of the simulation is smaller than the one of the experiment, but the calculated energy in the power-take-off system for the simulations is greater than for experiments. This is due to the fact, that the push motion in figures 6.16d and 6.18c experience a significant delay during the experiments compared to the simulations. Hence, the last executed push motion at the end of the simulations is completed, while the push motion in the experiments has just started. This additional push motion in the simulations contributes to the energy in the power-take-off system leading to greater calculated values in the simulations even though the power characteristics are smaller compared to the experiments.

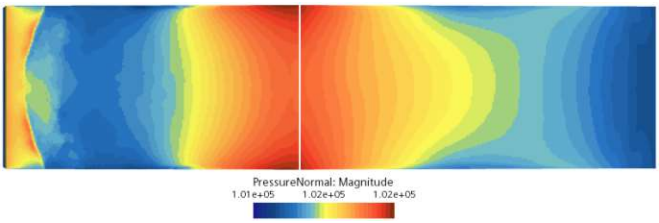

(a) $\lambda = 1.9\,\mathrm{m}$

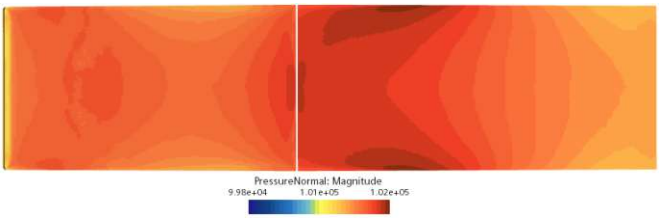

(b) $\lambda = 2.2\,\mathrm{m}$

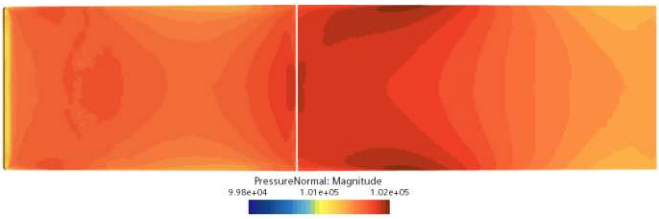

(c) $\lambda = 2.6\,\mathrm{m}$

Figure 6.13 – Absolute pressure normal to the wetted surface exerted on the bottom of the wave energy converter for $H = 0.15\,\mathrm{m}$ and different wavelengths λ at $t = 8\,\mathrm{s}$

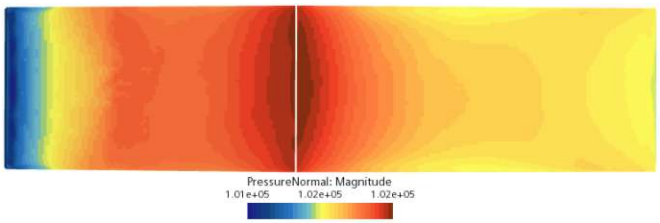

(a) $\lambda = 3.1\,\mathrm{m}$

Figure 6.14 – Absolute pressure normal to the wetted surface exerted on the bottom of the wave energy converter for $H = 0.125\,\mathrm{m}$ and different wavelengths λ at $t = 8\,\mathrm{s}$

Another point to consider is, that there should not be any power in the power-take-off system during the pull motion, since the power-take-off system applied to both the experiment and the simulation corresponds to the fourth model of table 5.4. However, contrary to simulations, where no power acts in the power-take-off system during the pull motion, there is power in the power-take-off system during the pull motion in all conducted experiments. This additional power obtained during the pull motion contributes to the energy in the power-take-off system during experiments, but is considered insignificant compared to the power in the power-take-off system during the push motion.

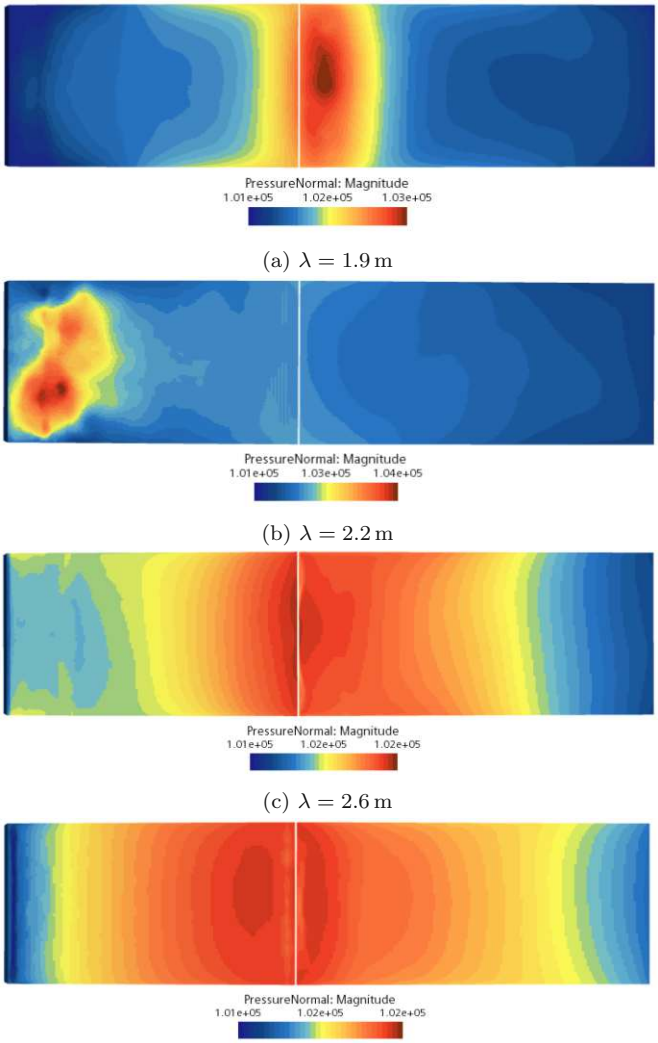

(a) $\lambda = 1.9\,\mathrm{m}$

(b) $\lambda = 2.2\,\mathrm{m}$

(c) $\lambda = 2.6\,\mathrm{m}$

(d) $\lambda = 3.1\,\mathrm{m}$

Figure 6.15 – Absolute pressure normal to the wetted surface exerted on the bottom of the wave energy converter for $H = 0.05\,\mathrm{m}$ and different wavelengths λ at $t = 8\,\mathrm{s}$

Overall, the energy in the power-take-off system is sufficiently simulated with CFD and actually represents the desired working principle of the fourth power-take-off system even better than in experiments. Especially, the power characteristics of the simulated wave energy converter operating in waves with long wavelengths and high wave heights are a good approximation to the experiments. However, more significant deviations of the simulations from the experiments occur for the shortest wavelength in different wave heights.

The efficiency of the second wave energy conversion stage is determined by the ratio of the energy in the power-take-off system and the energy exerted on the device. Thereby, the energy exerted on the device is determined by equation 5.22 only considering

hydrodynamic forces. On the contrary, the energy in the power-take-off system is calculated according to equation 5.23 using the velocity and the force in the spring-damper coupling. These are both affected by the motion of the wave energy converter, which responds not only to the hydrodynamic forces but also to the force of the mooring system. Hence, the energy in the power-take-off system also takes into account these additional loads. Subsequently, the two energies are not comparable, which is why the efficiency of the second wave energy conversion stage is not calculated in table 6.5. Generally, it is assumed that energy is lost at each energy conversion stage. This is in agreement with the results in table 6.5, where the theoretical wave energy is greater than the energy exerted on the device which in turn is again greater than the energy in the power-take-off system. However, the energy exerted on the device is smaller than the energy in the power-take-off system for some wave conditions in table 6.5. This misleadingly indicates an increase in energy in the second wave energy conversion stage. However, this is attributed to the additional loads which are considered in the energy in the power-take-off system, but not in the energy exerted on the device. For some wave conditions, these additional loads appear to have a greater impact on the device.

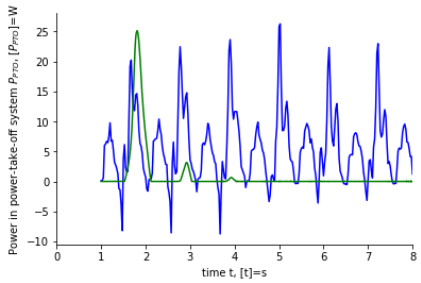

(a) $\lambda = 1.9\,\mathrm{m}$

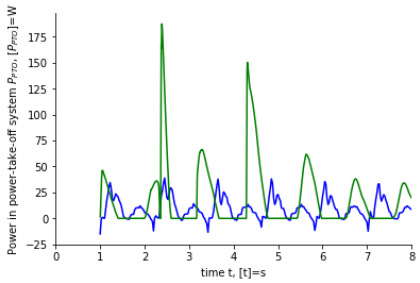

(b) $\lambda = 2.2\,\mathrm{m}$

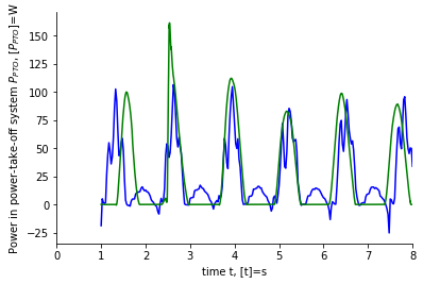

(c) $\lambda = 2.6\,\mathrm{m}$

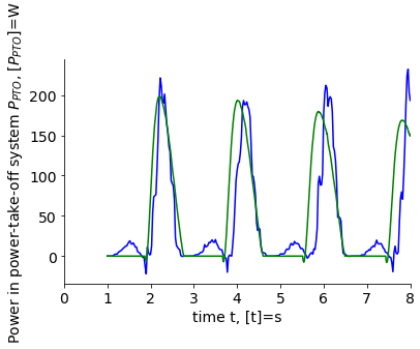

(d) $\lambda = 5.6\,\mathrm{m}$

Figure 6.16 – Comparison of the power in the fourth power-take-off system measured during experiments (blue solid line) and simulations (green solid line) with waves of a wave height of $H = 0.25\,\mathrm{m}$

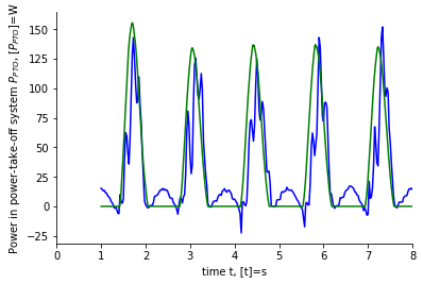

(a) $\lambda = 3.1\,\mathrm{m}$

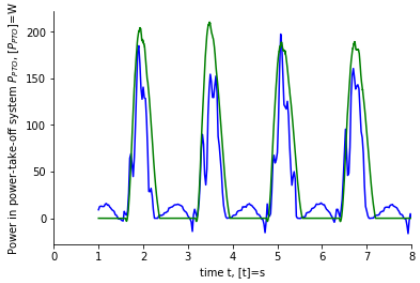

(b) $\lambda = 4\,\mathrm{m}$

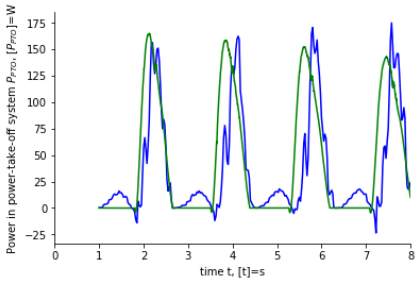

(c) $\lambda = 5.1\,\mathrm{m}$

Figure 6.17 – Comparison of the power in the fourth power-take-off system measured during experiments (blue solid line) and simulations (green solid line) with waves of a wave height of $H = 0.20\,\mathrm{m}$

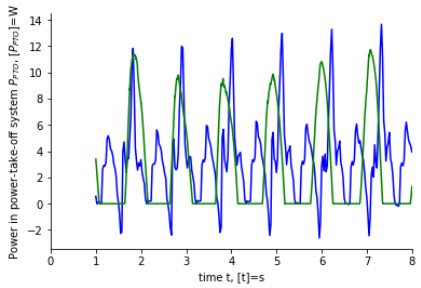

(a) $\lambda = 1.9\,\mathrm{m}$

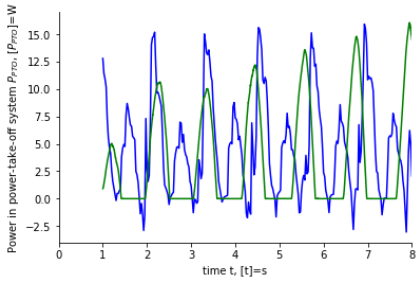

(b) $\lambda = 2.2\,\mathrm{m}$

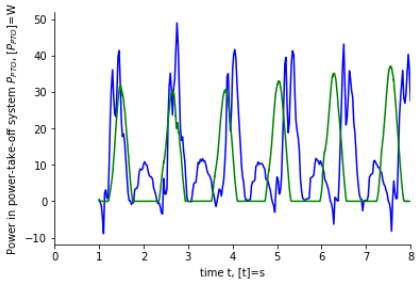

(c) $\lambda = 2.6\,\mathrm{m}$

Figure 6.18 – Comparison of the power in the fourth power-take-off system measured during experiments (blue solid line) and simulations (green solid line) with waves of a wave height of $H = 0.15\,\mathrm{m}$

However, the energy in the power-take-off system determines the overall efficiency according to equation 5.25. Therefore, parallels can be established between the energy

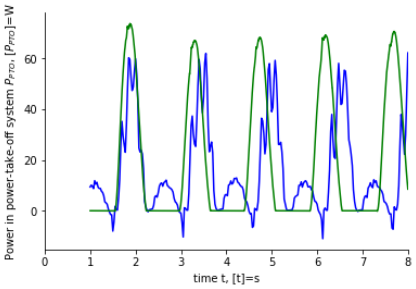

(a) $\lambda = 3.7\,\mathrm{m}$

Figure 6.19 – Comparison of the power in the fourth power-take-off system measured during experiments (blue solid line) and simulations (green solid line) with waves of a wave height of $H = 0.125\,\mathrm{m}$

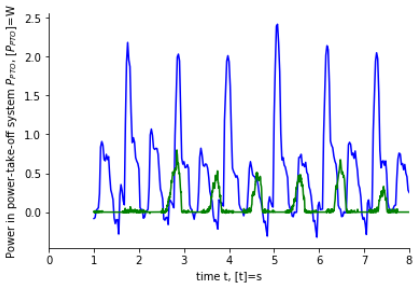

(a) $\lambda = 1.9\,\mathrm{m}$

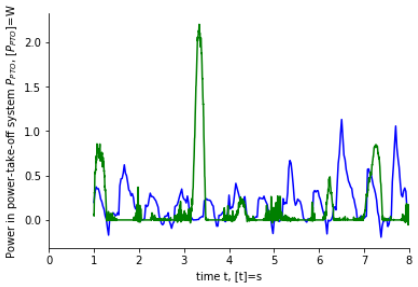

(b) $\lambda = 2.2\,\mathrm{m}$

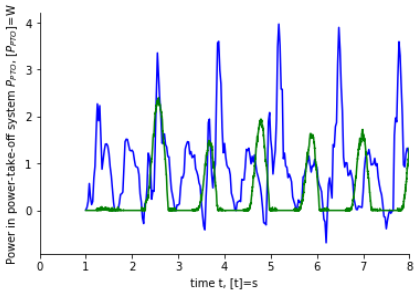

(c) $\lambda = 2.6\,\mathrm{m}$

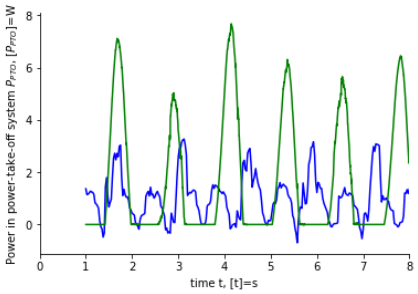

(d) $\lambda = 3.1\,\mathrm{m}$

Figure 6.20 – Comparison of the power in the fourth power-take-off system measured during experiments (blue solid line) and simulations (green solid line) with waves of a wave height of $H = 0.05\,\mathrm{m}$

in the power-take-off system and the efficiency. Additionally, the energy in the power-take-off system is also influenced by the first wave energy conversion stage.

The results in table 6.5 indicate, that the power in the power-take-off system as well as the overall efficiency increases with an increasing wavelength at a constant wave height as long as the wavelength is smaller than the length of the device ($\lambda < L_{device}$), but decreases if the wavelength exceeds the length of the device ($\lambda > L_{device}$). This resembles the behaviour of the first wave energy conversion stage. Thereby, its influence on the energy in the power-take-off system becomes apparent indicating that an efficient

capturing of hydrodynamic forces is essential to obtain good efficiencies. Moreover, this tendency is also observed in table 6.1 which presents the results of experiments at the Danish Hydraulic Institute. However, this does not apply to the wave energy converter operating in a wave height of $H = 0.25\,\mathrm{m}$ as its efficiency continues to increase although the wavelength already exceeded the length of the device.

The overall efficiency varies from approximately 2 % to 86 % depending on the wave condition. The least efficiencies are achieved for wavelengths of $\lambda = 1.9\,\mathrm{m}$ and different wave heights in table 6.5. In these wave conditions, the influence of the motion of the device is added to the one of the hydrodynamic forces. The hydrodynamic forces are already transmitted inefficiently, since the wave energy converter tends to float on top of the wave crests when operating in such short wavelength conditions. This additionally causes the wave energy converter not to respond to the wave motion. Because of the lacking movement of the wave energy converter, the spring-damper velocity as well as the force in the spring-damper coupling is reduced, which results in less power overall. On the contrary, the best efficiencies are reached for wavelengths similar to the length of the device. Hereby, the hydrodynamic forces can be absorbed optimally by the wave energy converter. Additionally, the wave energy converter is able to follow the wave motion perfectly. Thereby the spring-damper velocity and the force in the spring-damper coupling is influenced positively, resulting in high efficiencies.

Figure 6.21 compares the overall efficiency of the wave energy converter in different wave conditions during experiments and simulations. Every blue dot represents an experiment at a certain wave steepness s, while the associated orange cross denotes the simulation. When comparing the CFD simulations with experiments in figure 6.21, deviations are noticeable. The maximum efficiency is obtained for the wave energy converter operating in waves of a wave height of $H = 0.125\,\mathrm{m}$ and a wavelength of $\lambda = 3.7\,\mathrm{m}$ and is 66 % during experiments and 86 % in conducted CFD simulations. This results in a deviation of 20 % between experiments and simulations. Within waves characterized by a wave height of $H = 0.2\,\mathrm{m}$ and a wavelength of $\lambda = 4\,\mathrm{m}$ the wave energy converter in the simulation is the second most efficient with an efficiency of 76 %. This also applies to the experiment, where an efficiency of 54 % is obtained. Thus, the simulation deviates from the experiment by approximately 22 %. The minimum efficiency during the simulation is obtained in waves with a wave height of $H = 0.25\,\mathrm{m}$ and a wavelength of $\lambda = 1.9\,\mathrm{m}$ and

equals 2 %. However, the minimum efficiency during experiments is 6 % and is achieved within waves of a wave height of $H = 0.05\,\mathrm{m}$ and a wavelength of $\lambda = 2.2\,\mathrm{m}$. The wave energy converter in these wave conditions also yields one of the least efficiencies of 5 % within simulations. Comparing the simulation to the experiment results in a deviation of 1 %. These deviations arise because the power characteristics differ in the simulation and the experiment. The power characteristics of experiments are recorded after the wave energy converter has already been operating properly in waves for some time, whereby the influence of initial conditions is minimized and the wave field resulting from the motion of the device is fully developed. On the contrary, the power characteristics of the simulation is recorded after a simulated time of 1 s. Although, the first second of the simulation is excluded and the power characteristics in figures 6.16 - 6.20 seem to have converged, the deviations in the power characteristics and consequently in the efficiency of simulations and experiments indicate that there still is influence of initial conditions in the simulated power characteristics. This is due to the fact, that the wave energy converter has just started to move. In addition, the wave field resulting from the motion of the device has not been able to develop properly within the simulated time of 8 s especially for simulations with waves of longer wavelengths. The wake established and the waves radiating away from the device influence the incident wave height and therefore the efficiency. Longer lasting simulations enable to include these effects. This allows a better comparison between experimental and simulated power characteristics. Another point to consider is that friction losses are neglected within the simulations, although they do occur in experiments.

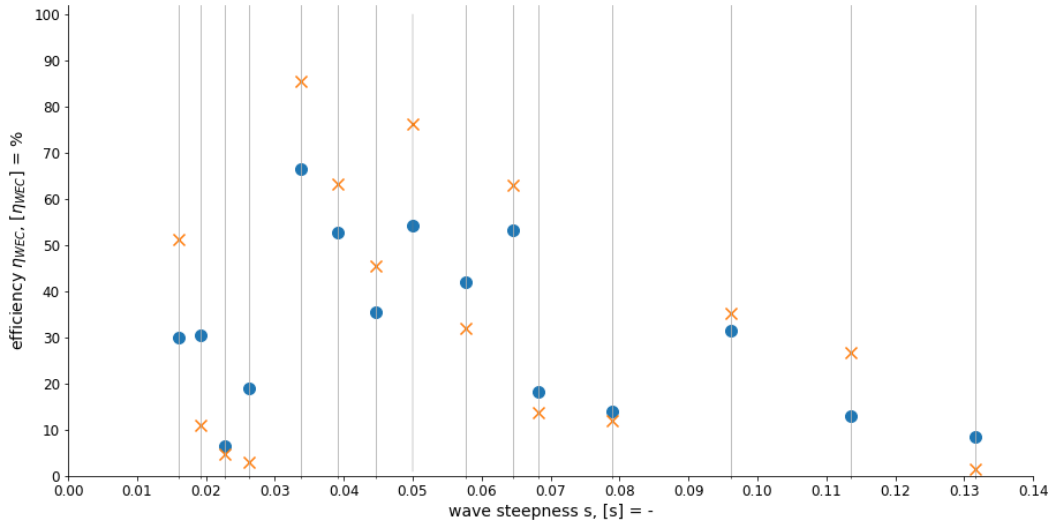

Figure 6.21 – Comparison of the efficiency of the wave energy converter during experiments (blue dots) and simulations (orange crosses)

All points considered, conducted simulations resemble experiments, with deviations from simulations to experiments that are considered acceptable. Therefore, despite the deviation, the performance and the behaviour of the wave energy converter in different wave conditions can be reasonably predicted with these simulations.

6.6 Flow analysis in different wave conditions

Just as waves influence the performance of the wave energy converter, the wave energy converter also has an impact on the waves. Therefore, the impact of the wave energy converter equipped with the fourth power-take-off system on the waves of different wave conditions is studied.

The wave fields resulting from the wave energy converter operating in different wave conditions are displayed in figure 6.22 - 6.26.

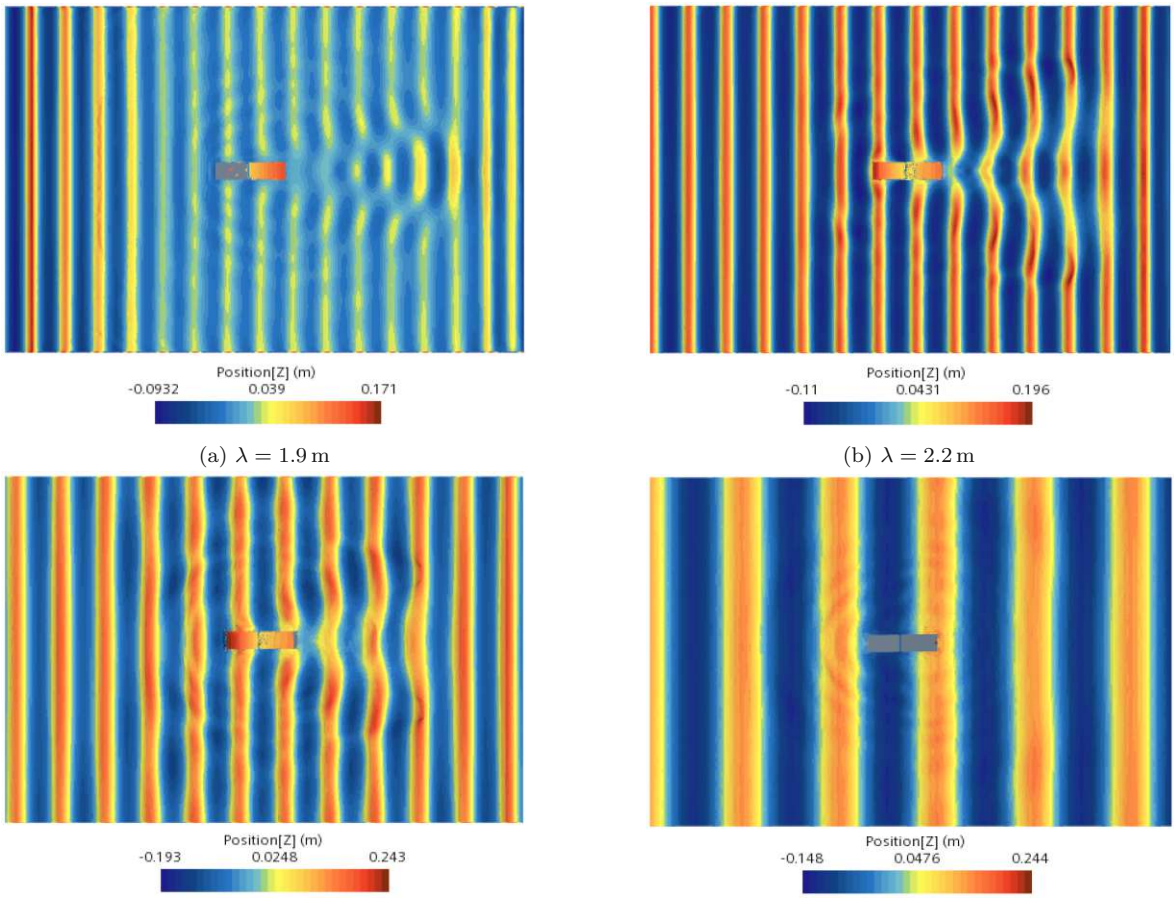

(a) $\lambda = 1.9\,\mathrm{m}$ (b) $\lambda = 2.2\,\mathrm{m}$

(c) $\lambda = 2.6\,\mathrm{m}$ (d) $\lambda = 5.6\,\mathrm{m}$

Figure 6.22 – Wave fields resulting from the wave energy converter operating in waves of a wave height of $H = 0.25\,\mathrm{m}$ at different wavelengths λ at $t = 8s$

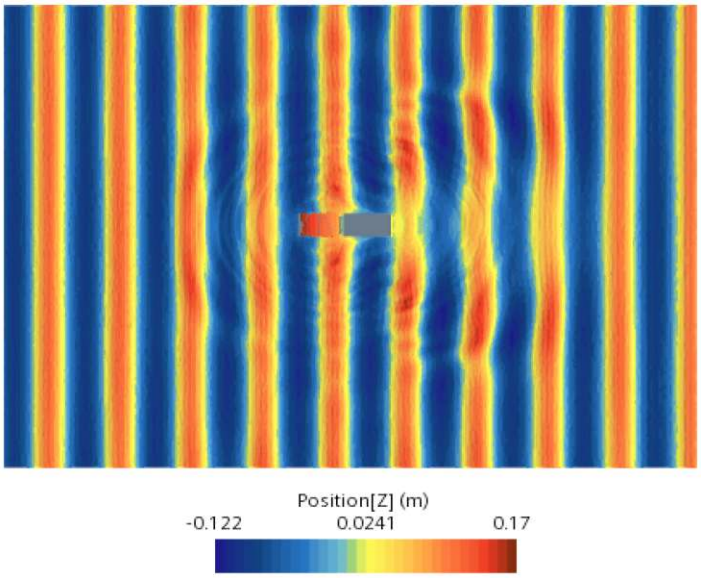

(a) $\lambda = 3.1\,\mathrm{m}$

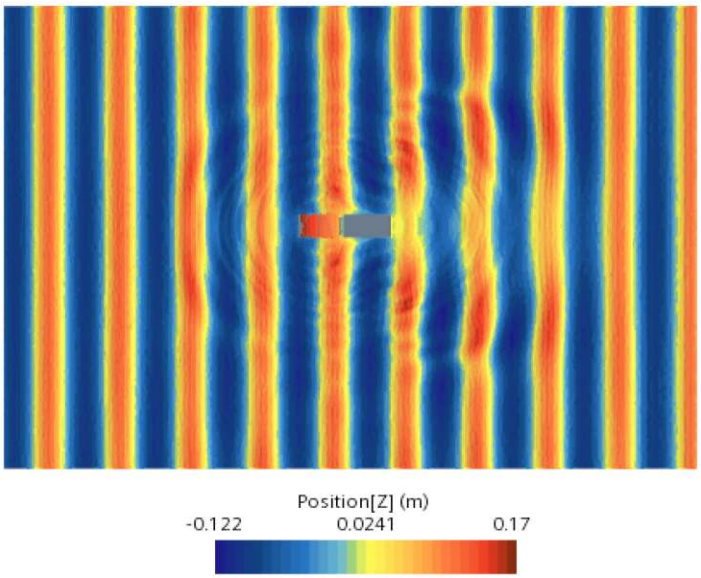

(b) $\lambda = 4\,\mathrm{m}$

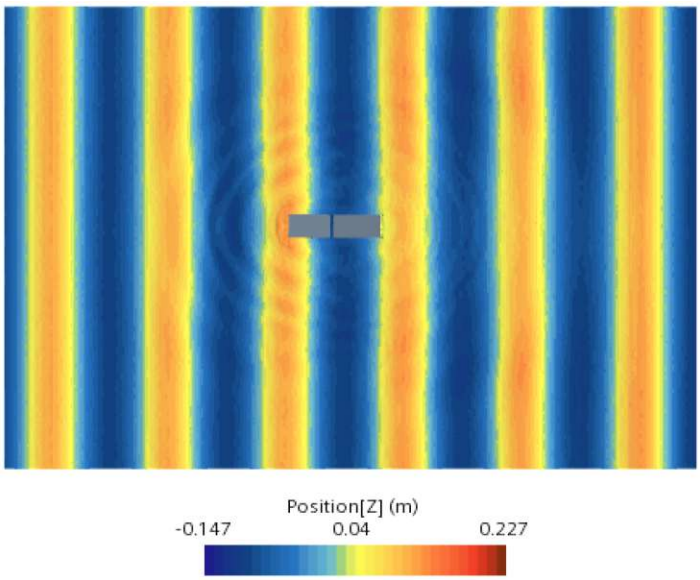

(c) $\lambda = 5.1\,\mathrm{m}$

Figure 6.23 – Wave fields resulting from the wave energy converter operating in waves of a wave height of $H = 0.20\,\mathrm{m}$ at different wavelengths λ at $t = 8s$

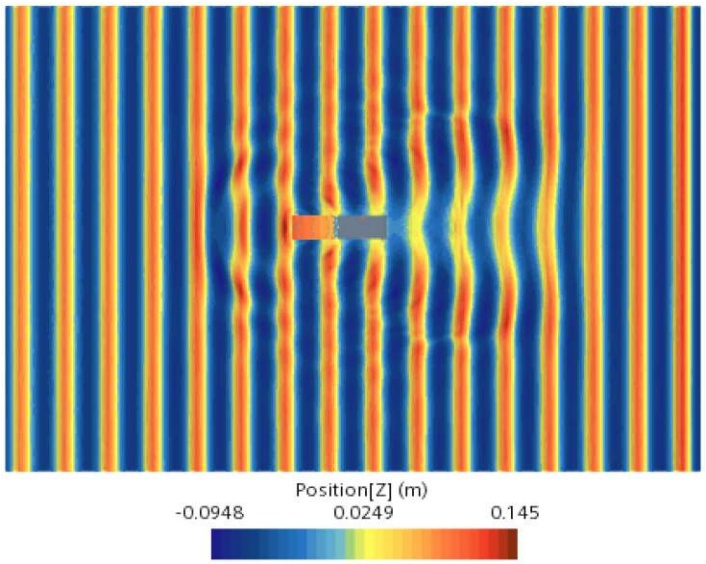

(a) $\lambda = 1.9\,\mathrm{m}$

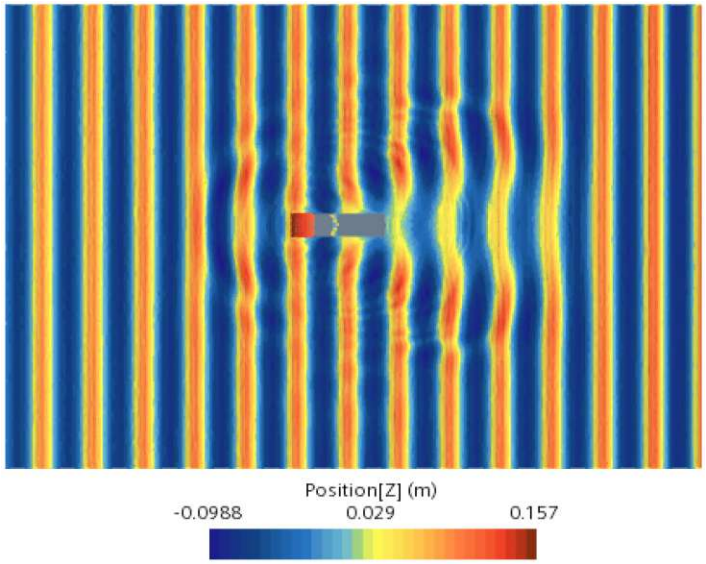

(b) $\lambda = 2.2\,\mathrm{m}$

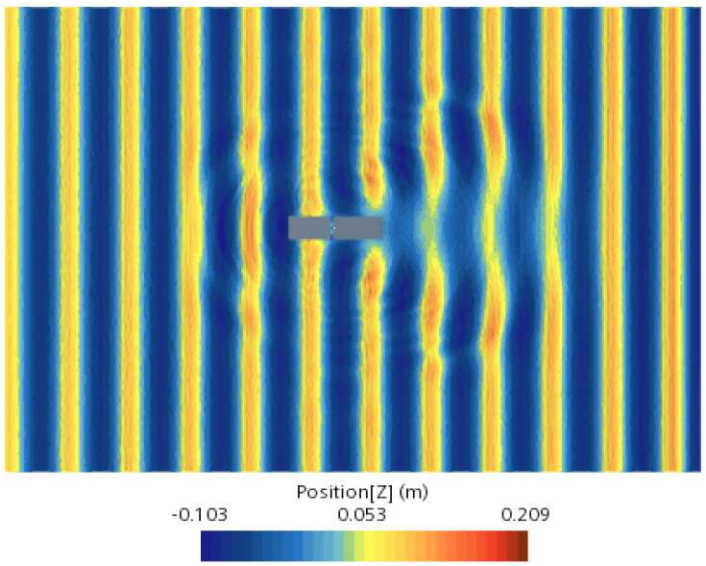

(c) $\lambda = 2.6\,\mathrm{m}$

Figure 6.24 – Wave fields resulting from the wave energy converter operating in waves of a wave height of $H = 0.15\,\mathrm{m}$ at different wavelengths λ at $t = 8s$

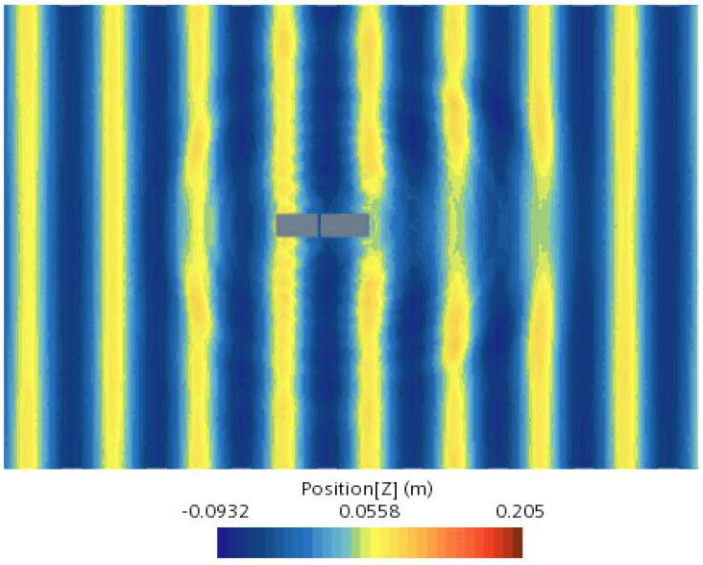

(a) $\lambda = 3.7\,\mathrm{m}$

Figure 6.25 – Wave fields resulting from the wave energy converter operating in waves of a wave height of $H = 0.125\,\mathrm{m}$ at different wavelengths λ at $t = 8s$

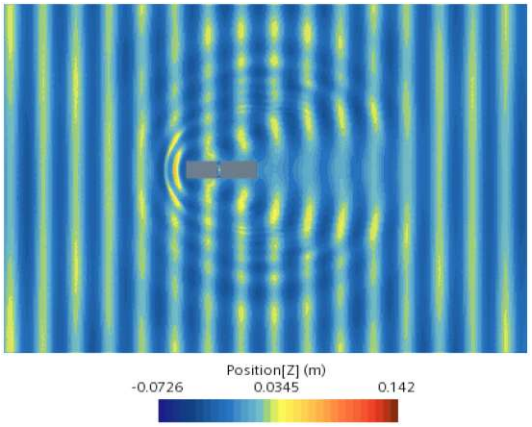

(a) $\lambda = 1.9\,\mathrm{m}$

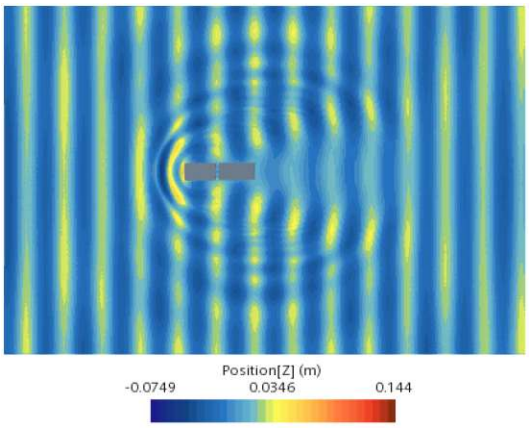

(b) $\lambda = 2.2\,\mathrm{m}$

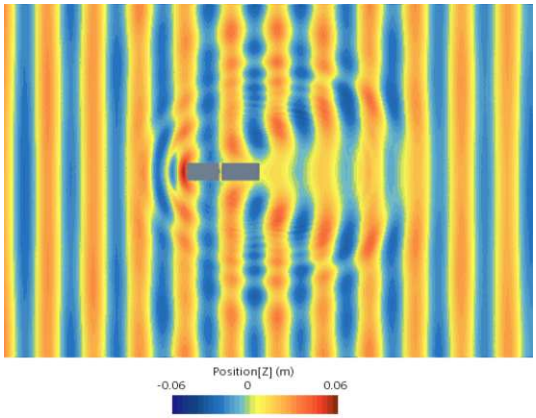

(c) $\lambda = 2.6\,\mathrm{m}$

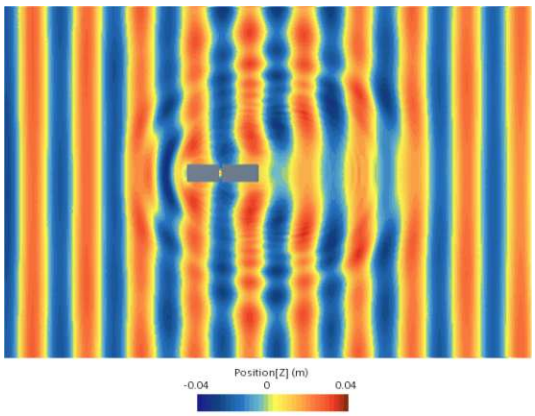

(d) $\lambda = 3.1\,\mathrm{m}$

Figure 6.26 – Wave fields resulting from the wave energy converter operating in waves of a wave height of $H = 0.05\,\mathrm{m}$ at different wavelengths λ at $t = 8s$

First of all, water is on top of the wave energy converter when operating in waves characterized by small wave lengths λ and high wave heights H. In these wave conditions, water sloshes onto the device, which can be observed in figures 6.22 - 6.24. This is also observed during experiments at the Danish Hydraulic Institute, where a shield was attached to prevent the water from splashing onto the device. However, this shield is not yet integrated into the CFD simulations.

Secondly, the waves radiating from the wave energy converter are clearly visible for all conducted simulations in figures 6.22 - 6.26. The radiated waves do not reach the boundary of the domain indicating that a reflection of the waves on the boundaries can be excluded. Furthermore, it is observed that a wake is established in all simulations with a wave length of $\lambda \leq 3.7\,\mathrm{m}$. The wake is more pronounced for shorter wavelengths and attains the typical V-shape. Its intensity decreases with an increasing wavelength λ and the wake disappears completely from a wavelength of $\lambda \geq 4\,\mathrm{m}$. This is due to the fact that the propagating waves must first be incident on the wave energy converter so that the wake can be developed. As all simulations only last 8 s, more waves pass the wave energy converter the shorter the wavelength allowing the wake to develop. In simulations with a longer wavelength, the wake has not been able to develop within the simulated time, as not enough waves have been incident on the wave energy converter. However, a wake is also expected to develop in simulations with a longer wavelength when proceeding the simulation.

Thirdly, the colour bars in figures 6.22 - 6.26 are distorted, as the maximal values are hardly reached. However, figures 6.22 - 6.26 represent the wave field resulting from the wave energy converter qualitatively satisfactory.

The wave elevation before, immediately after, and downstream of the device is further investigated.

The wave elevation of the incident waves is measured 9.1 m in front of the device and is shown on the left plot of figures 6.27 - 6.31. At this position, the waves should not yet be affected by the radiated waves, so the wave elevation of the simulated waves can be validated by comparing it to the linear wave theory. Generally, the wave elevation of the incident waves constitutes a good approximation to the linear wave theory. It is noticeable that the wave elevation of the incident waves deviates more from the linear wave theory for higher wave heights and shorter wavelengths. These deviations originate

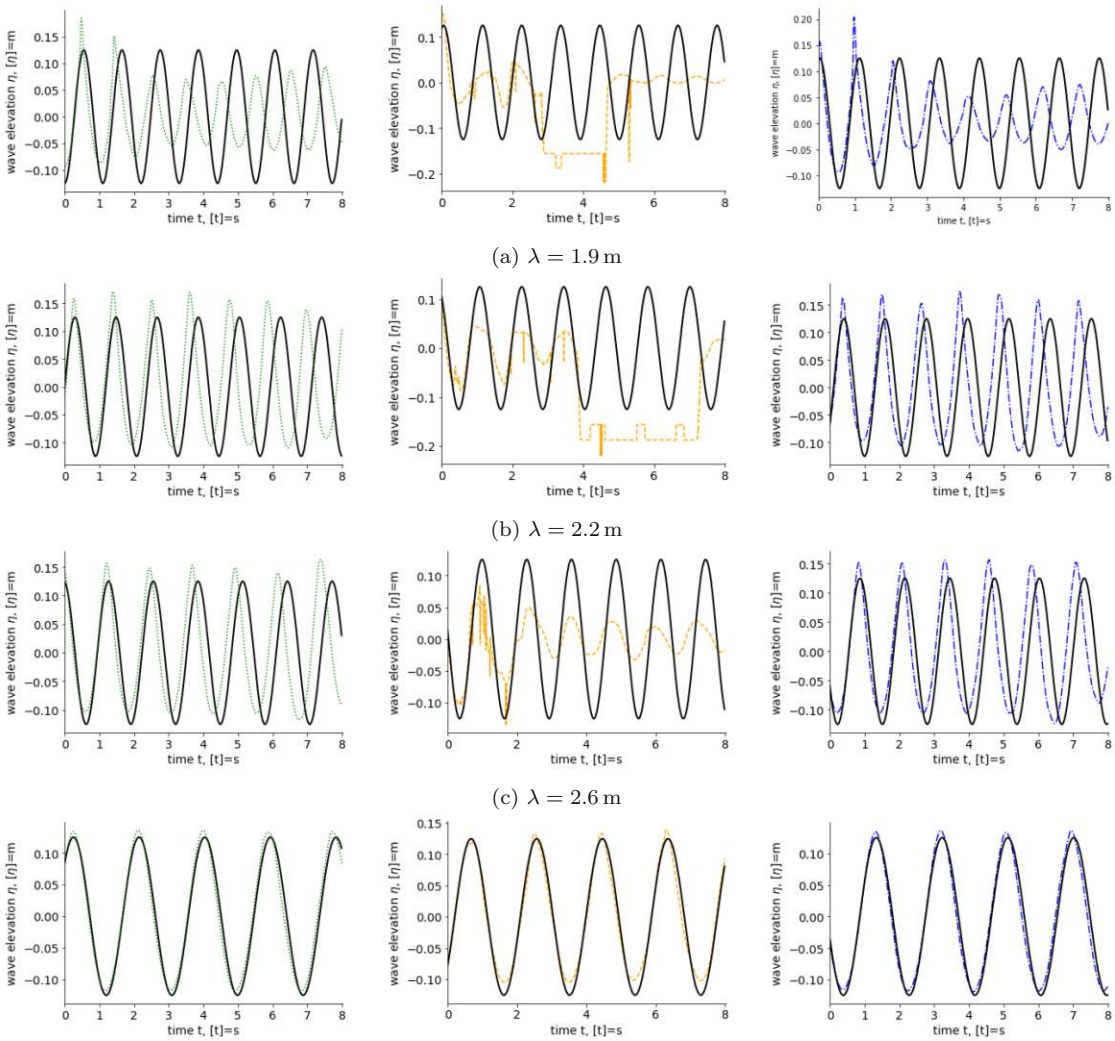

(a) $\lambda = 1.9\,\mathrm{m}$

(b) $\lambda = 2.2\,\mathrm{m}$

(c) $\lambda = 2.6\,\mathrm{m}$

(d) $\lambda = 5.6\,\mathrm{m}$

Figure 6.27 – Wave elevation η for simulated waves having a wave height of $H = 0.25\,\mathrm{m}$ measured at different locations in the wave tank and compared to waves according to the linear wave theory (solid black): 9.1 m in front of the device (left, dotted green), 0.1 m after the device (middle, dashed orange), 8.45 m after the device (right, dashed-dotted blue)

from the mesh alignment to the waves and are considered insignificant. However, significant deviations of the simulated wave elevation from the one of the linear wave theory can be observed for incident waves characterized by the highest simulated wave height of $H = 0.25\,\mathrm{m}$ and shortest wavelengths of $\lambda = 1.9\,\mathrm{m}$ and $\lambda = 2.2\,\mathrm{m}$. In these cases, a superposition of the incident wave with the waves radiating from the device already occurred.

The wave height before and after the device is compared in table 6.6 for all conducted simulations with different wave conditions. The wave height H before the device corresponds to the implemented wave height and the wave height after the device

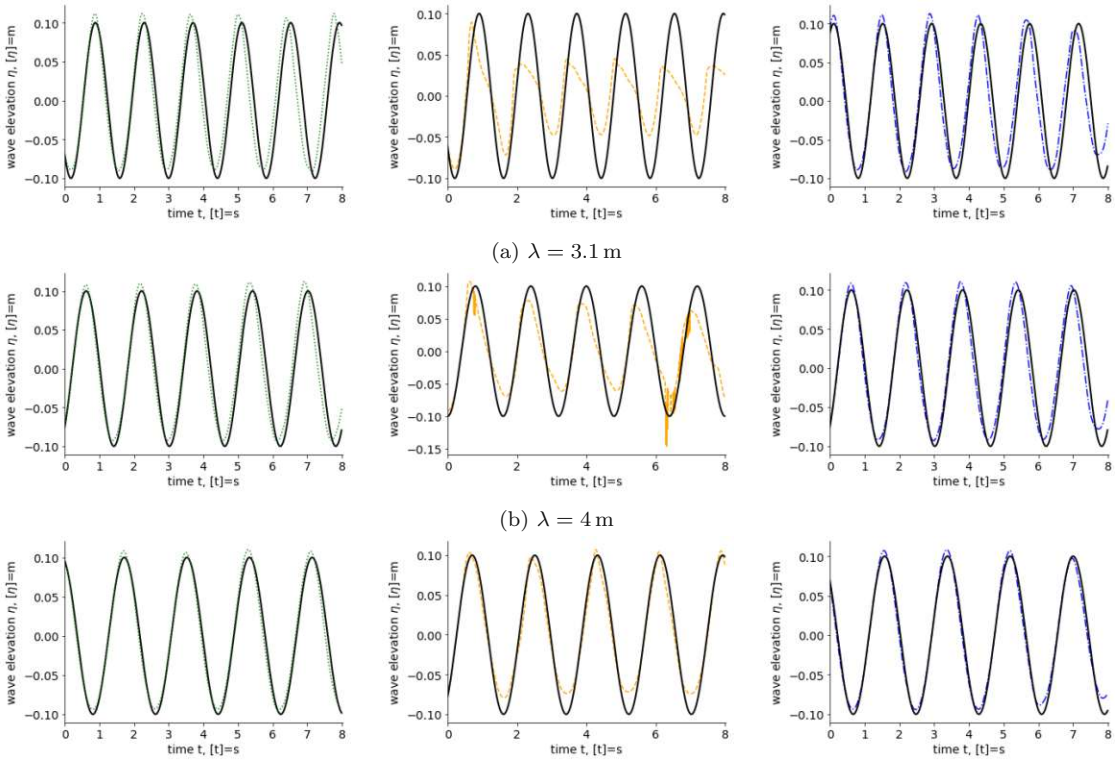

(a) $\lambda = 3.1\,\mathrm{m}$

(b) $\lambda = 4\,\mathrm{m}$

(c) $\lambda = 5.1\,\mathrm{m}$

Figure 6.28 – Wave elevation η for simulated waves having a wave height of $H = 0.2\,\mathrm{m}$ measured at different locations in the wave tank and compared to waves according to the linear wave theory (solid black): 9.1 m in front of the device (left, dotted green), 0.1 m after the device (middle, dashed orange), 8.45 m after the device (right, dashed-dotted blue)

H_{After} is determined by the sum of absolute value of the averaged local maxima and minima measured 0.1 m downstream the device. All waves of different wave conditions experience a significant decrease of the wave height downstream of the wave energy converter. This is also illustrated in the middle plots of figures 6.27 - 6.31. Next, the wave energy before E_{Waves} and after $E_{WavesAfter}$ the device are calculated with equation 5.21 using the corresponding wave height and are listed in table 6.6. Since the wave amplitude is proportional to the wave energy E_{Waves}, a decreased wave elevation downstream the device implies a decreased wave energy at this point. Thus, the wave energy converter must have absorbed the wave energy to maintain the conservation of energy. Therefore, the difference between the wave energy before and after the device ΔE corresponds to the energy exerted on the device $E_{OnDevice}$. When comparing the difference of the wave energy before and after the device ΔE with the energy exerted on the device $E_{OnDevice}$ deviations occur. These inaccuracies are due to the data processing as the wave height is determined by the averaged values of the local maxima and minima.

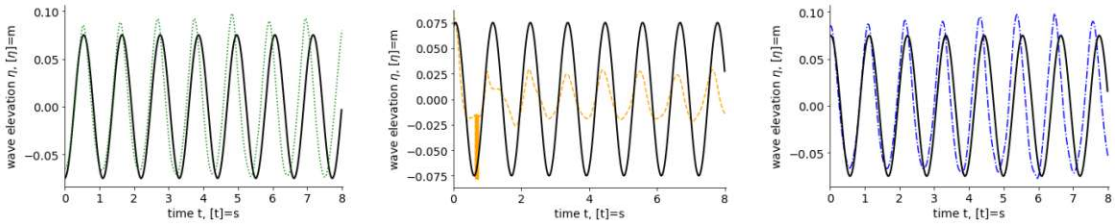

(a) $\lambda = 1.9\,\mathrm{m}$

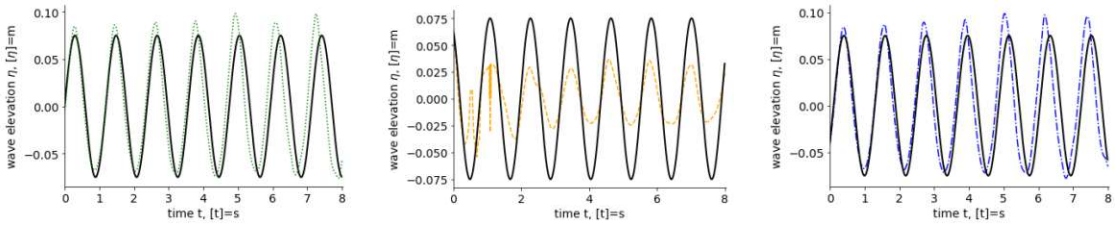

(b) $\lambda = 2.2\,\mathrm{m}$

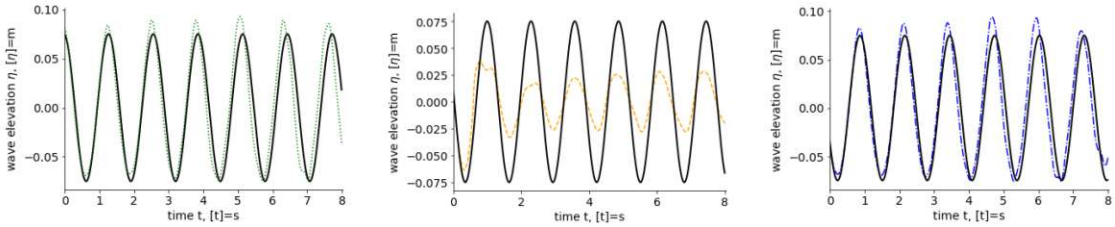

(c) $\lambda = 2.6\,\mathrm{m}$

Figure 6.29 – Wave elevation η for simulated waves having a wave height of $H = 0.15\,\mathrm{m}$ measured at different locations in the wave tank and compared to waves according to the linear wave theory (solid black): 9.1 m in front of the device (left, dotted green), 0.1 m after the device (middle, dashed orange), 8.45 m after the device (right, dashed-dotted blue)

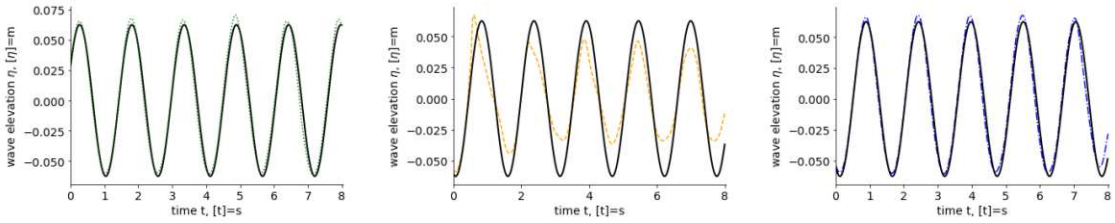

(a) $\lambda = 3.7\,\mathrm{m}$

Figure 6.30 – Wave elevation η for simulated waves having a wave height of $H = 0.125\,\mathrm{m}$ measured at different locations in the wave tank and compared to waves according to the linear wave theory (solid black): 9.1 m in front of the device (left, dotted green), 0.1 m after the device (middle, dashed orange), 8.45 m after the device (right, dashed-dotted blue)

Hence, the wave height after the device H_{After} does not correspond precisely to the actual values of the wave height after the device, which consequently influences the wave energy after the device $E_{WavesAfter}$ and thus the difference between the wave energy before and after the device ΔE. Moreover, there are some inaccuracies in the wave elevation in figure 6.27 for a wavelength of $\lambda = 1.9\,\mathrm{m}$ and $\lambda = 2.2\,\mathrm{m}$. These inaccuracies can be attributed to some outliers, which consequently falsify the display of the data.

Table 6.6 – Comparison of the incident with downstream wave parameters

wave steepness $[s] = -$	wave height $[H] = \mathrm{m}$	wave period $[T] = \mathrm{s}$	wave length $[\lambda] = \mathrm{m}$	average wave height after the device $[H_{After}] = \mathrm{m}$	wave energy incident on device $[E_{Waves}] = \mathrm{J}$	wave energy after the device $[E_{WavesAfter}] = \mathrm{J}$	energy difference $[\Delta E] = \mathrm{J}$	energy on device $[E_{OnDevice}] = \mathrm{J}$
0.1316	0.250	1.10	1.9	0.0530	462.01	20.79	441.22	30.10
0.1136	0.250	1.20	2.2	0.0791	497.14	49.81	447.33	154.42
0.0962	0.250	1.30	2.6	0.0839	540.45	60.91	479.55	337.26
0.0446	0.250	1.90	5.6	0.2342	793.17	696.09	97.08	383.65
0.0645	0.200	1.40	3.1	0.1069	377.69	107.86	269.83	252.60
0.0500	0.200	1.60	4.0	0.1494	429.02	239.25	189.78	369.23
0.0392	0.200	1.80	5.1	0.1785	484.44	385.94	98.49	275.59
0.0789	0.150	1.10	1.9	0.0487	166.32	17.53	148.79	9.65
0.0682	0.150	1.20	2.2	0.0603	178.97	28.9	150.08	33.68
0.0577	0.150	1.30	2.6	0.0524	194.56	23.72	170.84	78.81
0.0338	0.125	1.53	3.7	0.0896	161.18	82.75	78.43	129.29
0.0263	0.050	1.10	1.9	0.0178	18.48	2.35	16.13	6.92
0.0227	0.050	1.20	2.2	0.0183	19.89	2.66	17.22	8.47
0.0192	0.050	1.30	2.6	0.0192	21.62	3.2	18.42	5.61
0.0161	0.050	1.40	3.1	0.0259	23.61	6.33	17.28	22.15

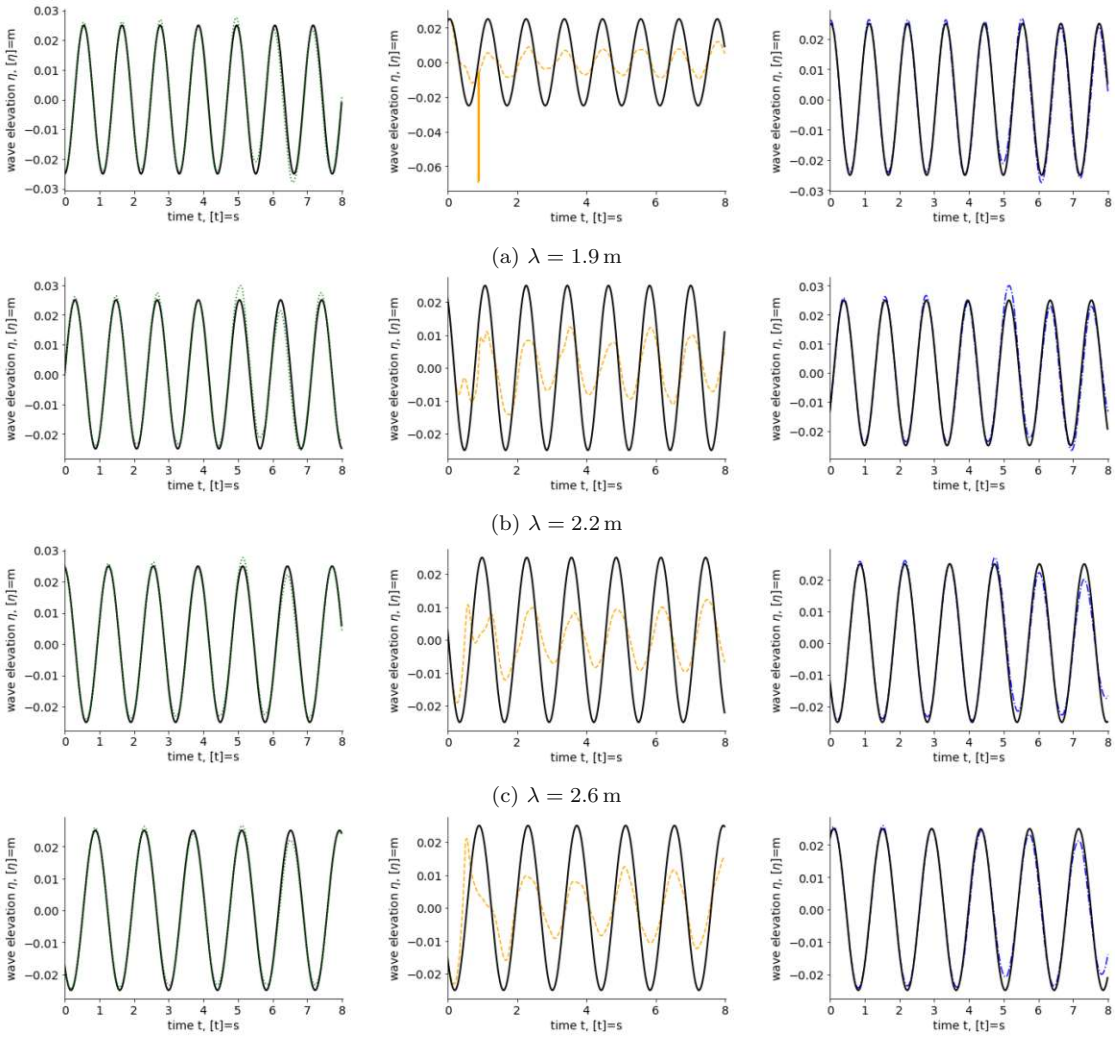

(a) $\lambda = 1.9\,\mathrm{m}$

(b) $\lambda = 2.2\,\mathrm{m}$

(c) $\lambda = 2.6\,\mathrm{m}$

(d) $\lambda = 3.1\,\mathrm{m}$

Figure 6.31 – Wave elevation η for simulated waves having a wave height of $H = 0.05\,\mathrm{m}$ measured at different locations in the wave tank and compared to waves according to the linear wave theory (solid black): 9.1 m in front of the device (left, dotted green), 0.1 m after the device (middle, dashed orange), 8.45 m after the device (right, dashed-dotted blue)

Another point to consider is that the energy exerted on the device $E_{OnDevice}$ only comprises hydrodynamic forces, whereas the difference in wave energy before and after the device ΔE takes into account all forces acting on the wave energy converter. From table 6.6 can be perceived that the difference in wave energy ΔE is generally greater than the energy exerted on the device $E_{OnDevice}$. This implies that other forces, such as the force of the mooring system or the force of the power-take-off system, also impact the transmission of wave energy to the device. For some wave conditions, the difference in wave energy before and after the device and the energy exerted on the device are comparable indicating that the influence of other forces on the power transmission is

marginal.

The middle plots of figures 6.27 - 6.31 show that the wave elevation decreases more for waves with a shorter wavelength than for waves with a longer wavelength. This is also evident in table 6.6. A greater decrease of the wave elevation implies a stronger decrease in wave energy after the device and therefore a higher energy absorption of the wave energy converter. Hence, the first energy conversion stage of the wave energy converter operating in short wavelengths should be the most efficient. This is in contradiction to experiments and the results of chapter 6.5, where it was found that the wave energy converter operates most efficiently at wavelengths similar to the length of the device. However, this tendency observed in the middle plots of figures 6.27 - 6.31 and in table 6.6 is related to the development of the wake. As more waves have been incident on the wave energy converter during the simulated time of 8 s in the simulations with shorter wavelengths than in the simulations with longer wavelengths, the wake could already develop properly in the former, which is also illustrated in figures 6.22 - 6.26. So the reduced wave elevation after the device in the simulations with shorter wavelengths is due to the waves being influenced by the wake and the waves radiating from the device. On the contrary, the waves in simulations with longer wavelengths are just influenced by the radiated waves but certainly will also be influenced by the wake when proceeding the simulation. Therefore, a comparison of the decrease of the wave elevation in different wave conditions is only viable if the simulation is continued for some time.

The right plots of figures 6.27 - 6.31 illustrate the wave elevation measured 8.45 m after the aft pontoon. The waves tend to rebuild downstream of the device and are already fully recovered for all conducted simulations except the ones with the highest wave height of $H = 0.25\,\mathrm{m}$ and the shortest wavelength of $\lambda = 1.9\,\mathrm{m}$ and $\lambda = 2.2\,\mathrm{m}$. Here, the wake still influences the waves.

6.7 Performance of different power-take-off systems

CFD simulations also enable to analyse the performance of different applications of power-take-off systems. The aim is to determine the power which is transmitted from the waves to the wave energy converter and the power in the power-take-off system.

Consequently, the efficiency of the wave energy converter can be defined and the energy loss in the first wave energy conversion stage can be identified.

In this thesis, five different power-take-off systems specified in table 5.4 are tested, which differ in the intensity of the brake effect. The brake effect is caused by the hysteresis brake which is used in the experiments at the Danish Hydraulic Institute. The hysteresis brake exerts resistance on the push rod which can be regulated by two clutches depending on the direction of the linear motion of the push rod. In the simulations, the power-take-off system is implemented as a spring-damper coupling whose force represents the resistance of the hysteresis brake. Thus, the intensity of the braking effect can be easily modelled by applying a user field function to the elastic coefficient k_e and the damping coefficient k_d which differentiates between the push and pull motion.

Generally, two types of power-take-off systems can be distinguished. Firstly, the two-way braking allows resistance during the push and the pull motion. This type is implemented within the first three power-take-off systems of table 6.7. Thereby, the intensity of the brake effect during the push and the pull motion is set equally. Another design of the two-way braking is the fifth power-take-off system in table 6.7. It is characterized by different intensities of the brake effect for the pull and push motion. Secondly, the one-way braking only enables resistance during the push motion, but no resistance during the pull motion. This assembly is tested within the fourth power-take-off system in table 6.7. The exact settings of the power-take-off systems can be found in table 5.4.

The same set-up of the simulation described in chapter 5 is used for all conducted simulations to be able to compare the results of different power-take-off systems. A wavelength of $\lambda = 4\,\mathrm{m}$ and a wave height of $H = 0.2\,\mathrm{m}$ are chosen as these wave conditions are among those with which the best efficiency of the wave energy converter is obtained during the experiments. These waves comprise theoretical energy of approximately 428.9 J. The values in table 6.7 only deviate marginally from each other due to the slightly different time periods.

On the contrary, the total energy incident on the wave energy converter varies for different power-take-off systems. It mainly consists of the hydrodynamic force in equation 3.61 originating from the pressure of the fluid, which is also impacted by the power-take-off systems. The values in table 6.7 indicate, that the total energy

Table 6.7 – Efficiency of different power-take-off systems

	PTO 1	PTO 2	PTO 3	PTO 4	PTO 5
wave energy $[E_{Waves}] = \mathrm{J}$	428.92	428.89	428.92	428.95	429.00
energy on device $[E_{OnDevice}] = \mathrm{J}$	272.59	304.85	339.12	369.23	361.71
energy in PTO $[E_{PTO}] = \mathrm{J}$	253.46	278.01	306.52	327.47	321.30
efficiency $[\eta_{WEC}] = \%$	59	65	72	76	75

exerted on the wave energy converter increases the less resistance is present in the power-take-off system during the pull motion. This implies that the energy exerted on the device is maximal when there is no resistance in the power-take-off system during the pull motion as for the fourth power-take-off. In this case, the two barges of the wave energy converter are not restricted in their relative movement away from each other and the spring-damper coupling elongates the most as shown in figure 6.32. In this way the device can follow the wave motion easily and is therefore subjected to higher hydrodynamic forces during the push motion. This allows 76 % of the theoretical wave energy to be converted within the first energy conversion stage. On the other hand, the first power-take-off system applies full resistance during the pull motion, which leads to a restriction in the movement of the device. As illustrated in figure 6.32, the spring-damper is not elongated as much and the device can not follow the wave motion as well. As a result, it is exposed to less hydrodynamic force and only achieves an efficiency of 59 % in the first wave energy conversion stage. This is in agreement with experiments, as the highest power conversion is also achieved with a one-way braking system according to [14].

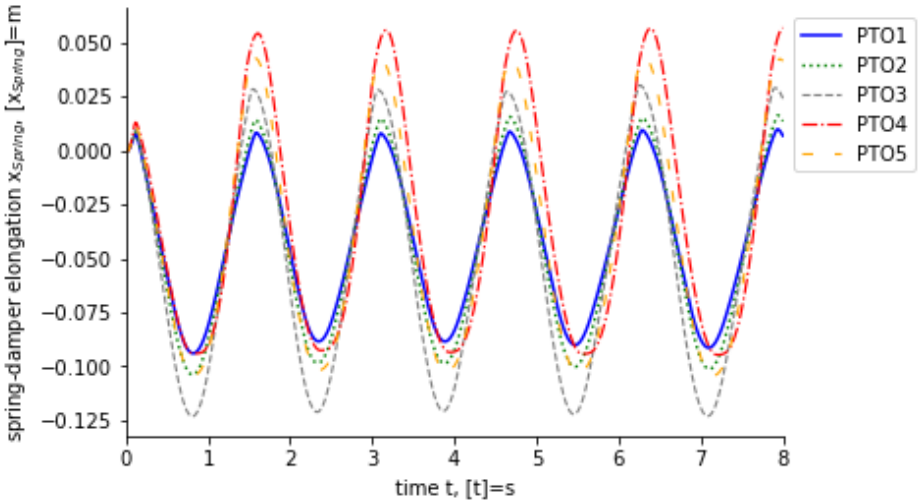

Figure 6.32 – Spring-damper elongation for different power-take-off systems operating in waves with a wave height of $H = 0.2\,\mathrm{m}$ and a wavelength of $\lambda = 4\,\mathrm{m}$

Figure 6.33 confirms that the device equipped with the fourth power-take-off system is exposed to higher hydrodynamic forces, as more pressure acts on the device compared to the one equipped with the first power-take-off system. The pressure distribution on the bottom of the device equipped with other power-take-off system can be found in the appendix A.2.3.

(a) PTO 1 (b) PTO 4

Figure 6.33 – Pressure exerted on the bottom of the wave energy converter equipped with different power-take-off system operating in waves of a wave height of $H = 0.20\,\mathrm{m}$ and a wavelength of $\lambda = 4.0\,\mathrm{m}$ at $t = 8s$

The energy in the power-take-off system is of particular interest as it ultimately indicates how much electricity can be generated and thus determines the efficiency of the wave energy converter. It depends on the applied resistance during the push and pull motion and varies accordingly. Table 6.7 indicates that the energy in the power-take-off system increases when the resistance during the pull motion is limited. Thus, the energy in the fourth power take-off system is the highest while the energy in the first power take-off system is the lowest. This is partly due to the highly efficient first wave energy

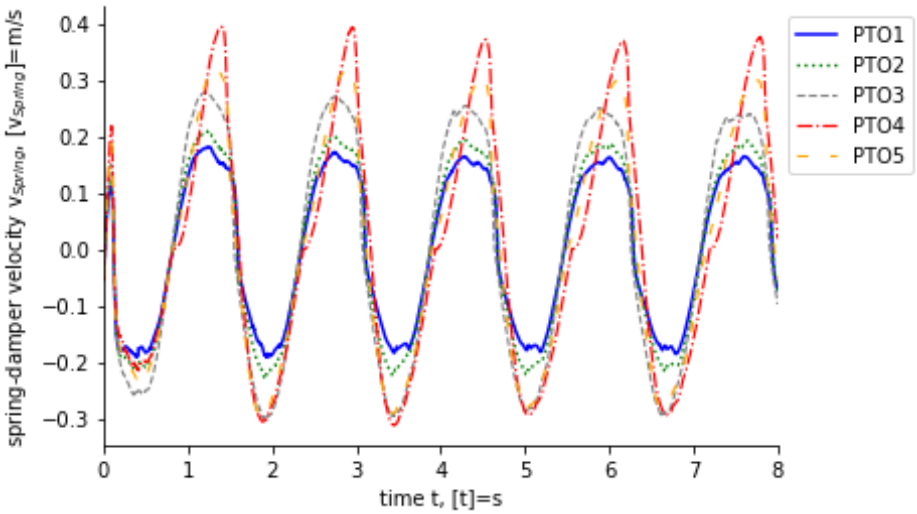

Figure 6.34 – Spring-damper velocity for different power-take-off systems operating in waves with a wave height of $H = 0.2\,\mathrm{m}$ and a wavelength of $\lambda = 4\,\mathrm{m}$

conversion stage of the fourth power-take-off system. Moreover, the energy in the power-take-off system depends on the velocity of the spring-damper coupling and the force in the spring-damper coupling. The velocity profile of the spring-damper for different power-take-off systems is shown in figure 6.34. The spring-damper velocity increases with decreasing resistance in the power-take-off system during the pull motion. This tendency also occurs during the push motion for the first three power-take-off systems. On the other hand, the spring-damper velocity of the third, fourth and fifth power-take-off systems are similar during the push motion despite different resistances, whereas it differs for power-take-off systems which employ the same resistance during the push motion as for the first and the fourth as well as the second and the fifth power-take-off system. The difference between these power-take-off systems is the applied resistance during the pull motion. Figure 6.34 shows that the spring-damper velocity during the push motion is higher for less resistance during the pull motion. It can be concluded that the intensity of the resistance during the pull motion influences the spring-damper velocity during the push motion.

The force in the spring-damper coupling depends on the applied resistance according to table 5.4 and is calculated with equation 5.5. Figure 6.35 illustrates that the force in the spring-damper during the pull motion decreases with decreasing resistance. Contrary to expectations, the decrease of the force in the power-take-off systems with constant two-way braking during the pull motion is marginal, whereas the force in

the fifth power-take-off system is diminished significantly and vanishes for the fourth power-take-off system as expected. On the other hand, the force in the power-take-off systems with a constant two-way braking increases accordingly with increasing applied resistance during the push motion. Nevertheless, the force in the first power-take-off system is not as strong as the one in the fourth power-take-off system although the same resistance is applied during the push motion, which also applies to the second and fifth power-take-off systems. This is because the force in the spring-damper coupling during the push motion is influenced by the pull motion as the force in the power-take-off system during the push motion increases the less resistance is applied during the pull motion.

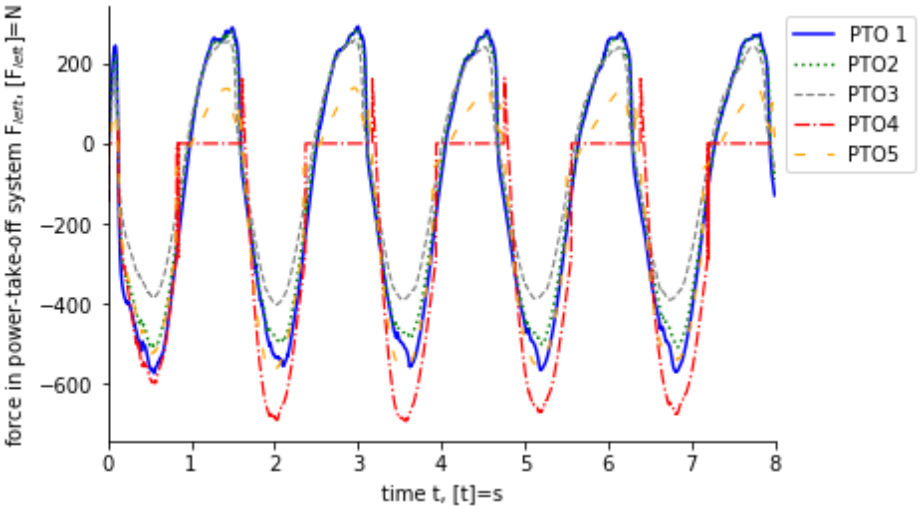

Figure 6.35 – Force in different power-take-off systems operating in waves with a wave height of $H = 0.2\,\mathrm{m}$ and a wavelength of $\lambda = 4\,\mathrm{m}$

The energy in the power-take-off system in table 6.7 is finally computed by integrating the power in the spring-damper coupling over a time period. The characteristics of the power in the power-take-off systems can be described in terms of its dependence on the spring-damper velocity and the force in the spring-damper according to equation 5.23. The power in the spring-damper coupling during the push motion increases with decreasing resistance during the pull motion. This tendency can be observed particularly for the power in the power-take-off systems and to a lesser extent for the velocity of the power-take-off systems. Further, the power in the spring-damper coupling during the push motion is higher than the one during the pull motion. This is due to the increased force in the power-take-off system during the push motion. Since the force

in the first three power-take-off systems is similar during the pull motion, the power in these power-take-off systems is determined by the velocity of the spring-damper coupling. It increases with decreasing resistance during the pull motion, which in turn is manifested in the power of the power-take-off system. On the other hand, the power in the fourth and the fifth power-take-off system depends mostly on the force applied in the power-take-off system during the pull motion.

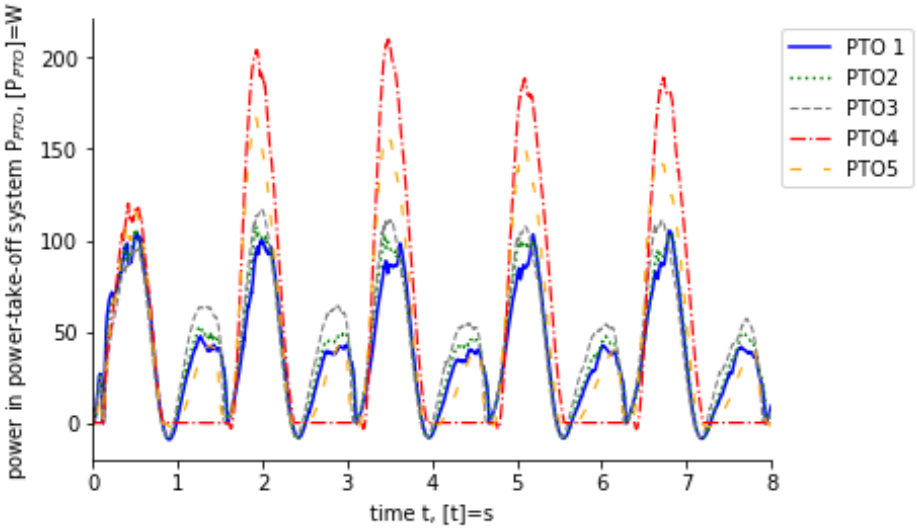

Figure 6.36 – Power in different power-take-off systems operating in waves with a wave height of $H = 0.2\,\mathrm{m}$ and a wavelength of $\lambda = 4\,\mathrm{m}$

The overall efficiency of the wave energy device equipped with different power-take-off systems is obtained with equation 5.25 and is depicted in figure 6.37. The efficiency indicates how much of the theoretical wave energy is converted during the first two wave energy conversion stages and can subsequently be transformed into electricity. The exact values can be derived from table 6.7.

All points considered, the wave energy conversion is the most efficient for the power-take-off system with the one-way braking as 76% of the theoretical wave energy is transformed into usable mechanical energy. The fifth power-take-off system which uses different resistance for the push and pull motion also achieves a high efficiency of 75%. Furthermore the power-take-off systems with the two-way braking which employ the same resistance during the push and pull motion attain sufficient efficiency in a range from approximately 60% to 70%. However, the efficiency of the wave energy converter increases the less resistance is applied during the pull motion. A maximal

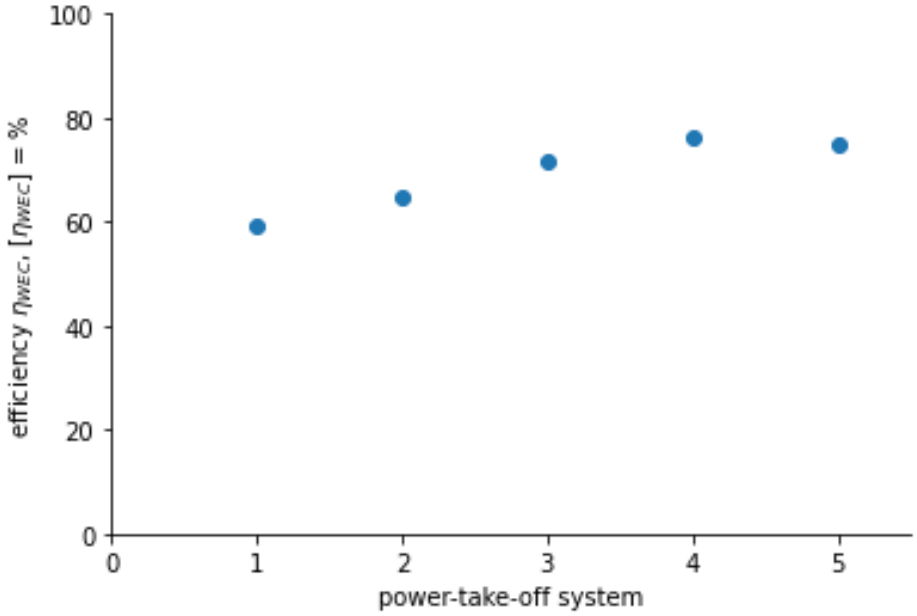

Figure 6.37 – Efficiency of different power-take-off systems operating in waves with a wave height of $H = 0.2\,\mathrm{m}$ and a wavelength of $\lambda = 4\,\mathrm{m}$

resistance during the push motion supports the increase of efficiency. This is confirmed by experiments conducted at the Danish Hydraulic Institute on behalf of Crestwing. [14]

6.8 Flow analysis of different power-take-off systems

Since the assembly of the power-take-off system influences the wave energy conversion and consequently determines the efficiency of the wave energy converter, it also impacts the behaviour of the waves. The effect of the assembly of the power-take-off system on the waves is investigated in this chapter. Thereby, the simulations of the first and the fourth power-take-off system from chapter 6.7 are compared because they achieve the worst and the best efficiency.

The wave energy converter equipped with the first power-take-off system leads to the wave field shown in figure 6.38, while the wave field in figure 6.39 results from the wave energy converter which employs the fourth power-take-off system. Therein, waves radiating from the wave energy converter can be identified, but there is no wake

downstream of the wave energy converter. This indicates that the simulation has not run long enough to develop a typical wave field. Nevertheless, a qualitatively satisfactory representation of the wave field resulting from the wave energy converter is obtained in figures 6.38 and 6.39, which further develops with longer simulation times.

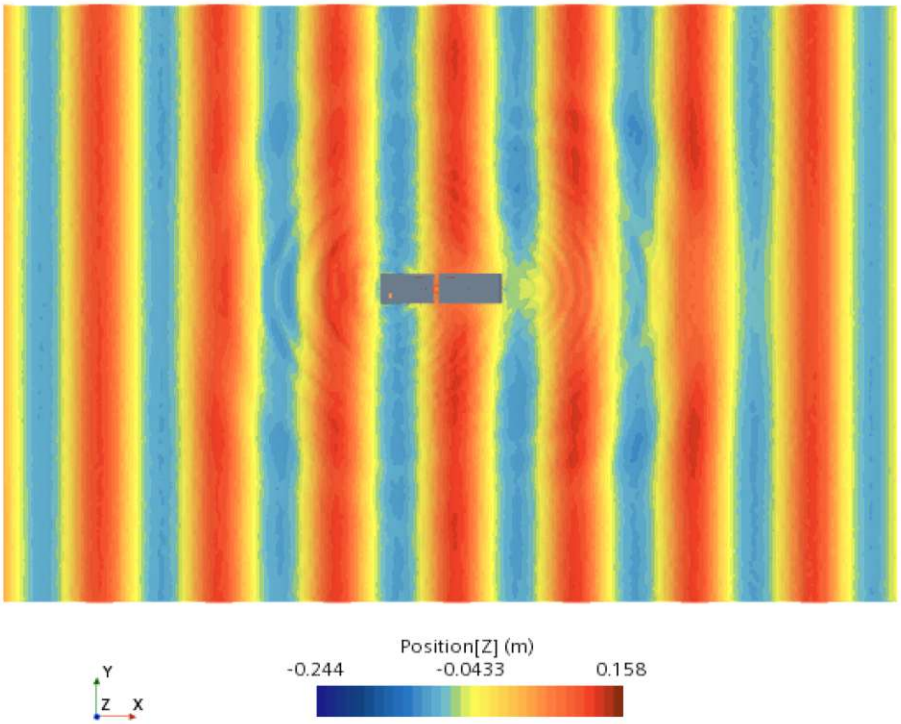

Figure 6.38 – Wave field resulting from the wave energy converter employed with the first power-take-off system operating in waves with a wave height of $H = 0.2\,\mathrm{m}$ and a wavelength of $\lambda = 4\,\mathrm{m}$

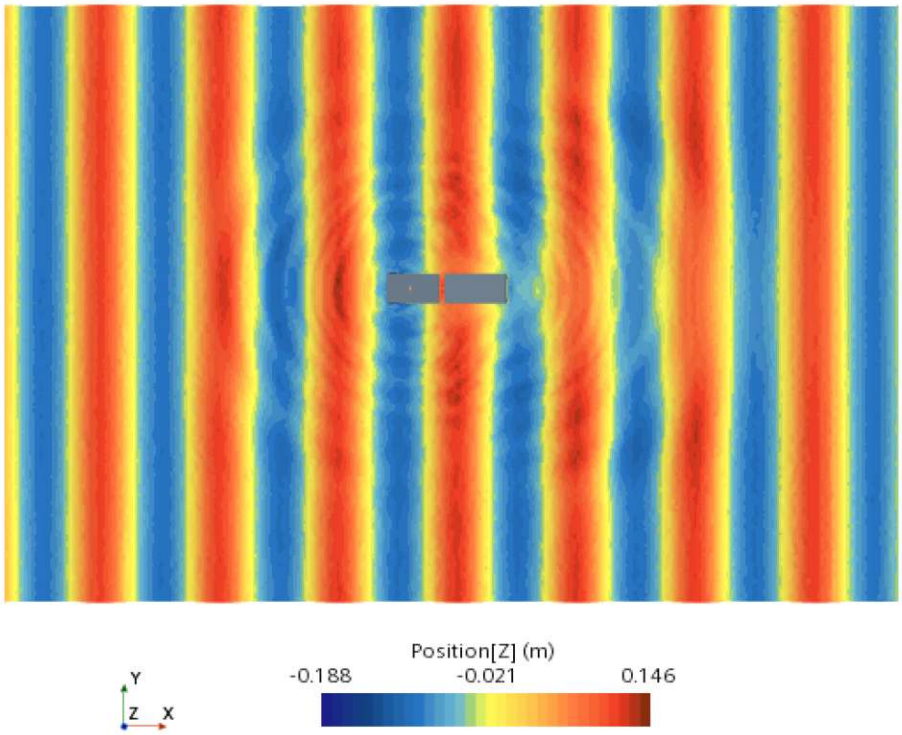

Figure 6.39 – Wave field resulting from the wave energy converter employed with the fourth power-take-off system operating in waves with a wave height of $H = 0.2\,\mathrm{m}$ and a wavelength of $\lambda = 4\,\mathrm{m}$

To verify the wave field, the surface elevation is measured at different locations in the wave tank. Figure 6.40 illustrates the wave elevation 9.1 m in front of the front pontoon of the wave energy converter. This ensures that the waves are fully developed and not influenced by the boundary conditions. Additionally, the waves are not yet impacted by the waves radiating from the device within the simulated time. This allows a comparison to the free surface elevation in equation 3.1 according to the linear wave theory. The surface elevation of the waves incident on the wave energy converter equipped with the first and the fourth power-take-off system are equal and remains almost consistent over the simulation time except for insignificant fluctuations. These can be attributed to numerical errors and are negligible. However, the simulated surface elevations deviate from the theoretical one. The wave crests are higher and the wave troughs are smaller but the simulated wave height corresponds to the theoretical one. Additionally, there is also a marginal phase shift, which is also observed within the simulated empty wave tank in chapter 6.2. Overall, the incident wave seems to be simulated sufficiently.

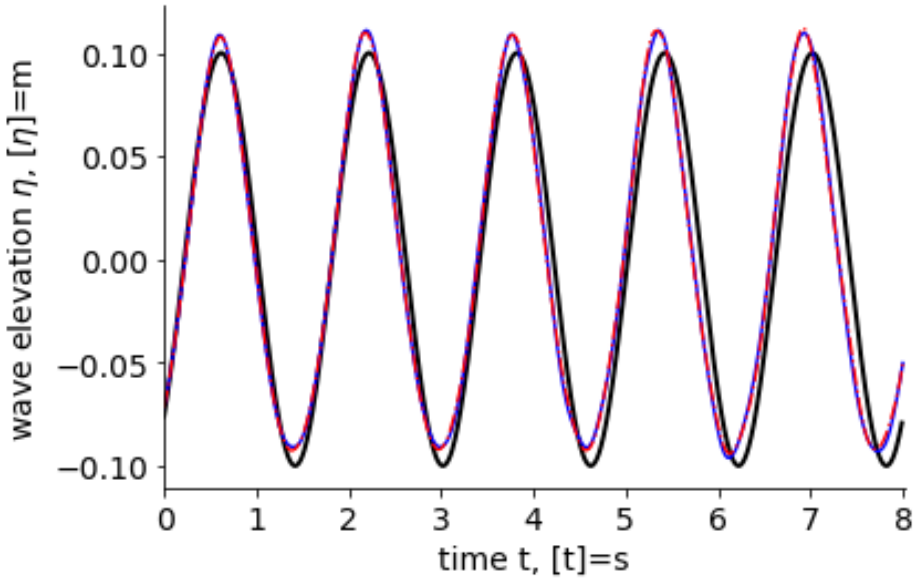

Figure 6.40 – Wave elevation η 9.1 m in front of the device according to linear wave theory (solid black), in the simulations with the wave energy converter employed with the first power-take-off system (solid blue) and with the fourth power-take-off system (dashed-dotted red)

Another point to consider is that the incident wave is affected by the radiated waves caused by the motion of the wave energy converter. The waves radiate in all directions and surround the device as shown in figure 6.38 and 6.39. Thereby, there is a superposition of the incident waves and the radiated waves. This may result in a change of the wave amplitude in front of the device, which in turn effects the energy contained in the waves incident on the device. However, these deviations are neglected and it is assumed that the wave energy incident on the wave energy converter corresponds to the one resulting from linear wave theory with the implemented wave height of $H = 0.2\,\mathrm{m}$. Furthermore, a decrease in the incident wave after the device is observed in figure 6.41, where the surface elevation is measured 0.1 m after the aft pontoon of the wave energy converter. The wave height after the wave energy converter is estimated by determining the maxima and minima of the measured wave elevation. The maxima and minima are then averaged and the wave height is the sum of the absolute values of the averaged maxima and minima of the wave elevation. The wave height after the wave energy converter equipped with the fourth power-take-off system is on average $H_{After} = 0.1494\,\mathrm{m}$. This is smaller than the one after the device with the first power-take-off system, which is $H_{After} = 0.1507\,\mathrm{m}$ on average. A smaller wave amplitude after the device indicates a decreased mean wave energy flux since the wave amplitude is

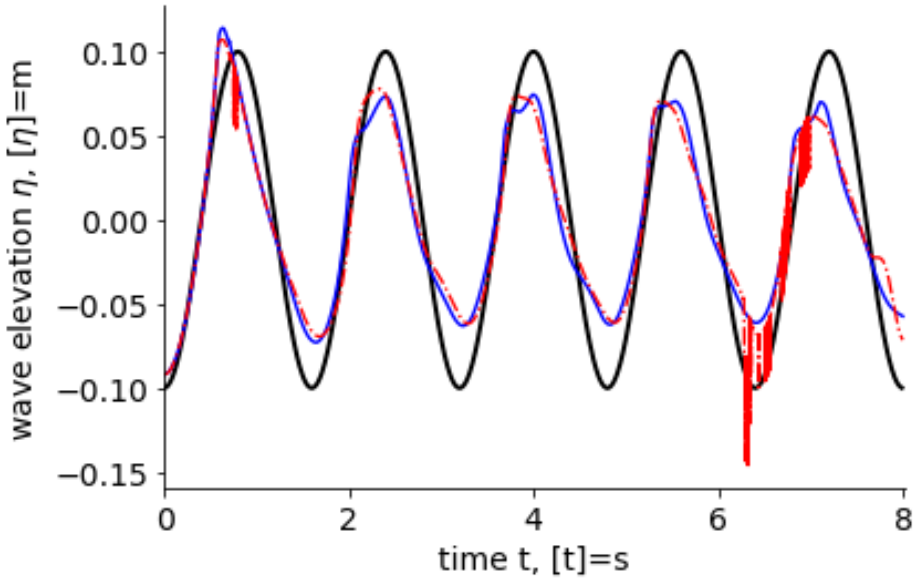

Figure 6.41 – Wave elevation η 0.1 m after the device according to linear wave theory (solid black), in the simulations with the wave energy converter employed with the first power-take-off system (solid blue) and with the fourth power-take-off system (dashed-dotted red)

proportional to the total mean energy density of a propagating wave according to equation 3.52. Thus, the mean wave energy flux after the wave energy converter is calculated following linear wave theory and is $E_{WavesAfter} = 243.55\,\text{J}$ for the wave energy converter with the first power-take-off system, while the mean wave energy flux after the one equipped with the fourth power-take-off system is $E_{WavesAfter} = 239.25\,\text{J}$. The difference between the theoretical mean wave energy flux before the wave energy converter of approximately 429.02 J and the obtained mean wave energy flux after the wave energy converter represents the wave energy harnessed during the first energy conversion stage. The total energy incident on the wave energy converter employing the first power-take-off system is $\Delta E = 185.48\,\text{J}$ and the one with the fourth power-take-off system is $\Delta E = 189.78\,\text{J}$. This implies that the smaller the wave amplitude behind the device, the more wave energy is absorbed. Therefore, the wave energy converter employing the fourth power-take-off system is more efficient than the wave energy converter with the first power-take-off system, which is also in agreement with the results from chapter 6.7.

Hence, the difference of the total mean wave energy flux before and after the device should correspond to the total energy incident on the wave energy converter in table 6.7. However, there are some deviations since the wave amplitude after the device is

determined by averaging the local maxima of the wave elevation after the device in figure 6.41. This leads to inaccuracies regarding the wave height, which in turn are reflected in the difference of the total mean wave energy flux before and after the wave energy converter. The deviations are amplified, as the averaging also considers initial conditions. The wave energy converter starts moving with the first incoming wave, which initiates the energy extraction. Thus, the wave amplitude at the beginning is rather high as less energy is extracted. However, a decrease of the wave amplitude over time is observed in figure 6.41 indicating a more efficient wave energy extraction. Furthermore, radiated waves caused by the motion of the wave energy converter additionally develop over time. Thus, the waves after the device are not only determined by the energy extraction but also by the superposition of the incident wave with the radiated waves. Another point to consider is that the waves tend to redevelop downstream, which was observed during the experiments at the Danish Hydraulic Institute. Since the surface elevation is measured 0.1 m after the edge of the aft pontoon and not directly behind the device, the waves are already enabled to regenerate partially. Nevertheless, the difference of the total mean wave energy flux before and after the device provides an approximation to the total energy incident on the wave energy converter, which is expected to improve for longer simulation times.

These considerations are also made for other power-take-off systems and the results are presented in the appendix A.2.4. Here the wave elevation 9.1 m before, 0.1 m downstream the device and 8.45 m after the device equipped with different power-take-off systems is also depicted.

In figure 6.41 some outliers can be observed at $t \approx 7\,\mathrm{s}$. These can be attributed to the motion of the device resulting in radiated waves and the wave energy converters' influence on the waves immediately after the device, which disturb the measurement of the wave elevation.

In the experiments at the Danish Hydraulic Institute, it was not only observed that the waves redevelop after the device, but also regenerate fully and resemble the incident waves. However, the wave will take some distance after the device to regenerate. This is also noted when considering the surface elevation 8.45 m after the aft pontoon in figure 6.42.

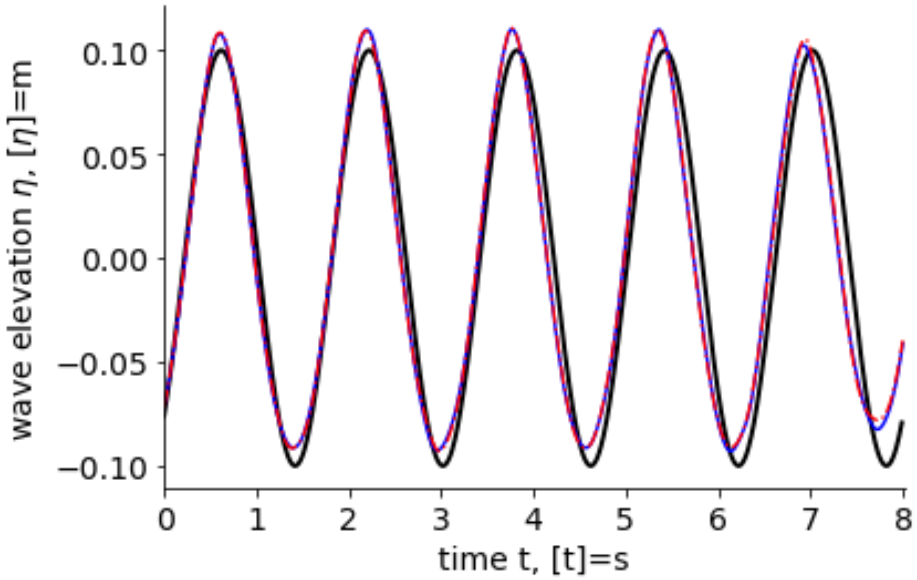

Figure 6.42 – Wave elevation η 8.45 m after the device according to linear wave theory (solid black), in the simulations with the wave energy converter employed with the first power-take-off system (solid blue) and with the fourth power-take-off system (dashed-dotted red)

7

Conclusion

Current advancements in the renewable energy sector of wave energy led to the development of the Crestwing wave energy converter which is a feasible technology. In this thesis, a CFD simulation of the Crestwing wave energy converter was set up to support the development of this technology as it can still be improved.

Waves according to the first and fifth order approximation of the Stokes theory were simulated in the empty wave tank. The wave generation was validated by comparing the simulated waves to waves according to linear wave theory and by determining the loss of the incident wave amplitude. The loss of the incident wave amplitude of the fifth order Stokes waves showed the same tendency as during a verification study in the reference [38]. Additionally, the wave profile of the fifth order Stokes waves showed minor deviations to the wave profile according to linear wave theory. Thereby, the fifth order Stokes waves were found to be the best approximation of linear wave theory and were used in further simulations.

In addition to the validation of the wave generation, a verification study of the mesh and the time step were performed with three different time steps and three different mesh sizes resulting in a fine, medium, and coarse mesh. Further, a qualitative study of the maximum limit of the CFL number was performed. Thereby, the medium mesh, the time step of 0.001 s and a maximum limit for the CFL number of 0.2 proved to be the best compromise between accuracy and computational effort and yielded reasonable simulations.

The working principle of the wave energy converter could be observed in an excerpt of the simulation. Further, the induced velocity field of the waves was investigated and was determined to be consistent with linear wave theory for deep water. The behaviour of the water surface around the device was studied and was found to influence the

pressure distribution on the bottom of the device.

Several simulations of the Crestwing wave energy converter operating in different wave conditions were conducted. Thereby, the energy exerted on the device as well as the energy in the power-take-off system were determined which allowed to define the efficiency of the first wave energy conversion stage and the overall efficiency based on the theoretical wave energy.

The efficiency of the first wave energy conversion stage refers to the energy exerted on the device. It is related to the pressure distribution on the bottom of the wave energy converter which in turn depends on the alignment of the wave energy converter with the waves. Therefore, the first energy conversion stage was most efficient, the more pressure was exerted on the device. This was the case when the wavelength resembled the length of the device, as the device could align perfectly with these waves. It was noticeable that the efficiency of the first wave energy conversion stage generally increased with an increasing wavelength at a constant wave height as long as the wavelength did not exceed the length of the wave energy converter but decreased again when the wavelength exceeded the length of the device. However, the efficiency of the first wave energy conversion stage did not increase steadily with an increasing wavelength for very small wave heights, but also achieved the highest efficiency for a wavelength similar to the length of the device.

This behaviour was reflected in both experiments and simulations in the energy in the power-take-off system. This is due to the fact that the absorbed wave energy was converted into useful mechanical energy by the power-take-off system within the second wave energy conversion stage. Since the energy in the power-take-off system is influenced by the motion of the wave energy converter, it was determined by the force and the velocity in the spring damper coupling. In addition to the hydrodynamic forces, other forces such as the force in the mooring system were taken into account. The resulting energy in the simulated power-take-off system was compared to the energy in the power-take-off system measured during experiments. Thereby, deviations occured which were also reflected in the corresponding power characteristics. These deviations were negligible for the wave energy converter operating in waves with long wavelengths and high wave heights but increased with a decreasing wave length at different wave heights. However, the simulated energy in the power-take-off system

provided a sufficient and reasonable qualitative representation of the experiments. In fact, the simulations modelled the working principle of the power-take-off system even better than experiments, as the force in the power-take-off system could be regulated more precisely.

Lastly, the overall efficiency of the wave energy converter is defined by the energy in the power-take-off system and was compared to experiments. The overall efficiency of the wave energy converter varied significantly depending on the wave condition in which the wave energy converter operated. The best efficiencies were achieved at wavelengths corresponding to the length of the device and the least efficiency was achieved for the shortest wave length and the highest wave height tested. This tendency was in agreement with experiments. However, there were quantitative deviations between simulations and experiments which were mainly attributed to the deviations in the energy in the power-take-off system and the neglected friction losses.

The wave field resulting from the wave energy converter operating in different wave conditions was studied. Thereby, the waves radiating from the wave energy converter were clearly visible and a wake was established during simulations with shorter wavelengths. This was due to the fact that more waves were incident on the wave energy converter during the simulated time period, which enabled the wake to develop. Additionally, the wave elevation before, immediately after and downstream of the device was determined and compared to linear wave theory. Generally, the wave elevation in front of the device resembles the incident wave elevation implying that the waves were not influenced by the radiated waves and the boundaries. However, the influence of the radiated waves increased the higher the simulated wave height and the shorter the wavelength. The wave height immediately after the device decreased significantly downstream of the device for all conducted simulations indicating a loss in wave energy. Thus, the difference between the wave energy before and after the device represents the energy exerted on the device. When comparing these variables, the difference between the wave energy before and after the device was generally greater than the energy exerted on the device. This was due to the fact that the difference between the wave energy before and after the device included all forces acting on the device, whereby the energy exerted on the device only considered hydrodynamic forces. Additionally, inaccuracies during the determination of the wave height occured. Further, the waves after the

device were influenced by the wake and the radiated waves from the device. Measuring the wave elevation downstream of the device showed that waves tend to rebuild and recover fully after some distance of the wave energy converter.

Since the power-take-off system determines the overall efficiency of the wave energy converter, it is considered as the key component of the wave energy converter and the development of an efficient power-take-off system is crucial. Thus, five applications of the power-take-off system were tested which differed in the intensity of the force in the spring damper coupling depending on the direction of its motion. The power-take-off system influenced the energy exerted on the device as an applied force in the spring damper coupling limited the relative movement of the two barges. Subsequently, the wave energy converter could not follow the waves accordingly and was subjected to less hydrodynamic forces. Thus, the energy exerted on the device increased, the less resistance was present in the power-take-off system during the pull motion reaching its maximum when no resistance was applied. This also applied to the energy in the power-take-off system, indicating the connection between the first and the second wave energy conversion stage. The behaviour of the energy in the power-take-off system resulted from the characteristics of the velocity and the force in the spring damper coupling. The velocity of the spring damper coupling increased with decreasing resistance during the pull motion, whereas the velocity of the spring damper coupling during the push motion was influenced by the resistance applied during the pull motion. The force in the spring damper coupling decreased with decreasing resistance during the pull motion and increased with increasing resistance during the push motion. Nevertheless, the force in the power-take-off system during the push motion was influenced by the resistance during the pull motion.

In conclusion, the highest overall efficiency of the wave energy converter was achieved when there was full resistance during the push motion and no resistance during the pull motion, whereas the least overall efficiency was obtained applying full resistance in both the pull and the push motion. Thus, the efficiency of the wave energy converter increased, the less resistance was applied during the pull motion and its increase was supported with a maximal resistance during the push motion. This was also in agreement with conducted experiments.

The wave fields resulting from the wave energy converter equipped with different power-

take-off systems were found to be qualitatively similar, as a typical wave field has not been able to develop after the simulated time of 8 s. Nevertheless, a difference in the wave fields could be identified when examining the wave elevation before, immediately after and downstream the device. The wave elevation before resembled the incident wave elevation and the wave elevation decreased immediately after the device but was rebuilt downstream the device. A decreased wave elevation immediately after the device indicates a decrease in wave energy, implying a better energy transfer on the wave energy converter. Therefore, the waves immediately after the most efficient wave energy converter were smaller than the waves immediately after the least efficient wave energy converter.

In summary, the simulation provided sufficient and accurate results which also corresponded to experiments conducted. The simulations confirmed that the wave energy converter achieved the highest efficiencies when operating in waves with a wave length similar to the length of the device. Further, the employment of an efficient power-take-off system increased the efficiency. The power-take-off system distinguished between the intensity of the force in the power-take-off system during the pull and push motion. Thereby, the most efficient power-take-off system applied full resistance during the push and no resistance during the pull motion.

8

Outlook

In this thesis, a first attempt is made to set up a viable CFD simulation of the Crestwing wave energy converter. The results are satisfactory, but the simulations can still be optimized.

First of all, the setup of the simulation can be improved. The symmetry of the device should be used by employing symmetry planes. Therefore, the extent of the computational domain and consequently the number of cells, and the required simulation time are reduced. In longer-lasting simulations, a reflection of surface waves at the boundaries occurs, which can be eliminated by implementing the VOF wave forcing. This also allows to reduce the size of the computational domain and thus the computational effort without degrading the accuracy and reliability of the solution. [57]

Secondly, the quasi-stationary, elastic catenary coupling used in simulations does not correspond to the mooring system used in experiments. Further, the characteristics of the quasi-stationary, elastic catenary coupling are only approximated and adjusted to a certain wave height. Therefore, simulations with a greater wave height of $H > 0.25\,\mathrm{m}$ malfunction because the mooring system fails. Hence, an implementation of an improved mooring system is suggested.

Thirdly, the wave energy converter is equipped with a shield preventing waves to slosh on top of the device during the experiments at the Danish Hydraulic Institute. Additionally, a skirt on the sides and the aft edge are mounted on the wave energy converter during experiments. [8] The influence of these additional components could be further investigated with CFD simulation.

Lastly, a simulation of several wave energy converters installed side by side provides an idea of a wave energy park. Thus, the influence of many wave energy converters on the waves as well as the influence of the wave energy converters on each other can

be investigated and the efficiency of each wave energy converter operating in the wave energy park can be determined. Thereby, the distance between the devices can be varied. This allows designing a highly efficient wave energy park.

Bibliography

[1] *Guide to wave analysis and forecasting*. World meteorological organization, 1998.

[2] T. Aderinto and H. Li. Review on power perfromance and efficiency of wave energy converters. *Energies*, 12(22):4329, 2019.

[3] R. Ahamed, K. McKee, and I. Howard. Advancements of wave energy converters based on power take off (PTO) systems: A review. *Ocean Engineering*, 204:107248, 2020.

[4] Petros J. Axaopoulos and Georgios T. Tzanes. Wind Energy Potential (Measurements, Evaluation, Forecasting). *Elsevier*, 2022.

[5] Ph. Balitsky. *A numerical investigation of the array effects of wave energy converters with a realistic power-take-off system utilizing a coupled model suite*. PhD thesis, Ghent University, 2019.

[6] H. B. Bingham, D. Ducasse, K. Nielsen, and R. Read. Hydrodynamic analysis of oscillating water column wave energy devices. *Journal of Ocean Engineering and Marine Energy*, 1(4):405–419, 2015.

[7] A. B. Biran. *Ship hydrostatics and stability*. Elsevier Inc., 2003.

[8] J. Bjarne. Crestwing wave energy converter - 3D wave tank model tests. Technical report, Danish Hydraulic Institute, 2011.

[9] P. Bocotti. *Wave mechanics and wave loads on marine structures*. Elsevier Inc., 2015.

[10] A. Böge and W. Böge. *Technische Mechanik: Statik - Reibung - Dynamik - Festigkeitslehre - Fluidmechanik*. Springer Fachmedien Wiesbaden GmbH, 2019.

[11] SciPy community. SciPy documentation, July 2022. URL https://docs.scipy.org/doc/.

[12] G. D. Crapper. *Introduction to water waves*. Ellis Horwood [u.a.], 1984.

[13] Crestwing. Oceans of wave energy - Technology. URL https://www.crestwing.dk/english-2/.

[14] Crestwing. Assessment of Crestwing - Prototype and PTO-system - Based on data from measurements. Technical report, Crestwing Ltd. and Tordenskiold Offshore and Tank tests, 2021.

[15] E. Dick. *Fundamentals of turbomachines - Fluid mechanics and its applications*. Springer Nature Switzerland AG, 2022.

[16] B. Drew, A. R. Plummer, and M. N. Sahinkaya. A review of wave energy converter technology. *Proceedings of the Institution of Mechanical Engineers, Part A: Journal of Power and Energy*, 223(8):887–902, 2009.

[17] F. Durst. *Grundlagen der Strömungsmechanik - Eine Einführung in die Theorie der Strömungen von Fluiden*. Springer Verlag Berlin Heidelberg, 2006.

[18] Environmental and Energy Study Institute (EESI). Fossil Fuels. URL https://www.eesi.org/topics/fossil-fuels/description.

[19] İ. Ö. Erselcan and A. Kükner. A review of Power Take-Off Systems employed in wave energy converters. *Journal of Naval Science and Engineering*, 10(1):32–44, 2014.

[20] J. Falnes and A. Kurniawan. *Ocean waves and oscillating systems: Linear interactions including wave-energy extraction*. Cambridge University Press, 2020.

[21] J. D. Fenton. Fifth order Stokes theory for steady waves. *Journal of Waterway, Port, Coastal and Ocean Engineering*, 111(2):216–234, 1985.

[22] M. Folley. *Numerical modelling of wave energy converters - State-of-the-art techniques for single devices and arrays*. Elsevier Inc., 2016.

[23] G. Giannini, I. Temiz, P. Rosa-Santos, Z. Shahroozi, V. Ramos, M. Göteman, J. Engström, S. Day, and F. Taveiro-Pinto. Wave energy converter power take-off system scaling and physical modelling. *Journal of Marine Science and Engineering*, 8(9):632, 2020.

[24] C.R. Handoko and Mukhtasor. The development of power take-off technology in wave energy converter systems: A review. *IOP Conference Series: Earth and Environmental Science*, 739(1):012081, 2021.

[25] T. Hino, F. Stern, L. Larsson, M. Visonneau, N. Hirata, and J. Kim. *Numerical ship hydrodynamics - An assessment of the Tokyo 2015 workshop*. Springer Nature Switzerland AG, 2021.

[26] IEA. World's first comprehensive energy roadmap shows government actions to rapidly boost clean energy and reduce fossil fuel use can create millions of jobs, lift economic growth and keep net zero in reach. URL https://www.iea.org/news/pathway-to-critical-and-formidable-goal-of-net-zero-emissions-by-2050-is-narrow-but-brings-huge-benefits.

[27] IPCC. *Climate Change 2022: Impacts, Adaptation and Vulnerability. Contribution of Working Group II to the Sixth Assessment Report of the Intergovernmental Panel on Climate Change*. Cambridge University Press, 2022.

[28] Md. R. Islam, N. K. Roy, and S. Rahman. *Renewable energy and the environment*. Springer Nature Singapore Pte Ltd., 2018.

[29] J. W. Kamphuis. *Introduction to coastal engineering and management*. World Scientific Publishing Co., 2000.

[30] H. Karadeniz, M. P. Saka, and V. Togan. *Stochastic analysis of offshore steel structures - An analytical appraisal*. Springer Verlag London, 2013.

[31] M. Karimirad. *Offshore energy structures - For wind power, wave energy and hybrid marine platforms*. Springer International Publishing Switzerland, 2014.

[32] G. Kuo. When fossil fuels run out, what then? URL https://mahb.stanford.edu/library-item/fossil-fuels-run/.

[33] P. H. Le Blond and L. A. Mysak. *Waves in the ocean*. Elsevier Scientific Publishing Company, 1978.

[34] B. Le Méhauté. *An introduction to hydrodynamics and water waves*. Springer Verlag, 1976.

[35] C. M. Liu, H. H. Hwung, and R. Y. Yang. The consistence between the Stokes wave theory and general wave theory. *Journal of Mechanics*, 25(3):N17–N20, 2009.

[36] St. R. Massel. *Ocean surface waves - Their physics and prediction*. World Scientific Publishing Co. Pte. Ltd., 2018.

[37] M. E. McCormick. *Ocean Engineering Wave Mechanics*. John Wiley and Sons, 1973.

[38] H. Mikkelsen, Y. Shao, and J. H. Walter. CFD Verification and Validation of Added Resistance and Seakeeping Response in Regular Oblique Waves with varying wave length. *The 9th Conference on Computational Methods in Marine Engineering (Marine 2021)*, 2021.

[39] I. Moukhtar, A. Z. El Dein, A. A. Elbaset, and M. Yasunori. *Solar energy - Ttechnologies, design, modeling and economics*. Springer Nature Switzerland AG, 2021.

[40] W. H. Munk. Origin and generation of waves. *Coastal Engineering Proceedings*, 1950. URL https://journals.tdl.org/icce/index.php/icce/article/view/904.

[41] J. N. Newman. *Marine Hydrodynamics*. The MIT Press, 2017.

[42] H. P. Nguyen, C. M. Wang, Z. Y. Tay, and V. H. Luong. Wave energy converter and large floating platform integration: A review. *Ocean Engineering*, 213:107768, 2020.

[43] H. Oertel Jr. *Prandtl - Führer durch die Strömungslehre - Grundlagen und Phänomene*. Springer Fachmedien Wiesbaden GmbH, 2017.

[44] H. Oertel Jr., M. Böhle, and U. Dohrmann. *Strömungsmechanik - Grundlagen - Grundgleichungen - Lösungsmethoden - Softwarebeispiele*. Vieweg + Teubner, 2009.

[45] A. Pecher and Kofoed J.P. *Ocean engineering and oceanography - Handbook of ocean wave energy*. Springer International Publishing AG Switzerland, 2017.

[46] St. B. Pope. *Turbulent flows*. Cambridge University Press, 2006.

[47] S. Raghunathan. The wells air turbine for wave energy conversion. *Progress in Aerospace Sciences*, 31(4):335–386, 1995.

[48] J. C. Rotta. *Turbulente Strömungen - Eine Einführung in die Theorie und ihre Anwendungen*. B.G. Teubner Stuttgart, 1972.

[49] G. Sannino, A. Carillo, A. Vogler, G. Bracco, M. Giuliana, V. Diego, P. Contestabile, D. P. Coiro, G. Troise, L. Castellini, and J. V. Ringwood. *Renewable energy from the oceans*, chapter Wave energy, pages 19–93. Institution of Engineering and Technology, 2019.

[50] T. Sawaragi. *Coastal engineering - Waves, beaches, wave-structure interaction*. Elsevier, 1995.

[51] H. Schlichting and K. Gersten. *Grenzschichttheorie*. Springer Verlag Berlin Heidelberg, 2006.

[52] L. W. Schwartz. Computer extension and analytic continuation of Stokes' expansion for gravity waves. *Journal of Fluid Mechanics*, 62:553–578, 1974.

[53] R. Schwarze. *CFD-Modellierung - Gundlagen und Anwendungen bei Strömungsprozessen*. Springer Verlag Berlin Heidelberg, 2013.

[54] I. T. Selezov, Y. G. Kryvonos, and I. S. Gandzha. *Wave propagation and diffraction - Mathematical methods and applications*. Springer Nature Singapore Pte Ltd., 2018.

[55] A. S. Shehata, Q. Xiao, K. M. Saqr, and D. Alexander. Wells turbine for wave energy conversion: a review. *International Journal of Energy Research*, 41(1):6–38, 2017.

[56] W. Sheng. Wave energy conversion and hydrodynamics modelling technologies: A review. *Renewable and Sustainable Energy Reviews*, 109:482–498, 2019.

[57] Siemens. *Simcenter Star-CCM+ user guide, version 2021.3*, 2021.

[58] R. M. Sorensen. *Basic wave mechanics for coastal and ocean engineers*. John Wiley and Sons, Inc., 1993.

[59] J. H. Spurk and N. Aksel. *Fluid mechanics*. Springer Nature Switzerland AG, 2020.

[60] Statista. Verteilung der CO2-Emissionen weltweit nach Sektor bis 2020. URL https://www.crestwing.dk/english-2/.

[61] R. Stöllinger. The EU's most urgent industrial mission: Zero imports of fossil fuels, 2022. URL https://wiiw.ac.at/the-eu-s-most-urgent-industrial-mission-zero-imports-of-fossil-energy-n-547.html.

[62] J. Tao. *Numerical simulation of water waves*. Springer Nature Singapore Pte Ltd., 2020.

[63] L. F. Titov. *Wind-driven waves*. Israel Program for Scientific Translations, 1971.

[64] D. C. Wilcox. *Turbulence modeling for CFD*. DCW Industries, 1994.

[65] I. R. Young. *Wind generated ocean waves*. Elsevier Science Ltd, 1999.

[66] Y. Zhang, Y. Zhao, W. Sun, and J. Li. Ocean wave energy converters: Technical principle, device realization and performance evaluation. *Renewable and Sustainable Energy Reviews*, 141:110764, 2021.

[67] H.-J. Zhao, Z.-Y. Song, L. Li, J. Kong, L.-Q. Wang, and J. Yang. On the fifth-order Stokes solution for steady water waves. *China Ocean Engineering*, 30(5):794–810, 2016.

A

Appendix

A.1 Different wave conditions

A.1.1 Velocity in the wave tank

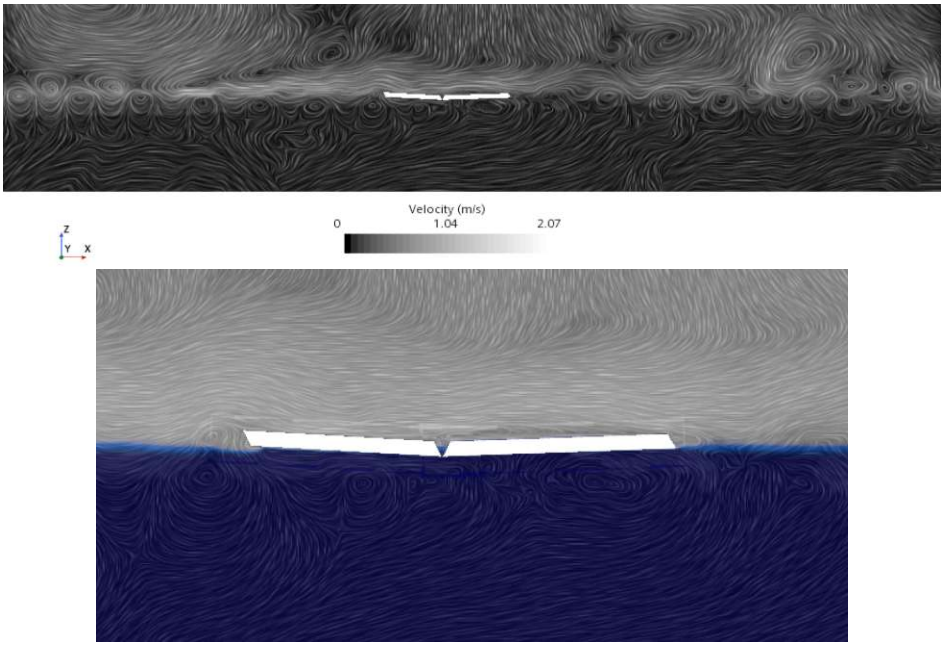

Figure A.1 – Velocity in the wave tank with waves of a wave height of $H = 0.25\,\mathrm{m}$ and a wavelength of $\lambda = 1.9\,\mathrm{m}$: (a) whole domain, (b) detail

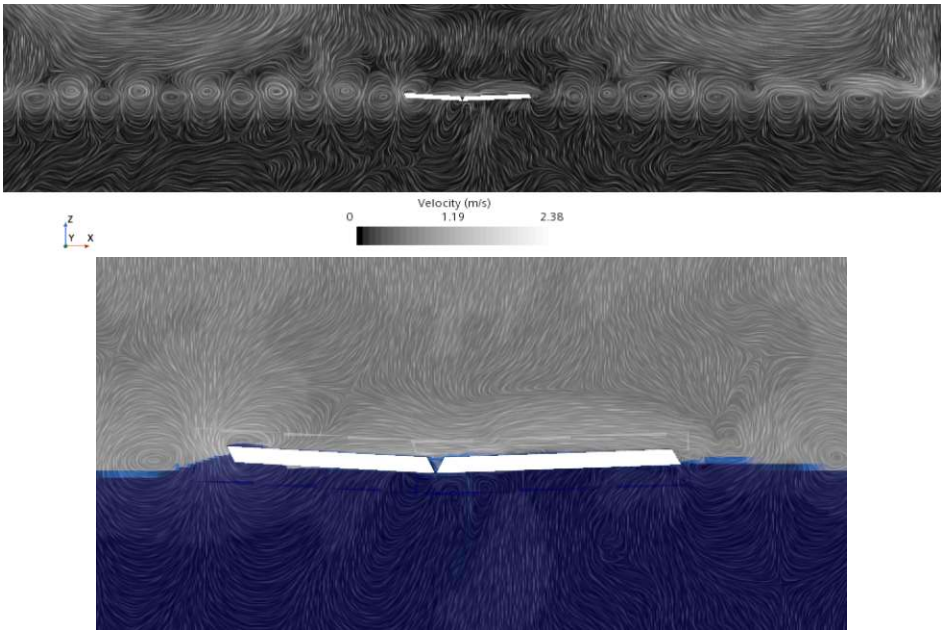

Figure A.2 – Velocity in the wave tank with waves of a wave height of $H = 0.25\,\mathrm{m}$ and a wavelength of $\lambda = 2.2\,\mathrm{m}$: (a) whole domain, (b) detail

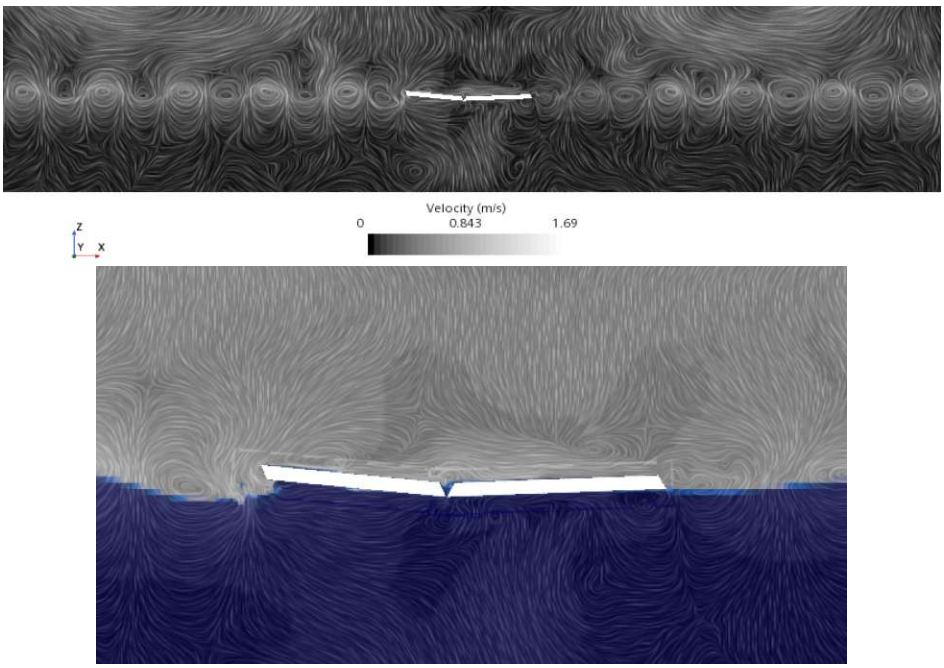

Figure A.3 – Velocity in the wave tank with waves of a wave height of $H = 0.25\,\mathrm{m}$ and a wavelength of $\lambda = 2.6\,\mathrm{m}$: (a) whole domain, (b) detail

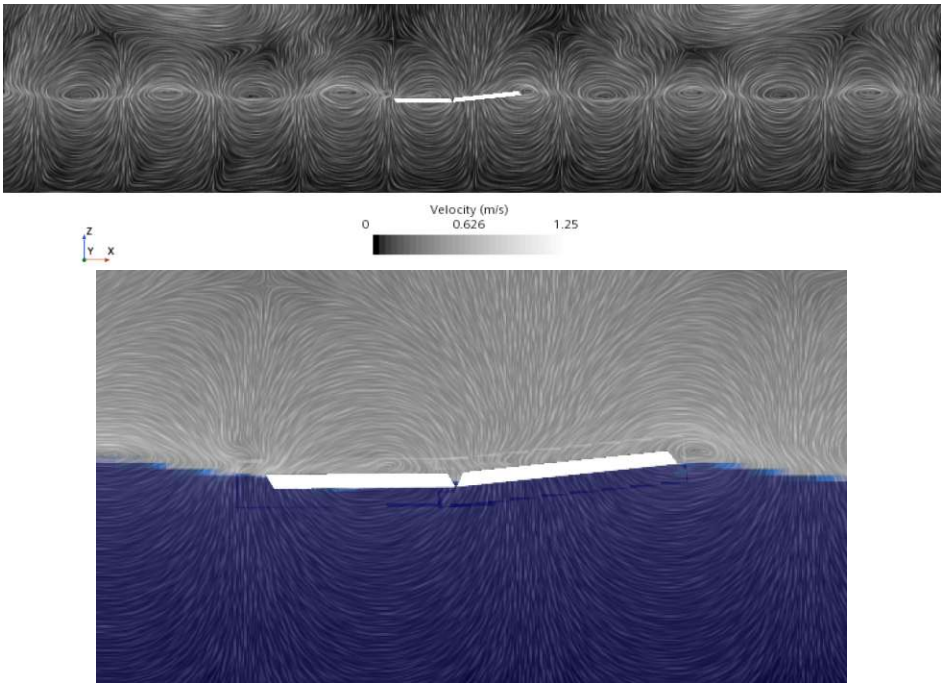

Figure A.4 – Velocity in the wave tank with waves of a wave height of $H = 0.25\,\mathrm{m}$ and a wavelength of $\lambda = 5.6\,\mathrm{m}$: (a) whole domain, (b) detail

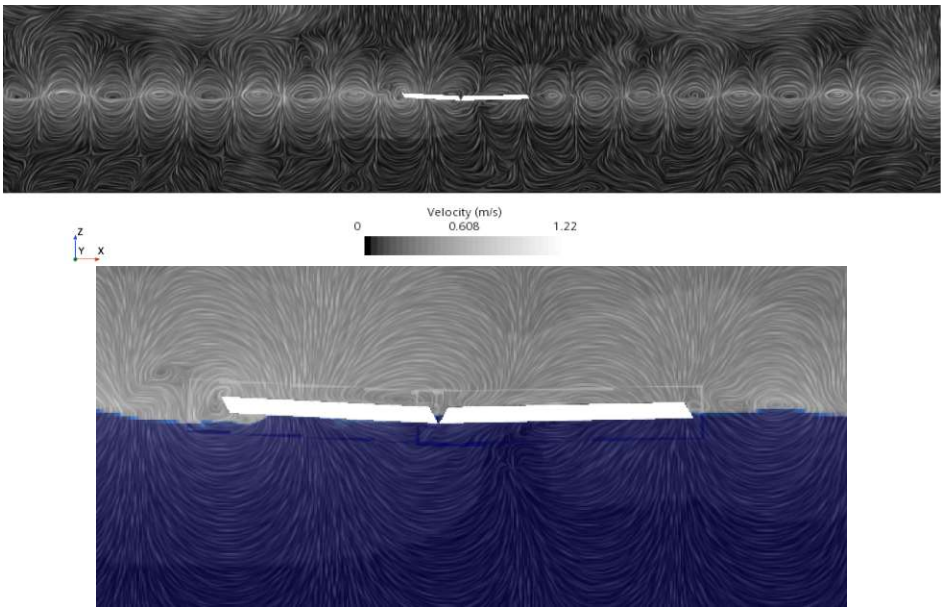

Figure A.5 – Velocity in the wave tank with waves of a wave height of $H = 0.2\,\mathrm{m}$ and a wavelength of $\lambda = 3.1\,\mathrm{m}$: (a) whole domain, (b) detail

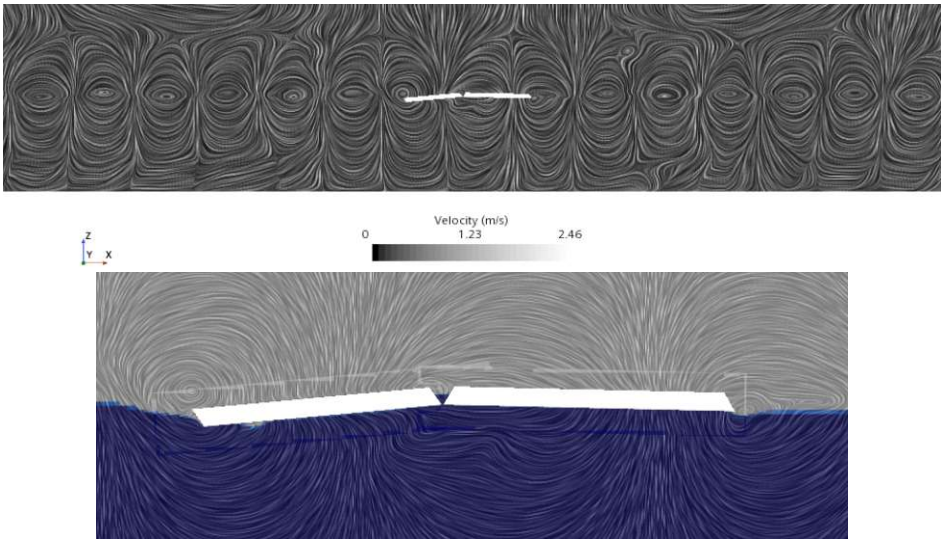

Figure A.6 – Velocity in the wave tank with waves of a wave height of $H = 0.2\,\mathrm{m}$ and a wavelength of $\lambda = 4\,\mathrm{m}$: (a) whole domain, (b) detail

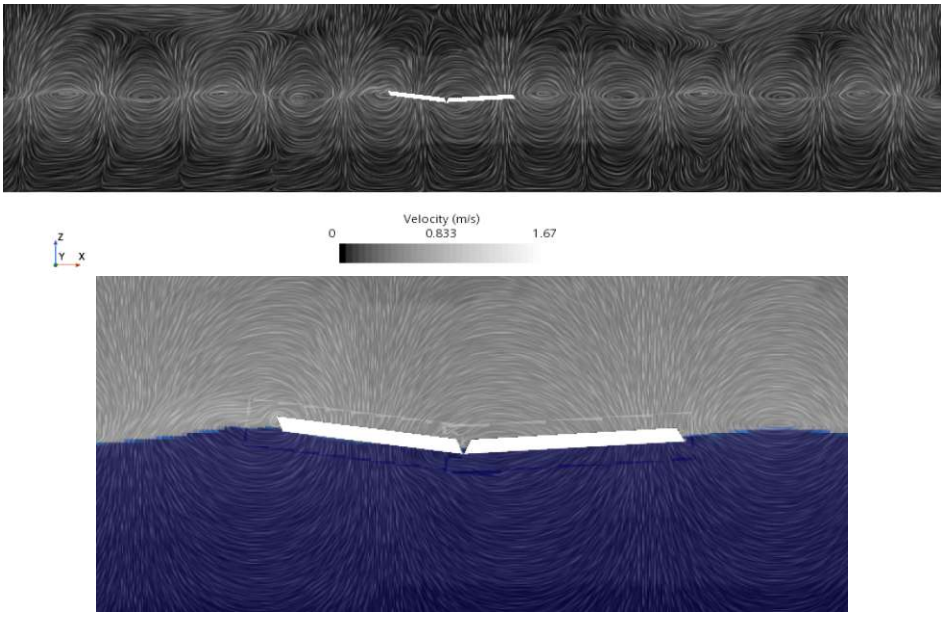

Figure A.7 – Velocity in the wave tank with waves of a wave height of $H = 0.2\,\mathrm{m}$ and a wavelength of $\lambda = 5.1\,\mathrm{m}$: (a) whole domain, (b) detail

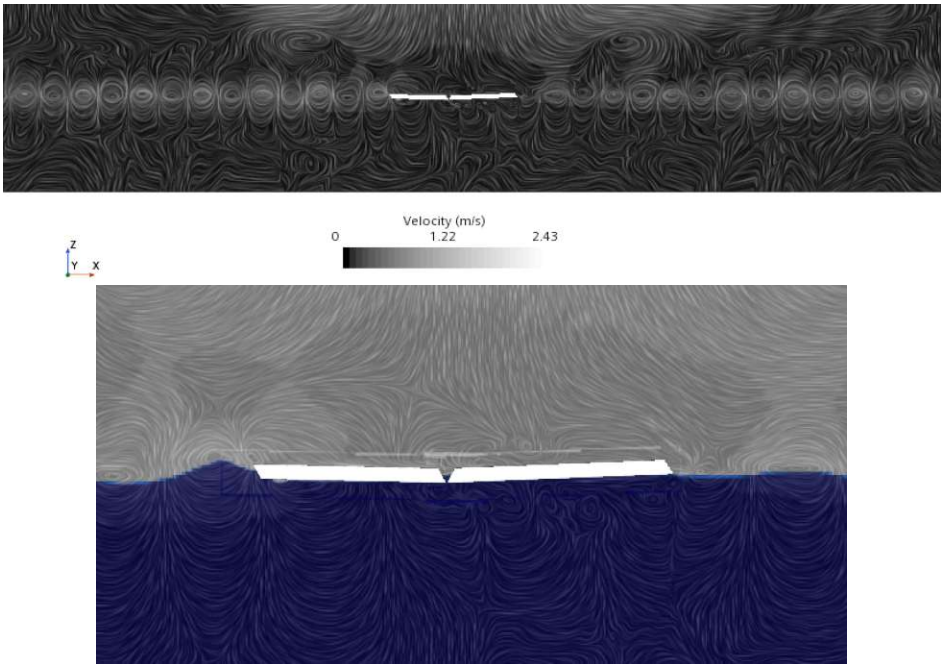

Figure A.8 – Velocity in the wave tank with waves of a wave height of $H = 0.15\,\mathrm{m}$ and a wavelength of $\lambda = 1.9\,\mathrm{m}$: (a) whole domain, (b) detail

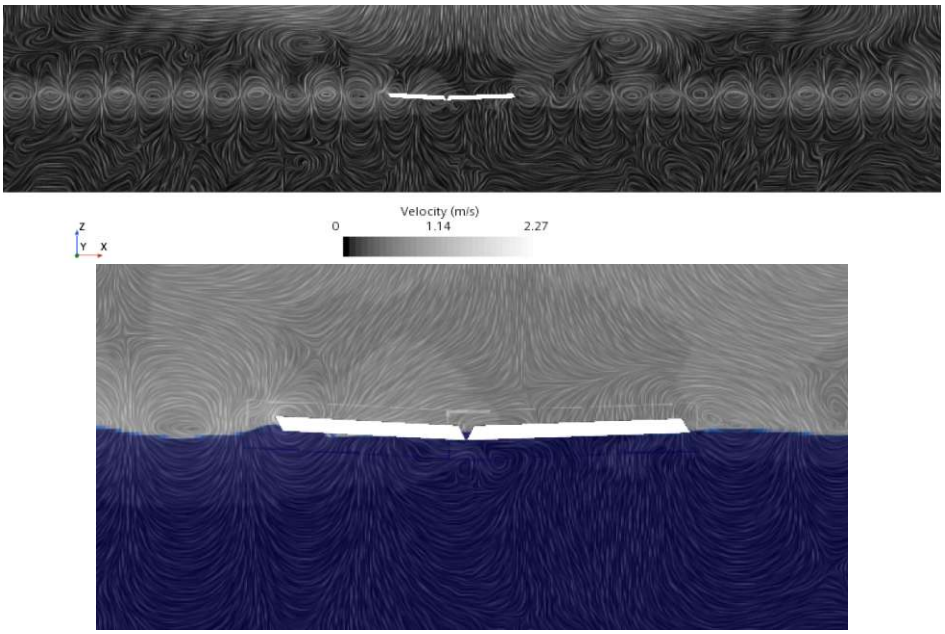

Figure A.9 – Velocity in the wave tank with waves of a wave height of $H = 0.15\,\mathrm{m}$ and a wavelength of $\lambda = 2.2\,\mathrm{m}$: (a) whole domain, (b) detail

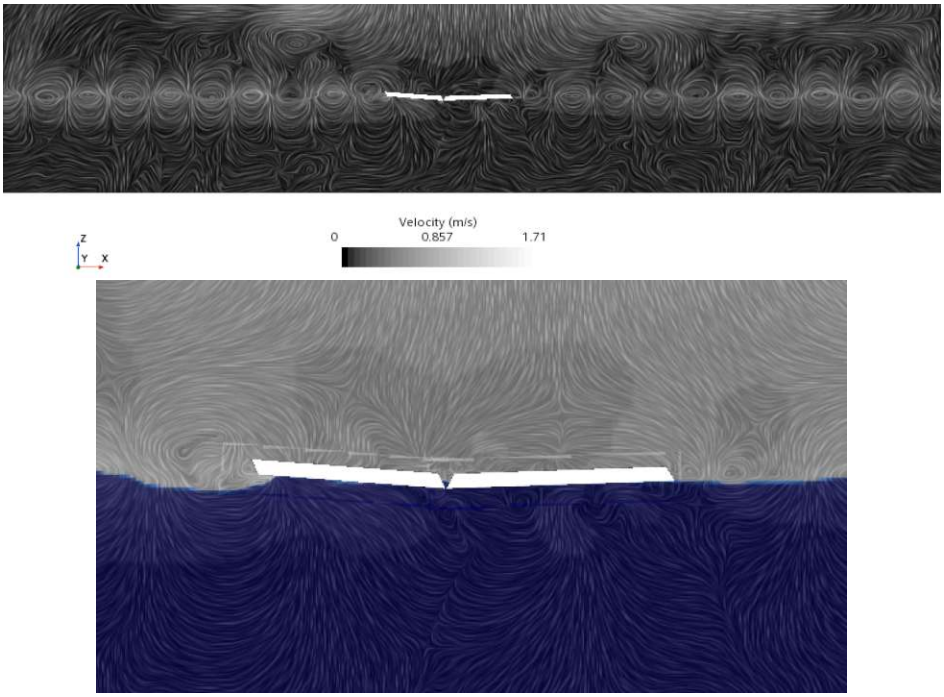

Figure A.10 – Velocity in the wave tank with waves of a wave height of $H = 0.15\,\mathrm{m}$ and a wavelength of $\lambda = 2.6\,\mathrm{m}$: (a) whole domain, (b) detail

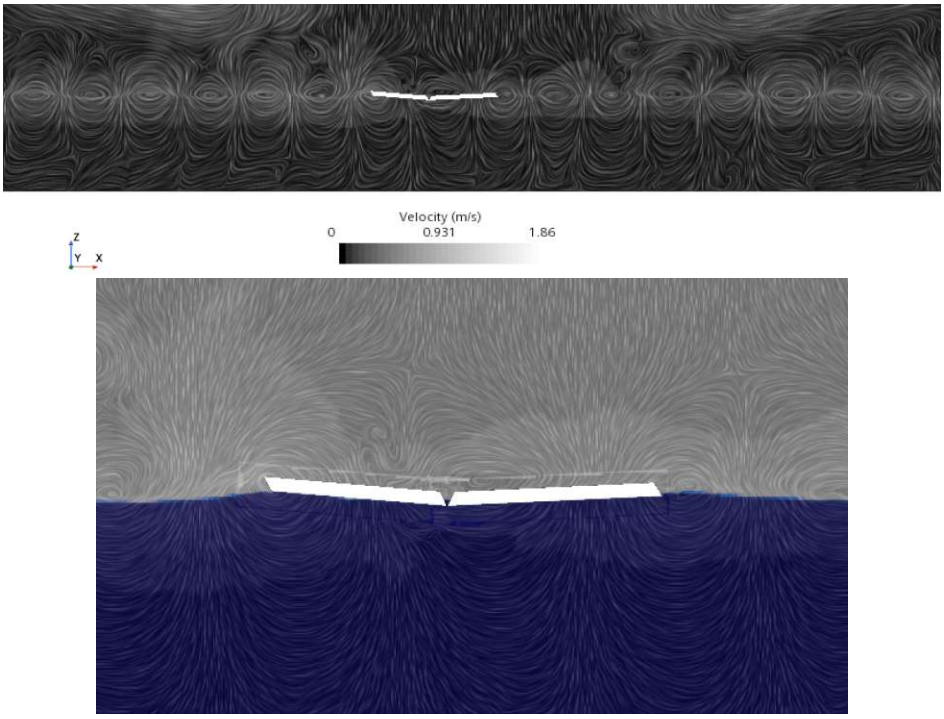

Figure A.11 – Velocity in the wave tank with waves of a wave height of $H = 0.125\,\mathrm{m}$ and a wavelength of $\lambda = 3.7\,\mathrm{m}$: (a) whole domain, (b) detail

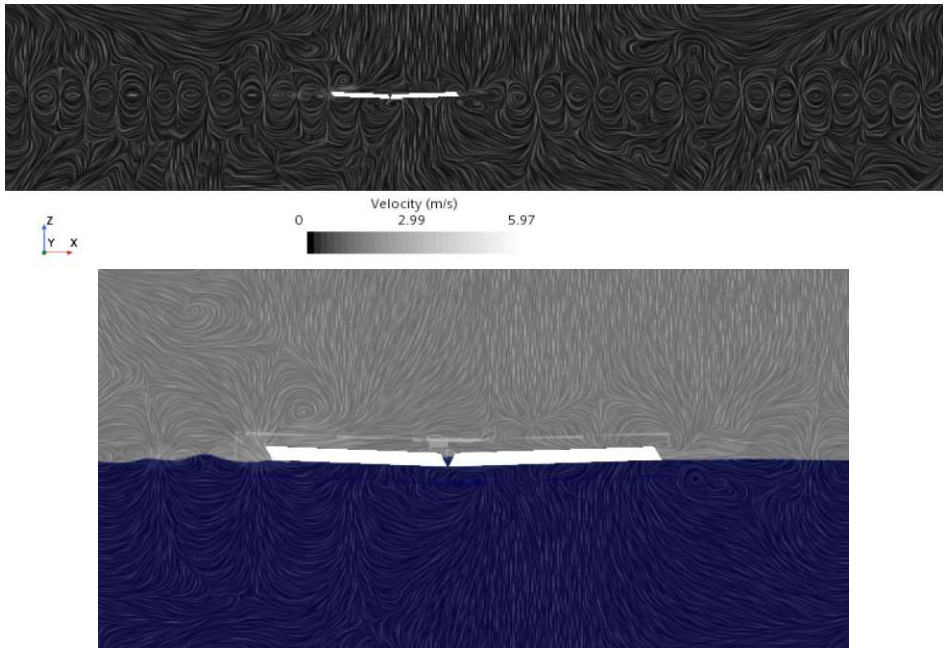

Figure A.12 – Velocity in the wave tank with waves of a wave height of $H = 0.05\,\mathrm{m}$ and a wavelength of $\lambda = 1.9\,\mathrm{m}$: (a) whole domain, (b) detail

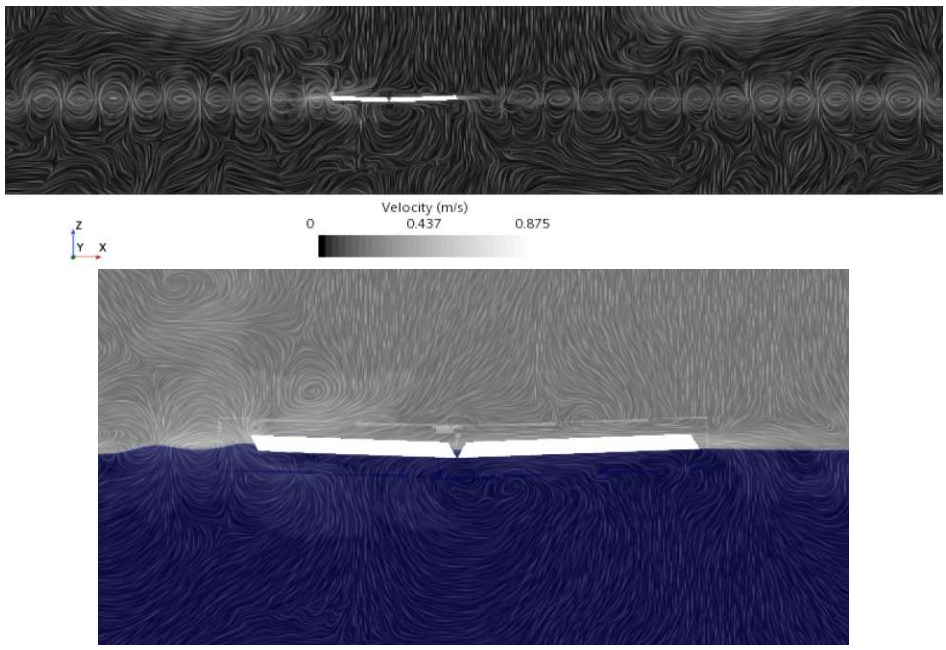

Figure A.13 – Velocity in the wave tank with waves of a wave height of $H = 0.05\,\mathrm{m}$ and a wavelength of $\lambda = 2.2\,\mathrm{m}$: (a) whole domain, (b) detail

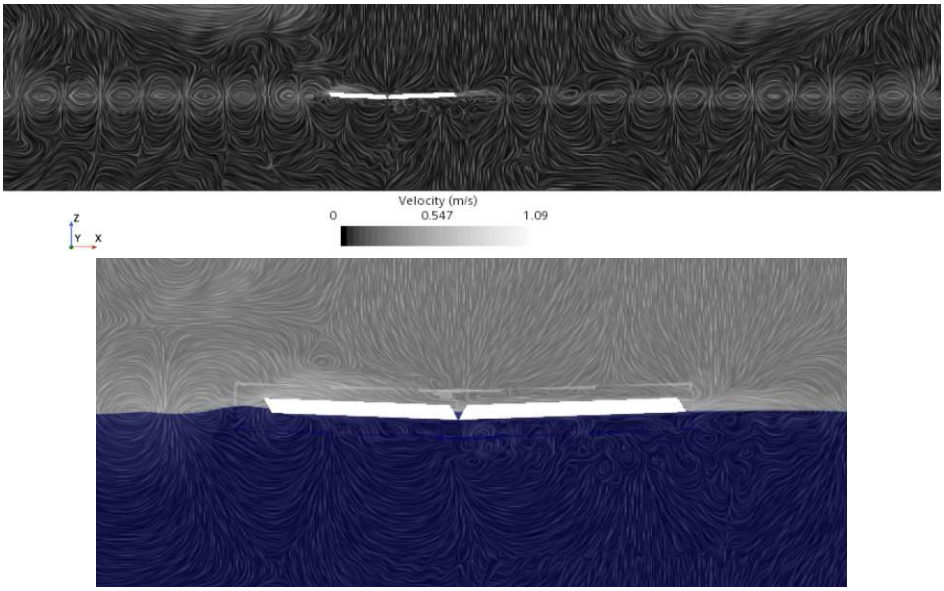

Figure A.14 – Velocity in the wave tank with waves of a wave height of $H = 0.05\,\mathrm{m}$ and a wavelength of $\lambda = 2.6\,\mathrm{m}$: (a) whole domain, (b) detail

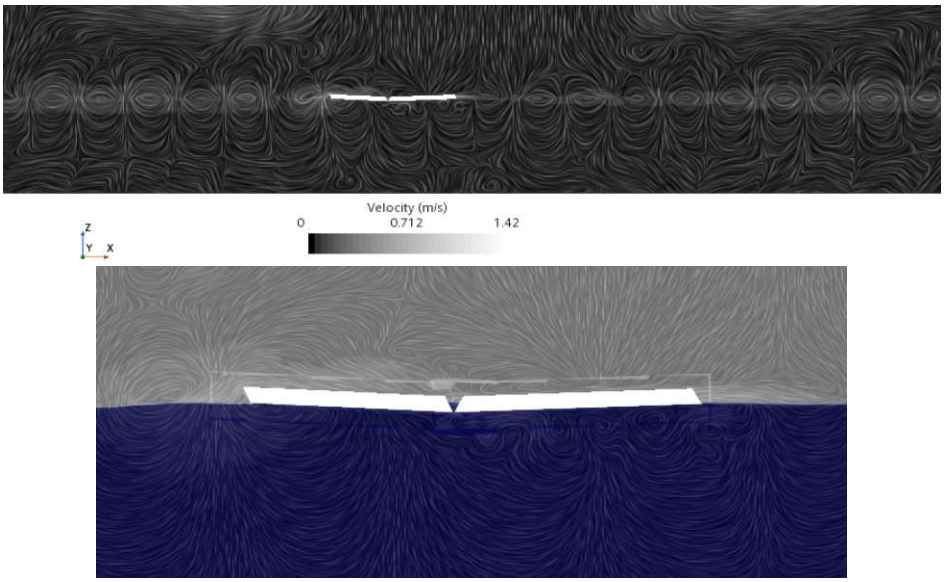

Figure A.15 – Velocity in the wave tank with waves of a wave height of $H = 0.05\,\mathrm{m}$ and a wavelength of $\lambda = 3.1\,\mathrm{m}$: (a) whole domain, (b) detail

A.2 Different power-take-off systems

A.2.1 Wave fields

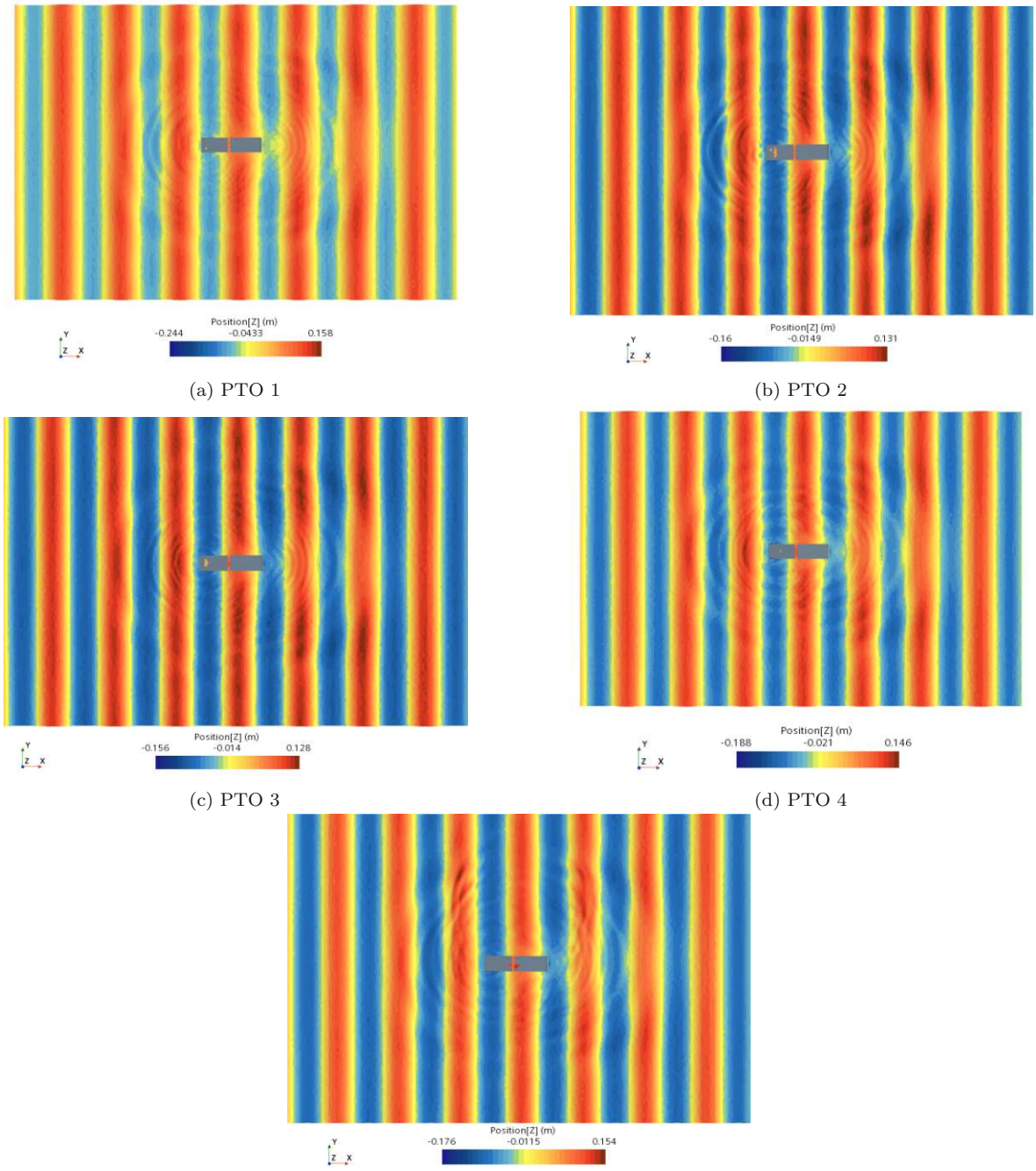

(a) PTO 1

(b) PTO 2

(c) PTO 3

(d) PTO 4

(e) PTO 5

Figure A.16 – Wave fields resulting from the wave energy converter equipped with different power-take-off systems operating in waves of a wave height of $H = 0.20\,\mathrm{m}$ at a wavelength of $\lambda = 4\,\mathrm{m}$ at $t = 8s$

A.2.2 Velocity in the wave tank

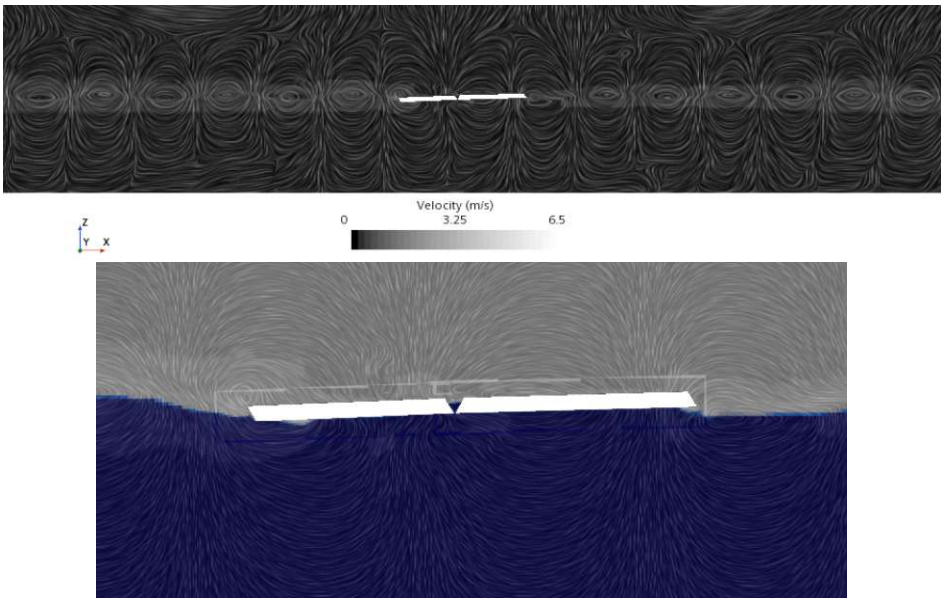

Figure A.17 – Velocity in the wave tank with waves of a wave height of $H = 0.2\,\mathrm{m}$ and a wavelength of $\lambda = 4\,\mathrm{m}$ and the wave energy converter equipped with the first power-take-off system: (a) whole domain, (b) detail

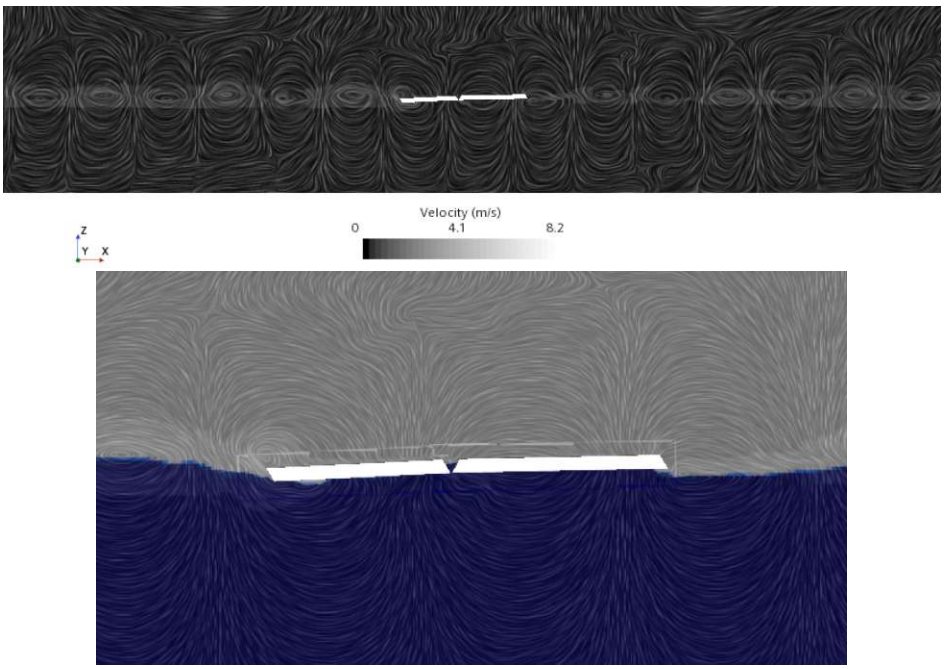

Figure A.18 – Velocity in the wave tank with waves of a wave height of $H = 0.2\,\mathrm{m}$ and a wavelength of $\lambda = 4\,\mathrm{m}$ and the wave energy converter equipped with the second power-take-off system: (a) whole domain, (b) detail

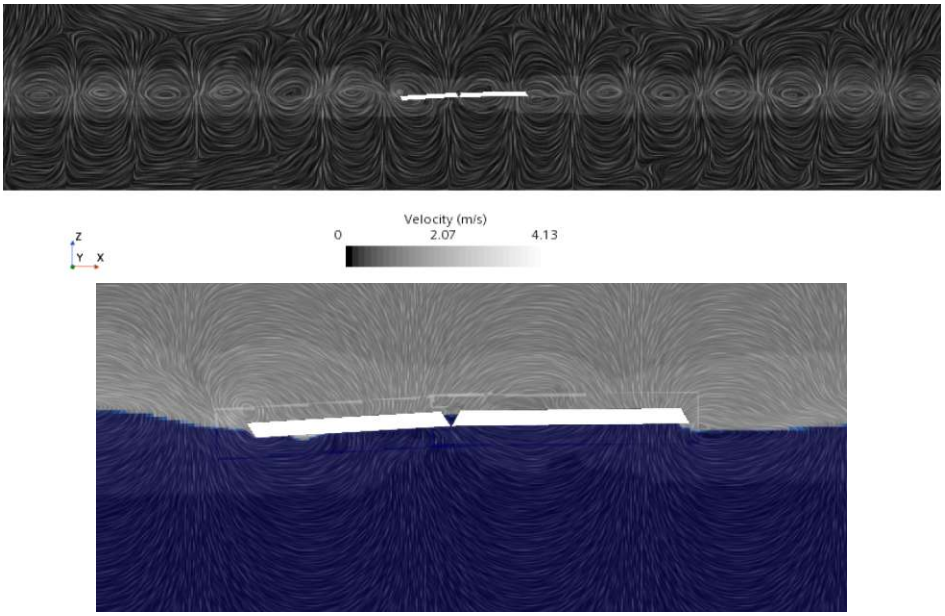

Figure A.19 – Velocity in the wave tank with waves of a wave height of $H = 0.2\,\mathrm{m}$ and a wavelength of $\lambda = 4\,\mathrm{m}$ and the wave energy converter equipped with the third power-take-off system: (a) whole domain, (b) detail

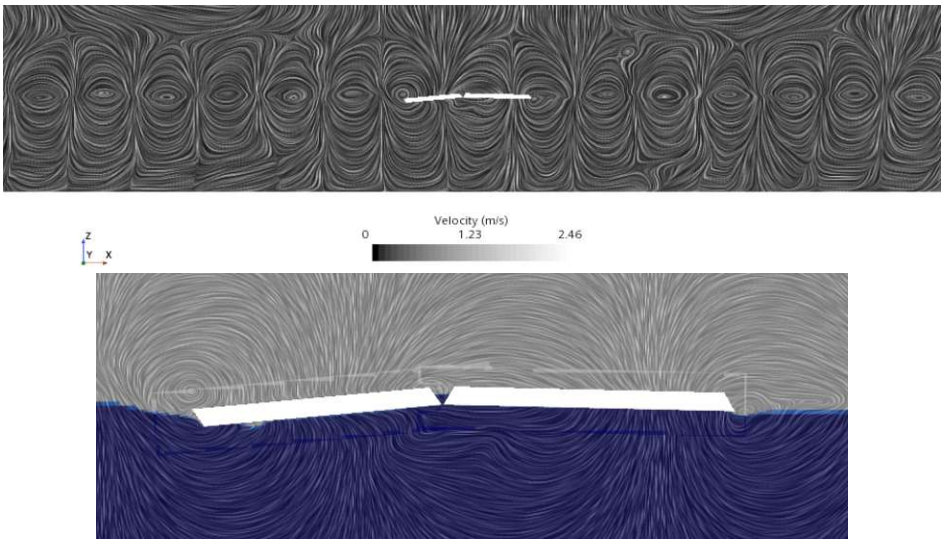

Figure A.20 – Velocity in the wave tank with waves of a wave height of $H = 0.2\,\mathrm{m}$ and a wavelength of $\lambda = 4\,\mathrm{m}$ and the wave energy converter equipped with the fourth power-take-off system: (a) whole domain, (b) detail

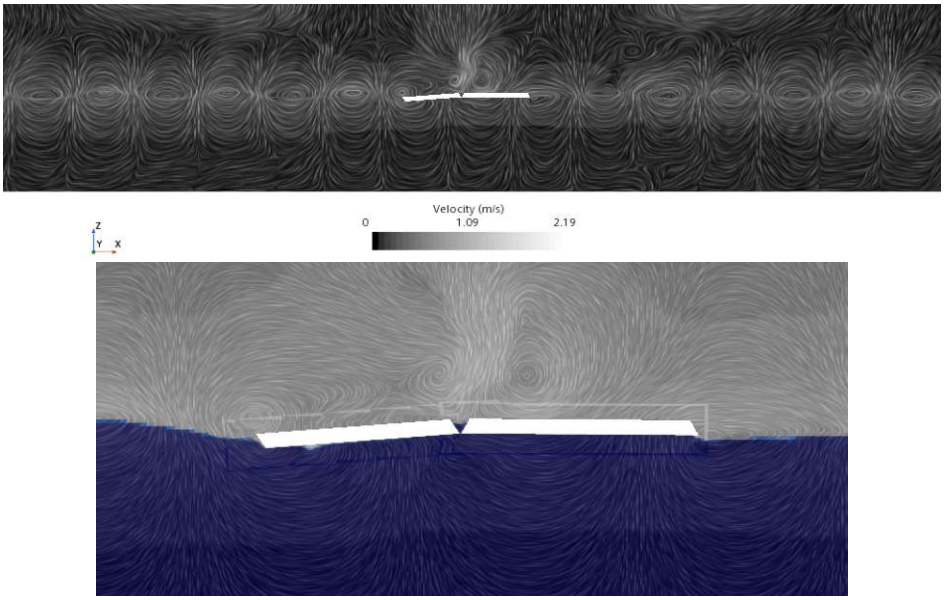

Figure A.21 – Velocity in the wave tank with waves of a wave height of $H = 0.2\,\mathrm{m}$ and a wavelength of $\lambda = 4\,\mathrm{m}$ and the wave energy converter equipped with the fifth power-take-off system: (a) whole domain, (b) detail

A.2.3 Pressure exerted on the bottom of the wave energy converter

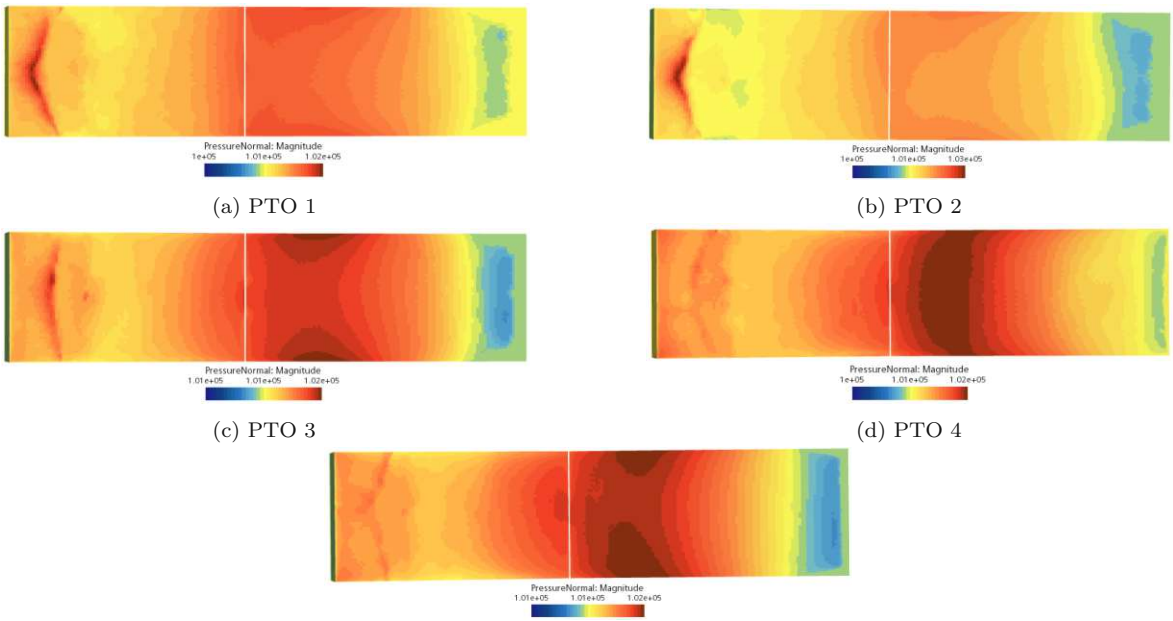

(a) PTO 1

(b) PTO 2

(c) PTO 3

(d) PTO 4

(e) PTO 5

Figure A.22 – Pressure exerted on the bottom of the wave energy converter equipped with different power-take-off system operating in waves of a wave height of $H = 0.20\,\mathrm{m}$ and a wavelength of $\lambda = 4.0\,\mathrm{m}$ at $t = 8s$

A.2.4 Wave elevation before, after and downstream the wave energy converter for different power-take-off systems

Table A.1 – Comparison of incident with downstream wave parameters of simulations with different power-take-off systems

	PTO 1	PTO 2	PTO 3	PTO 4	PTO 5
incident wave height $[H] = \mathrm{m}$	0.20	0.20	0.20	0.20	0.20
wave height after $[H_{After}] = \mathrm{m}$	0.1507	0.1264	0.1433	0.1494	0.1850
wave energy incident on device $[E_{Waves}] = \mathrm{J}$	429.02	429.02	429.02	429.02	429.02
wave energy after device $[E_{WavesAfter}] = \mathrm{J}$	243.55	171.39	220.4	239.25	367.13
difference $[\Delta E] = \mathrm{J}$	185.48	257.63	208.62	189.78	61.9
energy on device $[E_{OnDevice}] = \mathrm{J}$	272.59	304.85	339.12	369.23	361.71

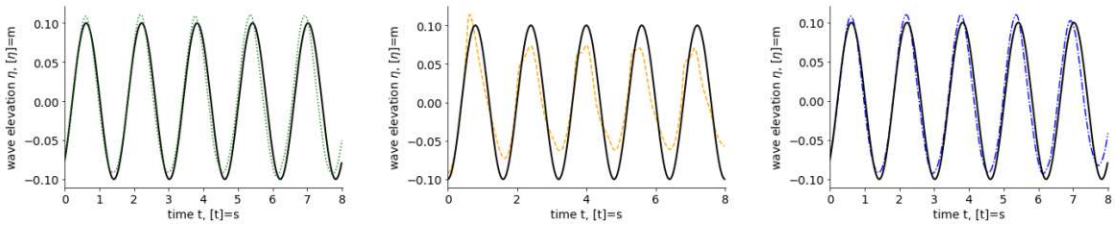

(a) PTO 1

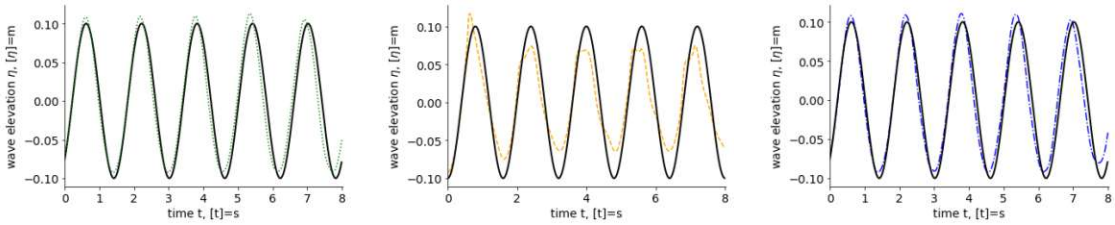

(b) PTO 2

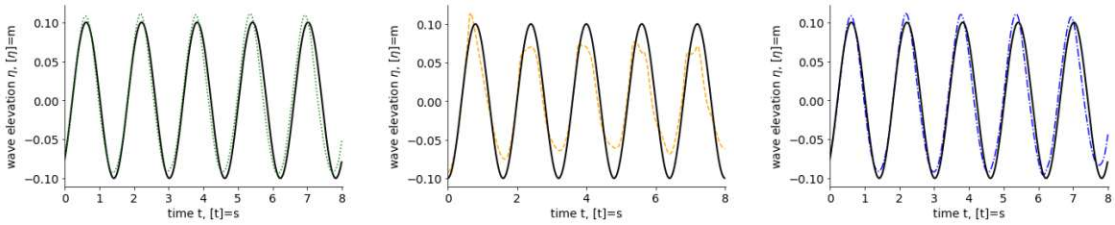

(c) PTO 3

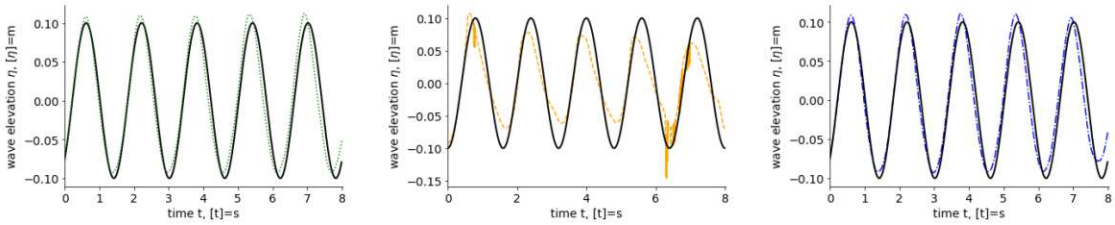

(d) PTO 4

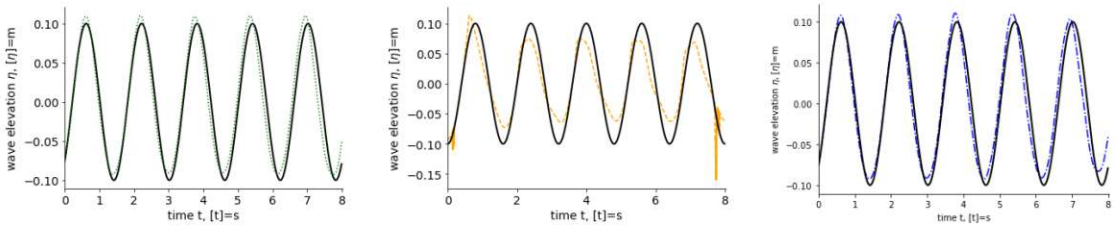

(e) PTO 5

Figure A.23 – wave elevation η for simulated waves having a wave height of $H = 0.2\,\mathrm{m}$ a wavelength of $\lambda = 4\,\mathrm{m}$ measured at different locations in the wave tank and compared to waves according to the linear wave theory (solid black) for different power-take-off systems: 9.1 m in front of the device (left, dotted green), 0.1 m after the device (middle, dashed orange), 8.45 m after the device (right, dashed-dotted blue)